Advances in Emerging Electromagnetics Topics: Metamaterials and Wireless Power Transfer

by

Brian Benjamin Tierney

A dissertation submitted in partial fulfillment
of the requirements for the degree of
Doctor of Philosophy
(Electrical Engineering)
in The University of Michigan
2016

Doctoral Committee:
Associate Professor Anthony Grbic, Chair
Professor Eric Michielssen
Professor Kamal Sarabandi
Associate Professor Max Shtein

It isn't the mountains ahead to climb that wear you out,
it's the pebble in your shoe.
—Muhammad Ali

To my family

Acknowledgments

This thesis would not be possible without the support and guidance of my advisor, Professor Anthony Grbic. Tony, thank you for believing in me and inviting me to join you in Michigan. I couldn't have asked for a more caring and dedicated advisor. You've taught me not only about electromagnetics, but also about how to be a better researcher, writer, and teacher. Your devotion to your work and to your students will always be an inspiration to me. Thank you.

I would like to thank the other members of my doctoral committee: Prof. Eric Michielssen, Prof. Kamal Sarabandi, and Prof. Max Shtein. Thank you for your service and for helping to improve this thesis. I would also like to thank all of the professors and research scientists of the Radiation Laboratory. It was an honor and privilege to learn from such a knowledgeable group. Thank you for everything you have taught me.

I am also grateful and proud to have spent the past five years studying with the talented students of the Radiation Laboratory. I would especially like to thank Gurkan Gok, Mohammadreza Imani, Amit Patel, and Carl Pfeiffer for mentoring me and accepting me into the research group. I would also like to thank Emre Alan and Lai Wei for offering their friendship on day one and for their constant companionship through the first two years of graduate school. You two made the transition to Ann Arbor so much more enjoyable. I would also like to thank Brian Moore and Andy Meier for three great years as roommates. I would also like to thank the rest of my friends in the RadLab, the EECS department, and the Ann Arbor area. When I moved here, I never thought I would meet such a fantastic group of people. I consider myself extremely lucky to have met you all. It will be tough to leave.

Finally, I would like to thank my family. You are the best friends I could have asked for. Thank you for all the laughs we've shared throughout the years and for never growing up too much. Thank you for being a model of resilience and responsibility, especially when times were tough. Mom, thank you for your love and support and for always maintaining a great sense of humor. Also, thank you for having one last child

(me). You can consider this thesis to be your second grandkid. Shaun and Shannon, thank you for being such great role models and for your support throughout the years. Shaun, thank you for getting me into electrical engineering and programming. Feel free to read this thesis to James for a bedtime story. I'm sure it will put him to sleep. Shannon, thank you always letting me hang out during breaks in school. Melissa, thank you for being such a great friend while we were growing up together. Amelia, you've been such a great addition to the family. Thank you for always making me feel at home.

Table of Contents

List of Tables

Table

List of Figures

Figure

List of Appendices

Appendix

Abstract

Advances in Emerging Electromagnetics Topics: Metamaterials and Wireless Power Transfer

by

Brian Benjamin Tierney

Chair: Anthony Grbic

Since their introduction 15 years ago, metamaterials have enabled the design of various new and exotic electromagnetic devices. These devices have included polarization convertors, beam refractors, absorbers, wave collimators, and many others. However, unlocking the full potential of metamaterials requires improving existing design methods. For example, one popular design approach has been transformation electromagnetics, which exploits the form invariance of Maxwells equations under coordinate transformations. However, transformation techniques can often yield material parameters which are difficult to implement, e.g. highly-anisotropic or inherently-dispersive materials.

In this thesis, new techniques are proposed and demonstrated to overcome the deficiencies of current metamaterial design methods. Specifically, a new technique is developed to generate arbitrary radiation patterns using metamaterial leaky-wave antennas. The featured synthesis method is an improvement over the commonly used ray optics method, which often results in degradation of the radiation pattern. The technique is demonstrated using a new leaky-wave impedance-surface topology that is

advantageous due to its independent control of the leakage rate, phase progression, and polarization of leaky-wave modes as well as its simple, planar fabrication.

Furthermore, an optimization technique is developed to overcome the deficiencies of coordinate-transformation methods used to design exotic electromagnetic devices. The proposed procedure has two primary advantages over coordinate-transformation methods: (1) it can place constraints on material parameters to improve practicality and bandwidth and (2) it permits the design of devices for which a transformation map may be difficult/impossible to find, such as those with a different prescribed output for each stipulated input. The procedure is used to design a beamformer with 7 prescribed input/output combinations.

In addition to metamaterial topics, this thesis also presents the design of a wireless non-radiative power transfer (WNPT) system that employs novel, compact, planar-loop resonators with integrated transmission lines and capacitive stubs. These high-Q resonators offer excellent coil-to-coil efficiencies and can be easily fabricated using standard printed-circuit board processes. Moreover, it is shown that the parameters of the resonator can be tailored to achieve a conjugate impedance-matched condition at a prescribed coupling distance, thereby eliminating the need for external matching networks used previously in the literature.

Chapter 1

Introduction

In this thesis, I discuss advances in two emerging topics in electromagnetics: metamaterials and wireless power transfer. In this chapter, I offer a brief history of both topics as well as the shortcomings of each that are addressed in this thesis.

1.1 Metamaterials

1.1.1 A New World

During the past 15 years or so, metamaterials have developed into a powerful tool for designing new, exotic electromagnetic devices. Metamaterials are engineered materials designed to imitate prescribed material parameters, such as permittivity ϵ and permeability μ. These artificial materials were inspired by natural materials, e.g. wood, which derive their macroscopic properties from their microscopic, atomic makeup. Metamaterials derive their macroscopric properties from an arrangement of unit cells, which typically consist of textured metal and/or dielectrics. As long as the period is much less than the operating wavelength, these arrangements can be macroscopically modeled as a homogeneous medium. This homogenization applies not only to 3D arrangements, but also 2D-engineered materials, such as grid of wires modeled as a sheet impedance [1].

With the advent of metamaterials, a new world of design possibilities has opened up. Unusual and unnatural materials can be engineered, such as negative-refractive index materials, which can theoretically be used to engineer a perfect lens [2], or epsilon-near-zero materials, which can be used for tailoring radiation patterns [3].

In 2006, the perfect compliment to metamaterials was introduced. Pendry [4] and Leonhardt [5] independently developed the theory of transformation electromagnetics, which exploits the form invariance of Maxwell's equations under coordinate transfor-

mations to find material parameters that achieved a prescribed function. Now, the inhomogeneity, anisotropy, and overall flexibility offered by metamaterials could be better utilized. Design examples have included invisibility cloaks, wave collimators, and polarization rotators [6].

1.1.2 Shortcomings

Metamaterials and transformation electromagnetics are not without their faults. It is well-known that metamaterials with $\epsilon < \epsilon_0$ or $\mu < \mu_0$ are inherently dispersive [7], thereby limiting bandwidth. This limits the performance of not only negative-refractive index lenses, but also the electromagnetic devices designed using transformation electromagnetics, which often yields dispersive material parameters.

Transformation electromagnetics may also yield parameters that are difficult to implement, such as highly-anisotropic materials. In addition, for certain designs, it may be difficult or impossible to find an appropriate coordinate mapping to utilize the technique. In fact, in many areas of metamaterials, existing design methodologies can be improved.

1.1.3 Motivation

The first part of this thesis addresses the deficiencies of current device design methodologies. Although some metamaterial devices are now designed using well-established, relatively simple design methods, e.g. metasurface design [8–10], other devices are lacking adequate techniques.

In particular, alternative techniques will be explored for designing devices in two areas: (1) the generation of arbitrary radiation patterns using metamaterial leaky-wave antennas and (2) the design of compact, broadband metamaterial beamformers with multiple, prescribed output beams.

The second part of this thesis describes advances in wireless power transfer systems.

1.2 Wireless Power Transfer

1.2.1 A Brief History

Wireless power transfer has a rich history dating back to the late 19th century. At the 1893 World's Columbian Exposition in Chicago, Nikola Tesla demonstrated that he could illuminate phosphorescent lamps without the aid of connecting wires. He positioned the lamps between a pair of rubber plates, which were suspended in air and covered in tin foil. The plates were fed (using wires) with high-voltage, high-frequency alternating current. Essentially, Tesla had constructed a large capacitor. The lamps were able to harvest the energy of the electric field between the plates.

In 1894, Maurice Hutin and Maurice LeBlanc filed a patent in which they described a system to power railway vehicles wirelessly, positing that it would be "very difficult to establish a constant communication between the vehicle and [an] electric conductor under proper conditions." Hutin and LeBlanc proposed a system of coils like those used in a transformer coupled by magnetic induction, a phenomenon discovered 70 years previously by Michael Faraday. However, they noted the inefficiency of the proposed system where "the magnetic conductivity [of air] is about two thousand five hundred times inferior to that of iron", which is "ordinarily employed in transformers for converting the energy from a primary circuit to a secondary circuit." To improve the system, the two engineers employed a capacitor to form a resonant circuit. Like a wine glass shattered by a sound wave at its resonant frequency, resonance can also be used to enhance the efficiency of wireless power transfer. In that same year, 1894, Tesla lit up incandescent lamps at two different laboratories in New York City using this resonant magnetic induction technique.

In the 1960s, William C. Brown demonstrated microwave power transmission by powering a model helicopter for Walter Cronkite and CBS News. This method of wireless power transmission is radiative, meaning that power is beamed from the transmitter and collected by the receiver (helicopter). Up to this point, methods of wireless power transfer had been non-radiative: power was confined to distances less than the wavelength of operation rather than radiated.

Recently, interest has been revived in wireless power transfer using resonant magnetic induction: the same phenomenon used by Hutin, LeBlanc, and Tesla in the late 1890s. In 2007, an MIT research team led by Professor Marin Soljačić wirelessly powered a 60W light bulb using resonant magnetic coupling over distances 8 times the radius of the self-resonant coils [11]. Their experiments demonstrated efficient wireless

energy transfer over larger coupling distances than experiments performed in the past.

In many modern applications, such as medical devices and operation in harsh environments, physical interconnects are bulky, dangerous, or simply not feasible. Wireless power transfer offers an indispensable solution. Today, the development of both non-radiative and radiative power transfer systems continues to gain significant attention to match growing consumer demands in a variety of markets, including consumer electronics [12, 13], medical applications [14–17], and automotive applications [18].

1.2.2 Resonant Magnetic Coupling

The contributions in this thesis will be in the area of near-field, resonant magnetic wireless power transfer. While radiative methods can achieve far greater power transfer distances, they suffer from spatial interference, poor efficiency, and cause heating. Non-radiative, resonant magnetic induction is attractive for several reasons. It is:

- Relatively safe. Magnetic fields interact weakly with dielectric objects and living organisms, compared to electrostatic induction methods, which interact strongly.
- Affordable.
- Simple to implement.

In general, wireless power transmission is a three-step process: DC-to-RF conversion, RF transmission through free space, and RF-to-DC rectification. Therefore, the overall system efficiency depends on the loop-to-loop efficiency as well as the RF conversion and rectification efficiencies.

1.2.3 Motivation

The second part of this thesis will primarily address the loop-to-loop efficiency, which is a function of the quality factor Q of the resonant loops, the mutual inductance M between the loops, and impedance matching. Existing impedance matching techniques, such as those employing intermediate coils [19] or external L-section matching networks [20], may be too bulky for some wireless power applications. This thesis addresses the compactness of impedance-matched loop resonators. In particular, a compact, high-Q, planar loop resonator is developed by incorporating distributed impedance-matching elements into the structure itself, thereby alleviating external matching requirements.

1.3 Goals

This thesis will be broken into three main projects, two of which are related to metamaterials. The goals for each project are provided here.

1.3.1 Metamaterials: Leaky-Wave Beam Shaping

The first project will concern beam shaping in the far field using leaky-wave antennas. The goals for this project are the following:

- To provide eigenmode analysis tools for two different impedance surface topologies: (1) an impedance surface consisting of a conductor-backed, inhomogeneous, uniaxial dielectric topped by an admittance sheet and (2) an impedance surface consisting of cascaded, full-tensor electric admittance sheets separated by homogeneous, dielectric layers.
- To introduce an adaptation of the Orchard-Elliott method for leaky-wave pattern synthesis.
- To demonstrate how controlling the leaky-wave eigenmodes along the length of the antenna allows the generation of prescribed far-field patterns.

1.3.2 Metamaterials: Beamformers

The second project will concern the design of new beamformers using optimization techniques. The goals for this project are the following:

- To design a compact, broadband, printed-circuit beamformer with modest loss.
- To develop a methodology that addresses the shortcomings of transformation electromagnetics.
- To explain how a custom finite-element method (FEM) solver and a constrained nonlinear minimization algorithm can be coupled as an alternative to transformation electromagnetics.
- To convey the importance of developing a custom FEM solver for expediting the optimization process.
- To provide simulation results for two different idealized beamformer designs: (1) a beamformer that transforms each of 7 specified input excitations into a different

beam of prescribed radiation angle (2) a beamformer with 3 input/output pairs that each produce a flattop radiation pattern with 40° beamwidth at different angular ranges.

- To show that the measurement results of the fabricated, 7-port beamformer meet specified design goals.

1.3.3 Wireless Power Transfer

The third project will concern the design of wireless power transfer systems. The goals for this project are the following:

- To introduce a compact, planar, printed loop resonator topology that is simple to fabricate and has low loss.
- To explain the operation of these planar loop resonators and develop a circuit model for them.
- To demonstrate how the parameters of the loop resonator can be tailored for an impedance match at a prescribed coil-to-coil coupling distance.
- To provide experimental results demonstrating high coil-to-coil efficiency over a range of distances using a frequency tuning technique

1.4 Thesis Outline

This thesis is divided into 8 chapters. Chapter 2 introduces a new synthesis technique for generating arbitrary radiation patterns using 1D leaky-wave antennas. The technique consists of a modification of the Orchard-Elliott method [21] used in array synthesis. The analysis is applied to an idealized impedance surface consisting of a grounded, inhomogeneous, uniaxial substrate topped by an admittance sheet. The contributions of Chapter 2 are twofold: (1) a pattern synthesis technique that overcomes the deficiencies of the geometrical optics techniques used in the past by employing an efficient gradient search method and (2) independent control of the leakage constant $\alpha_{\|}$ and phase constant $\beta_{\|}$ using impedance surfaces. Four different antennas are designed and simulated to verify the design procedure.

Chapter 3 introduces a new leaky-wave impedance surface topology that is easier to fabricate than the one introduced in Chapter 2. The topology consists of cascaded,

electric admittance sheets separated by dielectric layers. In addition, control of the radiated polarization is discussed. Resulting designs are verified through full-wave simulation.

Chapter 4 begins the discussion of the beamformer design. An alternative to transformation electromagnetics is proposed. The technique consists of a custom finite-element method (FEM) solver coupled with a constrained nonlinear minimization algorithm. The proposed procedure has two primary advantages over coordinate-transformation methods: (1) it can place constraints on material parameters to improve practicality and bandwidth and (2) it permits the design of devices for which a transformation map may be difficult/impossible to find, such as those with several prescribed outputs for specified inputs. The procedure is applied to the design of two beamformer devices.

Chapter 5 presents the design and fabrication of a printed-circuit implementation of the 7-port beamformer introduced in Chapter 4. The unit cells are tensor transmission-line metamaterials. The result is a printed-circuit beamformer with frequency-invariant beams from 10 GHz to 13 GHz at the prescribed angles.

Chapter 6 introduces the design of planar resonators for wireless power transfer. A compact, high-Q, topology is presented for efficient inductive power transfer. An analytical model is developed for the resonators and used to analyze the behavior of the loops for different geometries. The model shows close agreement with both simulation and measurement results.

Chapter 7 presents a method for tailoring the parameters of the loop resonator presented in Chapter 6 to achieve a 2-port impedance match at a prescribed coupling distance, thereby alleviating the need for external matching networks. Such a technique not only promotes high efficiency, but also a compact structure. Two different sets of loops are fabricated: one for a 2-port match at 15 cm and another for a 2-port match at 20 cm. Measurement results show coil-to-coil efficiencies of 91% and 85% for the two structures, respectively.

Concluding remarks are presented in Chapter 8.

Chapter 2

Tailoring Radiation Patterns with Leaky-Wave Antennas

2.1 Chapter Introduction

2.1.1 Leaky-Wave Antennas

Leaky-wave antennas (LWAs) are traveling-wave antennas that support fast-wave propagation [22, 23]. Power enters from a single input feed and propagates along the antenna while gradually radiating (leaking) energy. Any power that is not radiated is typically absorbed by a load at the end of the antenna. Fig. 2.1 depicts the radiation from a leaky-wave mode with complex wavevector $\vec{k} = \vec{\beta} - j\vec{\alpha}$. The leakage rate and phase progression along the antenna are given by the transverse components $\alpha_{\parallel}$ and $\beta_{\parallel}$, respectively.

Traditional LWA designs are homogeneous, i.e. $\alpha_{\parallel}$ and $\beta_{\parallel}$ remain constant as a function of x along the antenna aperture. As a result, the power radiated from the aperture follows an exponential distribution along x, resulting in an inherent drop in directivity. However, efforts have emerged to vary the leakage rate $\alpha_{\parallel}$ as a function of position along the antenna to improve directivity and/or sidelobe levels [23–26].

2.1.2 Pattern Shaping: Brief Review

Efforts to further shape the radiation pattern by tapering $\beta_{\parallel}$ have been explored in the past [27]. The synthesis of broad (flat-top) radiation patterns using leaky-wave antennas was explored in [28], with an experimental demonstration in [29]. However, the geometrical optics approximation used to calculate $\alpha_{\parallel}(x)$ and $\beta_{\parallel}(x)$ required long antenna lengths, e.g. $20\lambda_0$, and resulted in degraded patterns.

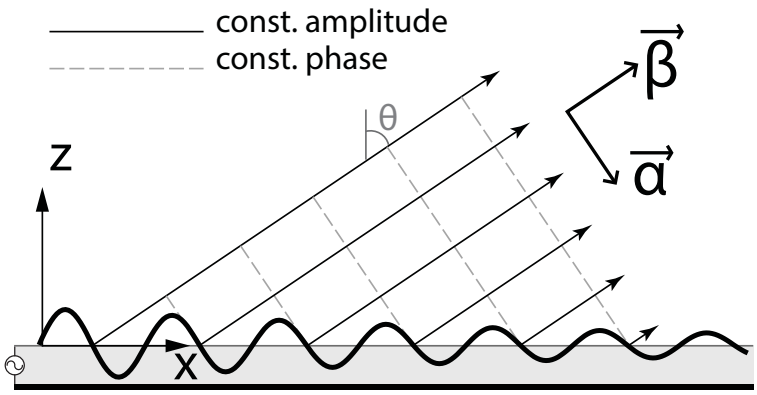

Figure 2.1 Depiction of radiation from a leaky-wave mode with complex wavevector $\vec{k} = \vec{\beta} - j\vec{\alpha}$. The phase progression along the antenna aperture is given by the transverse component $\beta_{\|}$ and the leakage rate is given by the transverse component $\alpha_{\|}$.

Alternatively, [29] employed an iterative FFT technique [30,31] to generate patterns with nulls of arbitrary width and depth. This method could be explored to synthesize arbitrary radiation patterns. However, this technique must work with the phase of the radiation pattern, instead of working only with the magnitude. Moreover, the computation and truncation of an FFT at each iteration can be cumbersome.

2.1.3 Pattern Shaping: A New Approach

In this chapter, the polynomial representation of linear arrays is exploited to employ more efficient synthesis methods and generate radiation patterns with greater accuracy than have been demonstrated previously. The approach utilizes the well-established Orchard-Elliott synthesis method [21]. Specifically, the leaky-wave aperture field is constructed by interpolating a coarsely-sampled Orchard-Elliott array. In this method, the cumbersome iterative FFT method is avoided and substituted with an efficient, gradient search for the desired roots of the array factor polynomial. The proposed method avoids dealing with the phase of the far-field pattern by working directly with the magnitude of the array factor polynomial. Using this technique, a wide range of high-fidelity radiation patterns can be generated. Such accurate synthesis has not been demonstrated to date using the iterative FFT method.

2.1.4 Beam Shaping with Impedance Surfaces

The proposed beam-shaping technique is applied to a homogenized model for impedance surfaces. The model consists of an anisotropic, inhomogeneous substrate topped by an isotropic admittance sheet. In [32], it was shown that $\alpha_{\parallel}$ and $\beta_{\parallel}$ of a leaky wave can be tailored by properly selecting the sheet admittance and dielectric height of an impedance surface. Rather than tapering the dielectric height, here we consider a uniaxial dielectric whose extraordinary (normal to the surface) permittivity $\epsilon_{\perp}$ varies along the aperture. In practice, such a structure can be implemented using a transmission line loaded with series and shunt reactive elements [33,34] or a mushroom structure [35]. However, this is beyond the focus of this work.

The contributions of this chapter are twofold: (1) a pattern synthesis technique is introduced that overcomes the deficiencies of the geometrical optics approximation by using an efficient gradient search method instead of an iterative FFT method, which has not yet been used to demonstrate a variety of high-fidelity patterns, and (2) independent control of $\alpha_{\parallel}$ and $\beta_{\parallel}$ along an impedance surface consisting of a grounded, uniaxial dielectric substrate topped by an admittance sheet.

2.1.5 Chapter Outline

Sec. 2.2 relates the aperture field with the leakage constant $\alpha_{\parallel}(x)$ and phase constant $\beta_{\parallel}(x)$ along the impedance surface. In Sec. 2.3, the transverse resonance technique is used to relate $\alpha_{\parallel}(x)$ and $\beta_{\parallel}(x)$ to the electrical parameters of the impedance surface. In Sec. 2.4, simple antenna designs are presented that achieve prescribed aperture field distributions. In Sec. 2.5, the Orchard-Elliott technique, used in array antenna synthesis, is adapted for the synthesis of arbitrary LWA antenna patterns. In Sec. 2.6, designs are presented that generate arbitrary beam shapes.

2.2 A Brief Review of Aperture Field Analysis

It is well-known [36] that the radiation pattern is related to the aperture field of the antenna via a Fourier transform. It is also well-known how an aperture field relates to the leakage rate and phase constant of a leaky wave. This section briefly reviews these concepts.

The proposed impedance surface is depicted in Fig. 2.2. It supports TM leaky waves that travel in the $+\hat{x}$ direction and gradually radiate energy due to their fast

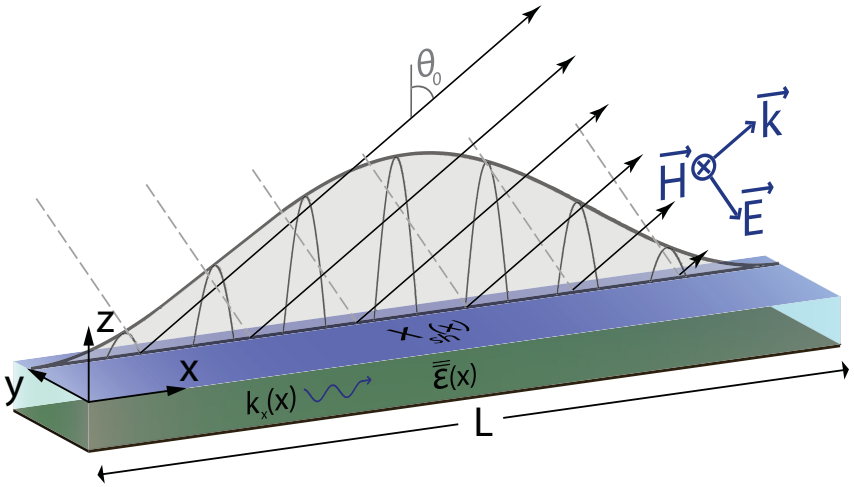

Figure 2.2 Impedance surface supporting TM leaky waves. The structure consists of a grounded, uniaxial substrate topped by an admittance sheet. For the analysis in this chapter, the structure is assumed to be infinite in the $\hat{y}$ direction.

transverse phase constant ($|\beta_{\parallel}(x)| < k_0$). The transverse wavenumber of the leaky wave at each point x is complex: $k_{\parallel}(x) = \beta_{\parallel}(x) - j\alpha_{\parallel}(x)$. In the analysis, it will be assumed that there is no variation in the $\hat{y}$ direction and $k_y = 0$.

2.2.1 Fourier Transform Relations

The far-field pattern $\vec{E}(r, \theta)$ is related to the tangential aperture field $E_x(x, z = 0)$ directly above the surface by a Fourier transform [36]:

$$f_x(\beta_{\parallel}) = \int_{-\infty}^{\infty} E_x(x, 0) e^{j\beta_{\parallel} x} dx \tag{2.1}$$
$$= \mathcal{F}^{-1}\{E_x(x, 0)\}$$
$$\vec{E}(r, \theta) \approx \frac{jk_0 e^{-jk_0 r}}{2\pi r} f_x(\beta_{\parallel} = k_0 \sin\theta)\hat{\theta}. \tag{2.2}$$

The Fourier spectrum $f_x(\beta_{\parallel})$ is the space factor of the antenna [36]. Therefore, Fourier theory can be used to analyze the radiation pattern. For an antenna of length L, the integration bounds are set from 0 to L. To produce a far-field pattern with high directivity, one could employ a constant aperture field:

$$E_x(x, 0) = C \tag{2.3}$$

where C is some scaling constant. Alternatively, to reduce the sidelobes, one could employ a Hamming window [37]:

$$E_x(x,0) = C(0.54 - 0.46\cos(2\pi x/L)). \tag{2.4}$$

Both aperture distributions (2.3) and (2.4) produce a main beam at broadside. To generate a main beam at non-zero angle θ_0, the phase of the fields along the aperture must vary. From the properties of Fourier transforms, application of a linear phase progression $\Phi(x) = -k_0 x \sin\theta_0$ to $E_x(x,0)$ translates the angular spectrum $f_x(\beta_\parallel)$ [38]:

$$\mathcal{F}^{-1}\{E_x(x,0)e^{-jk_0 x\sin\theta_0}\} = f_x(k_0[\sin\theta - \sin\theta_0]). \tag{2.5}$$

If the original spectrum f_x produced a broadside beam, (2.5) represents a beam at an angle θ_0 from broadside. This phase progression is realized by a leaky-wave mode with phase constant given by:

$$\beta_\parallel(x) = k_0 \sin\theta_r(x) = k_0 \sin\theta_0. \tag{2.6}$$

Physically, (2.6) sets the radiation angle at each point x along the antenna to θ_0 [22] (see Fig. 2.2). Far-field patterns with $\theta_0 = 30°$ and aperture magnitudes given by (2.3) and (2.4) are plotted in Fig. 2.3.

Simple patterns are demonstrated in Fig. 2.3. However, determining the aperture field needed to establish a more complicated far-field radiation pattern is not a simple task. This will be discussed further in Sec. 2.5.

2.2.2 Generating the Aperture Field

The electric field magnitude $|E_x(x,0)|$ along the aperture of a leaky-wave antenna is a function of the attenuation constant $\alpha_\parallel(x)$ along x [23]:

$$\frac{|E_x(x,0)|^2}{2\eta_0\cos^2\theta_r(x)} = P_{rad}(x) = 2\alpha_\parallel(x)P(x). \tag{2.7}$$

Here, $\theta_r(x)$ is defined by (2.6), η_0 is the free-space wave impedance, $P_{rad}(x)$ is the per-unit-length power radiated at x, and $P(x)$ is the available power in the antenna at x. Recall that the angle of radiation is given by (2.6). Equation (2.7) can be

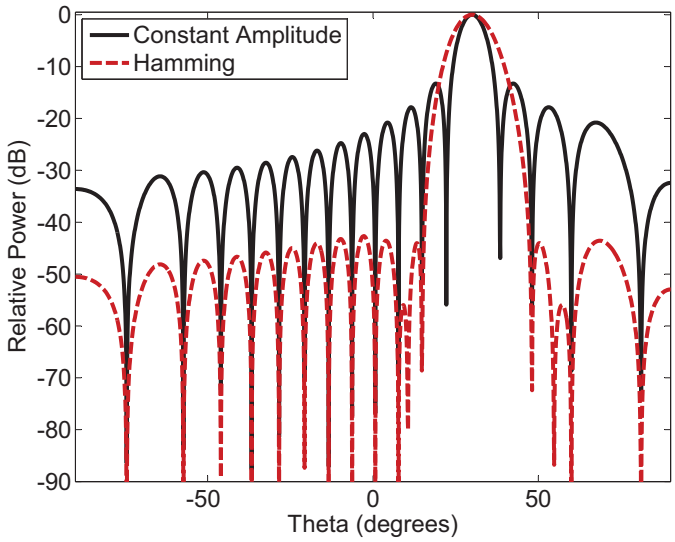

Figure 2.3 The far-field patterns for the aperture magnitude distributions given by (2.3) and (2.4) with $\theta_0 = 30°$.

transformed into an explicit equation for $\alpha_{\|}(x)$ [23]:

$$\alpha_{\|}(x) = \frac{P_{rad}(x)/2}{\frac{1}{F}\int_0^L P_{rad}(\zeta)d\zeta - \int_0^x P_{rad}(\zeta)d\zeta} \tag{2.8}$$

where F is the ratio of total radiated power to accepted input power. Together, (2.7) and (2.8) relate $\alpha_{\|}(x)$ to the magnitude of the aperture field: $|E_x(x,0)|$. The phase constant $\beta_{\|}(x)$ is given by [28]:

$$\beta_{\|}(x) = \frac{d\Phi(x)}{dx}. \tag{2.9}$$

Here, $\Phi(x)$ is the phase of the aperture field at position x.

Equations (2.7), (2.8), and (2.9) show that the magnitude and relative phase of the aperture field $E_x(x,0)$ are established by $\alpha_{\|}(x)$ and $\beta_{\|}(x)$ (see Fig. 2.4). In Sec. 2.3, control of $\alpha_{\|}(x)$ and $\beta_{\|}(x)$ is demonstrated using the electrical parameters of the impedance surface, which facilitates the synthesis of arbitrary aperture fields.

2.3 Eigenmode Analysis

In this section, the complex transverse wavenumber $k_{\|} = \beta_{\|} - j\alpha_{\|}$ supported by a *homogeneous* (non-tapered, i.e. $k_{\|}(x) = k_{\|}$) impedance surface is derived using the transverse resonance technique [39]. The results can be applied to inhomogeneous

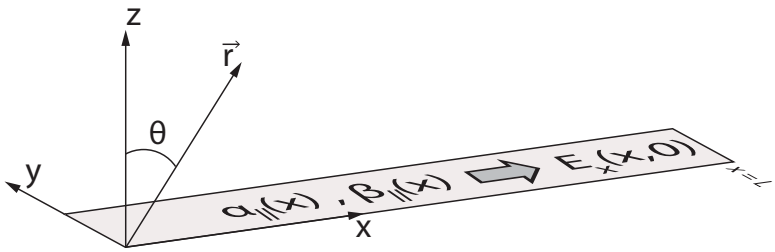

Figure 2.4 The tailoring of $\alpha_{\parallel}(x)$ and $\beta_{\parallel}(x)$ along the antenna surface generates a prescribed tangential electric field $E_x(x,0)$ at the aperture of the impedance surface. The analysis assumes an infinite width in the $\hat{y}$ direction. Thus, the tangential electric field for the TM leaky-wave antenna is purely in the $\hat{x}$ direction.

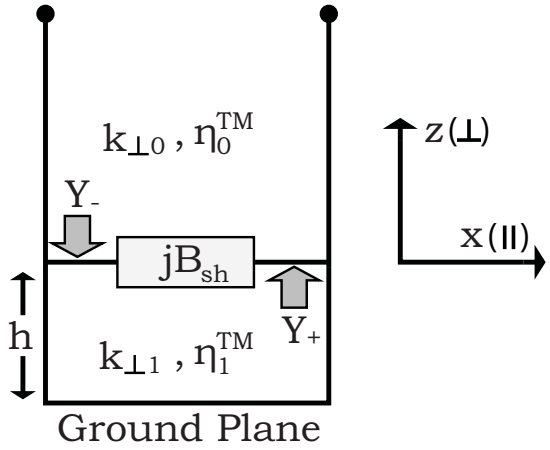

Figure 2.5 Equivalent transmission line problem for the grounded, uniaxial substrate topped by an admittance sheet.

surfaces, as long as the electrical parameters vary slowly. If the parameters are slowly varying, then (2.8) and (2.9) predict the fields well. Slowly-varying parameters are also generally desired to prevent unwanted radiation, such as that from reflected or diffracted waves.

2.3.1 Transverse Resonance Technique

The permittivity $\bar{\bar{\epsilon}}$ of the uniaxial substrate of the leaky-wave impedance surface can be represented by the following tensor:

$$\bar{\bar{\epsilon}} = \begin{bmatrix} \epsilon_{\parallel} & 0 & 0 \\ 0 & \epsilon_{\parallel} & 0 \\ 0 & 0 & \epsilon_{\perp} \end{bmatrix} = \epsilon_0 \begin{bmatrix} \epsilon_{r\parallel} & 0 & 0 \\ 0 & \epsilon_{r\parallel} & 0 \\ 0 & 0 & \epsilon_{r\perp} \end{bmatrix}. \tag{2.10}$$

Here, $\epsilon_\perp$ is the $\hat{z}$-directed, extraordinary permittivity and $\epsilon_\parallel$ is the transverse permittivity.

From transverse resonance, an eigenmode must satisfy the condition $Y_+ + Y_- = 0$ for the equivalent transmission-line circuit of the impedance surface shown in Fig. 2.5 [39]. The admittances Y_+ and Y_- are the admittances looking up and down just above the sheet ($z = 0$). The TM wave impedances are given by [1]:

$$\eta_0^{TM} = \frac{k_{\perp 0}}{\omega \epsilon_0} \tag{2.11a}$$

$$\eta_1^{TM} = \frac{k_{\perp 1}}{\omega \epsilon_\parallel}. \tag{2.11b}$$

The subscript 0 refers to the free-space region above the surface, and subscript 1 refers to the uniaxial substrate. The transverse resonance condition can therefore be written as

$$\frac{k_0}{\eta_0 k_{\perp 0}} + jB_{sh} - j\frac{k_0 \epsilon_{r\parallel}}{\eta_0 k_{\perp 1}} \cot\left(k_{\perp 1} h\right) = 0. \tag{2.12}$$

At first, this equation appears to be equivalent to the dispersion equation provided in [32] for an isotropic dielectric. However, the separation relation for the dielectric substrate in the present case is that of a uniaxial medium [40]:

$$k_0^2 \epsilon_{r\parallel} \epsilon_{r\perp} \mu_r = k_{\perp 1}^2 \epsilon_{r\perp} + k_\parallel^2 \epsilon_{r\parallel}. \tag{2.13}$$

In the free-space above, the separation relation is given by:

$$k_{\perp 0}^2 = k_0^2 - k_\parallel^2. \tag{2.14}$$

It is difficult to discern the behavior of the transverse wavenumber $k_\parallel$ from (2.12). However, explicit expressions for $\alpha_\parallel$ and $\beta_\parallel$ can be derived under the conditions of an electrically thin substrate and a low attenuation constant: $\beta_{\perp 1} h \ll 1$ and $\alpha_{\perp i} \ll \beta_{\perp i}$.

2.3.2 Solving for $\alpha_\parallel$ and $\beta_\parallel$

Combining (2.13) and (2.14) yields an expression for $k_{\perp 1}$ in terms of $k_{\perp 0}$:

$$k_{\perp 1}^2 = [k_0^2(\epsilon_{r\perp}\mu_r - 1) + k_{\perp 0}^2]\frac{\epsilon_{r\parallel}}{\epsilon_{r\perp}}. \tag{2.15}$$

If we assume $|k_{\perp 1}h| \ll 1$, then $\cot(k_{\perp 1}h) \approx {}^1\!/_{k_{\perp 1}h}$. By substituting (2.15) into (2.12), the dispersion equation can be written in terms of $k_{\perp 0}$ (for $k_{\perp 0} \neq 0$):

$$\begin{aligned} &k_0 h[k_0^2(\epsilon_{r\perp}\mu_r - 1) + k_{\perp 0}^2]\frac{\epsilon_{r\parallel}}{\epsilon_{r\perp}} \\ &+ jB_{sh}\eta_0 h k_{\perp 0}[k_0^2(\epsilon_{r\perp}\mu_r - 1) + k_{\perp 0}^2]\frac{\epsilon_{r\parallel}}{\epsilon_{r\perp}} - jk_0\epsilon_{r\parallel}k_{\perp 0} = 0. \end{aligned} \tag{2.16}$$

For leaky-wave modes, $k_{\perp 0}$ is complex-valued and of the form $k_{\perp 0} = \beta_{\perp 0} + j\alpha_{\perp 0}$. Therefore, (2.16) can be decomposed into its real and imaginary parts to yield two equations:

$$\begin{aligned} &(\epsilon_{r\perp}\mu_r - 1)k_0^3 h\frac{\epsilon_{r\parallel}}{\epsilon_{r\perp}} + k_0 h(\beta_{\perp 0}^2 - \alpha_{\perp 0}^2) - B_{sh}\eta_0 h(\epsilon_{r\perp}\mu_r - 1)k_0^2\alpha_{\perp 0}\frac{\epsilon_{r\parallel}}{\epsilon_{r\perp}} \\ &- B_{sh}\eta_0 h(3\beta_{\perp 0}^2\alpha_{\perp 0} - \alpha_{\perp 0}^3)\frac{\epsilon_{r\parallel}}{\epsilon_{r\perp}} + k_0\epsilon_{r\parallel}\alpha_{\perp 0} = 0. \end{aligned} \tag{2.17}$$

$$\begin{aligned} &2k_0 h\beta_{\perp 0}\alpha_{\perp 0}\frac{\epsilon_{r\parallel}}{\epsilon_{r\perp}} + B_{sh}\eta_0 h(\epsilon_{r\perp}\mu_r - 1)k_0^2\beta_{\perp 0}\frac{\epsilon_{r\parallel}}{\epsilon_{r\perp}} \\ &+ B_{sh}\eta_0 h(\beta_{\perp 0}^3 - 3\beta_{\perp 0}\alpha_{\perp 0}^2)\frac{\epsilon_{r\parallel}}{\epsilon_{r\perp}} - k_0\epsilon_{r\parallel}\beta_{\perp 0} = 0. \end{aligned} \tag{2.18}$$

Equations (2.17) and (2.18) can be solved explicitly for $\alpha_{\perp 0}$ and $\beta_{\perp 0}$ and simplified under the condition $\alpha_{\perp i} \ll \beta_{\perp i}$. As a result, (2.18) simplifies to:

$$\beta_{\perp 0}^2 = -(\epsilon_{r\perp}\mu_r - 1)k_0^2 + \frac{k_0\epsilon_{r\perp}}{B_{sh}\eta_0 h}. \tag{2.19}$$

To relate $\beta_{\perp 0}$ to the transverse phase constant $\beta_\parallel$, the wavenumber components from (2.14) can be decomposed into real and imaginary parts, and simplified using $\alpha_{\perp i} \ll \beta_{\perp i}$:

$$\beta_\parallel^2 \approx k_0^2 - \beta_{\perp 0}^2 \tag{2.20}$$

$$\alpha_{\parallel} = \frac{\beta_{\perp 0}}{\beta_{\parallel}} \alpha_{\perp 0}. \tag{2.21}$$

Recall that the sign convention for $\alpha_{\parallel}$ is such that $k_{\parallel} = \beta_{\parallel} - j\alpha_{\parallel}$. Plugging (2.19) into (2.20) yields an equation for $\beta_{\parallel}$:

$$\beta_{\parallel}^2 = k_0^2 \epsilon_{r\perp} \left[\mu_r - \frac{1}{B_{sh} k_0 \eta_0 h} \right]. \tag{2.22}$$

Note that the dispersion equation (2.22) is independent of $\epsilon_{r\parallel}$. Plugging (2.22) into (2.17) with $\alpha_{\perp i} \ll \beta_{\perp i}$ results in an equation for $\alpha_{\perp 0}$:

$$\alpha_{\perp 0} = \frac{\epsilon_{r\perp}}{2\eta_0^2 h B_{sh}^2 [1 - \epsilon_{r\perp}(\mu_r - \frac{1}{B_{sh} k_0 \eta_0 h})]}. \tag{2.23}$$

The leakage constant $\alpha_{\parallel}$ is related to $\alpha_{\perp 0}$ by combining (2.19), (2.21), and (2.22) resulting in:

$$\alpha_{\parallel} = \frac{1}{2B_{sh}^2 \eta_0^2 h} \sqrt{\frac{\epsilon_{r\perp}}{(1 - \epsilon_{r\perp}(\mu_r - \frac{1}{B_{sh} k_0 \eta_0 h}))(\mu_r - \frac{1}{B_{sh} k_0 \eta_0 h})}}. \tag{2.24}$$

Equation (2.24) yields positive values for $\alpha_{\perp 0}$ and $\alpha_{\parallel}$ under the condition

$$\epsilon_{r\perp}(\mu_r - \frac{1}{B_{sh} k_0 \eta_0 h}) < 1. \tag{2.25}$$

From inspection of (2.22), condition (2.25) is simply the fast-wave criterion for leaky-wave radiation ($|\beta_{\parallel}| < k_0$).

2.3.3 Impedance Matching

Equations (2.22) and (2.24) can be used to determine the required electrical parameters of the impedance surface for a given distribution of $\alpha_{\parallel}(x)$ and $\beta_{\parallel}(x)$. However, as the electrical parameters are tapered along the impedance surface, the wave impedance will change and cause reflections which may degrade the desired far-field pattern. The x-directed wave impedance within the substrate for TM waves propagating in the $+\hat{x}$ direction along the antenna is given as follows:

$$\eta_{\parallel 1}^{TM}(x) = \eta_0 \frac{k_{\parallel}(x)}{k_0 \epsilon_{r\perp}(x)}. \tag{2.26}$$

A constant TM wave impedance within the substrate of the antenna is achievable by maintaining a constant ratio $k_{\parallel}(x)/\epsilon_{r\perp}(x)$. For tailored far-field patterns, $\alpha_{\parallel}(x)$

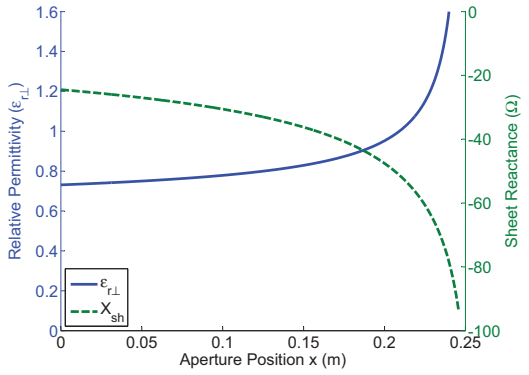

(a) Electrical parameters for the LWA with constant aperture magnitude distribution ($\theta_0 = 50°$).

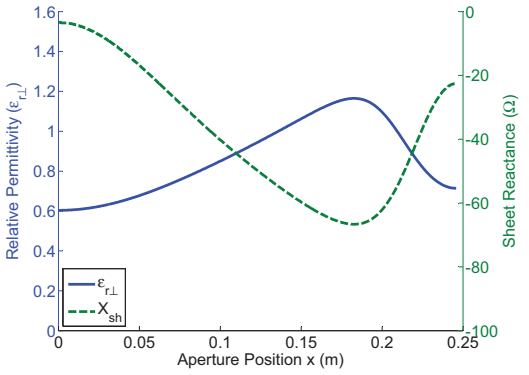

(b) Electrical parameters for the LWA with aperture magnitude distribution corresponding to a Hamming window ($\theta_0 = 50°$).

Figure 2.6 The design parameters $\epsilon_{r\perp}$ and X_{sh} for the simple antenna designs.

varies but is small with respect to $\beta_{\parallel}$(x). Therefore a constant ${}^{\beta_{\parallel}(x)}/_{\epsilon_{r\perp}(x)}$ ensures a relatively-constant TM wave impedance:

$$\eta_{\parallel 1}^{TM}(x) \approx \eta_0 \frac{\beta_{\parallel}(x)}{k_0 \epsilon_{r\perp}(x)} := \eta_m. \tag{2.27}$$

The parameters X_{sh}, $\epsilon_{r\perp}$, and μ_r can be used to control $\alpha_{\parallel}$ and $\beta_{\parallel}$ while maintaining a constant ${}^{\beta_{\parallel}(x)}/_{\epsilon_{r\perp}(x)}$ ratio. Here, $X_{sh} = {}^{-1}/_{B_{sh}}$ is the admittance sheet. Using (2.22) and (2.24), the required parameters are

$$\epsilon_{r\perp} = \frac{\eta_0 \beta_{\parallel}}{\eta_m k_0} \tag{2.28}$$

$$X_{sh} = \pm \sqrt{\frac{2\eta_0 (k_0^2 - \beta_{\parallel}^2) \alpha_{\parallel} h \eta_m}{k_0 \beta_{\parallel} \cot \theta_r}} \tag{2.29}$$

$$\mu_r = \frac{\beta_{\parallel} \eta_m h \mp X_{sh}}{k_0 \eta_0 h}. \tag{2.30}$$

2.3.4 Eigenmode Control

For slowly-varying electrical parameters, the reflections within the LWA can be neglected and therefore the permeability μ_r can be kept constant. For the designs described in this chapter, $\mu_r = 1$ while X_{sh} and $\epsilon_{r\perp}$ are varied. For a prescribed transverse wavenumber $k_{\parallel}$, the required X_{sh} and $\epsilon_{r\perp}$ (with $\mu_r = 1$) are derived by

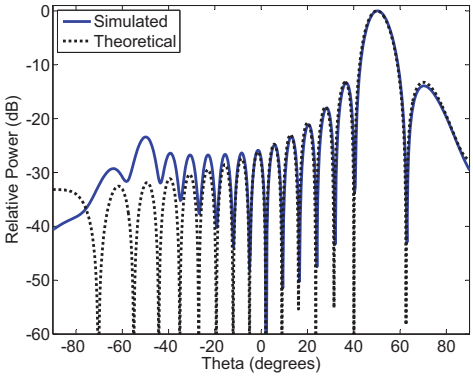

(a) LWA with constant aperture magnitude distribution for improved directivity with main beam at angle $\theta_0 = 50°$. The simulated fraction F of radiated power to accepted power is 96.8%.

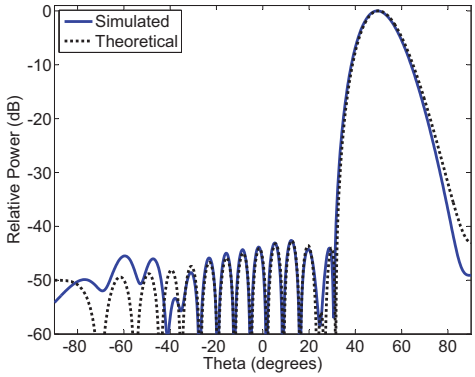

(b) LWA with aperture magnitude distribution corresponding to a Hamming window for reduced sidelobe levels with main beam at angle $\theta_0 = 50°$. The simulated fraction F of radiated power to accepted power is 98.3%.

Figure 2.7 Far-field simulations for the simple antenna designs.

combining (2.22) and (2.24):

$$X_{sh} = \frac{\alpha_\parallel \eta_0 (k_0^2 - \beta_\parallel^2) \pm \chi}{\cot\theta_r \beta_\parallel^2 k_0} \tag{2.31}$$

$$\chi := \eta_0 \sqrt{\alpha_\parallel^2 (k_0^2 - \beta_\parallel^2)^2 + (2\cot\theta_r \mu_r h k_0^2 \beta_\parallel^2 \alpha_\parallel (k_0^2 - \beta_\parallel^2))}$$

$$\epsilon_\perp = \frac{\epsilon_0 \beta_\parallel^2}{k_0^2 \mu_r + \frac{X_{sh} k_0}{\eta_0 h}}. \tag{2.32}$$

Therefore, $\alpha_\parallel(x)$ and $\beta_\parallel(x)$ can be tailored using the electrical parameters of the impedance surface, according to (2.31) and (2.32). For more accurate values of X_{sh} and $\epsilon_\perp$, (2.12) can be solved numerically.

2.4 Simple Designs: Prescribing Aperture Fields

The complete antenna design procedure is explicitly enumerated as follows:

1. Stipulate or determine the aperture field $E_x(x, 0)$.
2. Compute the leakage constant $\alpha_\parallel$ and phase constant $\beta_\parallel$ from the aperture field $E_x(x, 0)$ using (2.7), (2.8), and (2.9).

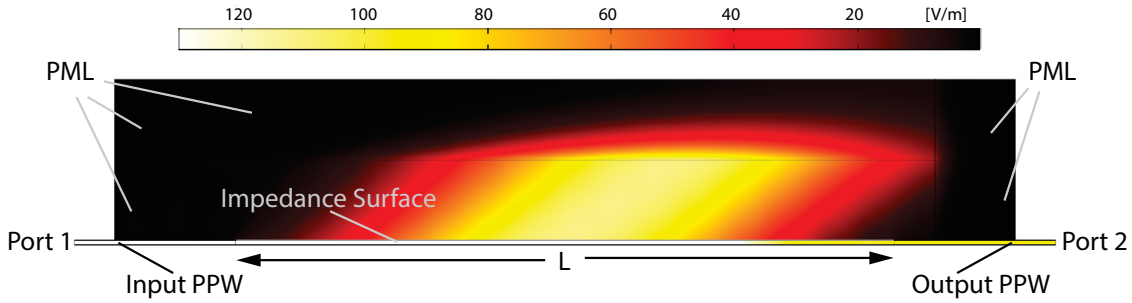

Figure 2.8 Plot of electrical field magnitude from a 2D COMSOL simulation. The fields depicted are those corresponding to the Hamming antenna. The antenna is fed using an air-filled parallel-plate waveguide (PPW). Perfectly-matched layers (PMLs) are employed to absorb radiated fields. The input power is 1 W/m.

3. Compute the electrical parameters $\epsilon_{r\perp}$ and X_{sh} of the impedance surface using (2.31) and (2.32) or by solving (2.12) directly for greater accuracy.

In this section, two simple antennas with prescribed aperture fields are presented. The antennas operate at 10 GHz with length L = 24.6 cm ($8.2\lambda_0$), thickness h = 1.57 mm, and $\epsilon_{r\parallel} = 2.2$. In these designs, $\beta_\parallel(x)$ is kept constant to realize a beam pointing at $\theta_0 = 50°$ while the aperture magnitude is tapered to control the directivity and sidelobe levels. The two aperture magnitude distributions are as follows: (1) a constant magnitude distribution for improved directivity and (2) a magnitude distribution corresponding to a Hamming window for reduced sidelobe levels.

The leakage constant $\alpha_\parallel(x)$ for the first antenna, having an aperture with a constant magnitude distribution, is given by:

$$\alpha_\parallel(x) = \frac{1}{2\left(\frac{L}{F} - x\right)}. \tag{2.33}$$

Using (2.4), the leakage constant $\alpha_\parallel(x)$ for the second antenna having an aperture with a Hamming window magnitude distribution is given by:

$$\alpha_\parallel(x) = \frac{(4.16 - 3.54\cos\left(\frac{2\pi x}{L}\right))^2}{47.13(\frac{L}{F} - x) + 9.38L\sin\left(\frac{2\pi x}{L}\right) - L\sin\left(\frac{4\pi x}{L}\right)}. \tag{2.34}$$

The electrical parameters were calculated using (2.31) and (2.32) for $F = 0.98$ and are plotted in Fig. 2.6. Note that as the leakage constant increases, the required admittance sheet becomes less capacitive. Physically, the capacitive gaps would become larger, thereby producing a higher leakage rate.

The designs were simulated using COMSOL Multiphysics and the patterns are provided in Fig. 2.7. A view of the simulated fields is provided in Fig. 2.8, using the Hamming antenna as an example. The antennas were fed by an air-filled PPW at the input and output. Since the focus of this chapter is on the methods of generating arbitrary radiation patterns, impedance matching at the input feed is not optimized here. However, the captions in Fig. 2.7 do provide a simulated value for the ratio F of radiated power to accepted power. The simulated values are close to the designed value of $F = 98\%$.

2.5 Arbitrary Beam Shaping

In Sections 2.2 and 2.3, it was shown how to generate a prescribed aperture field by tailoring the electrical parameters of the impedance surface. In Sec. 2.4, simple antenna patterns were synthesized by stipulating the aperture field. However, the aperture field must often be determined from a desired far-field radiation distribution [41]. Such an inverse problem is not straightforward, but synthesis methods are well-known [36]. For traveling-wave antennas, several methods can be found in [27]. One method is geometrical optic, which has been used previously to design broad (flat-top) antenna patterns [28, 29]. However, the inherent high-frequency approximation leads to poor far-field predictions, particularly for low values of antenna length $k_0 L$.

Exact, spectral analysis of the aperture field directly above the antenna surface has been investigated in [30] using an iterative FFT method. In this chapter, a method is proposed which avoids iterative FFTs and instead exploits the polynomial representation of linear antenna arrays to employ an efficient gradient search method. Moreover, the technique only involves the magnitude of the radiation pattern. The method is a modification to the Orchard-Elliott method used in antenna array theory [21], which is a well-established method of synthesizing arbitrary patterns. Using this method, a variety of radiation patterns are generated that exhibit higher fidelity than those generated using the iterative FFT method.

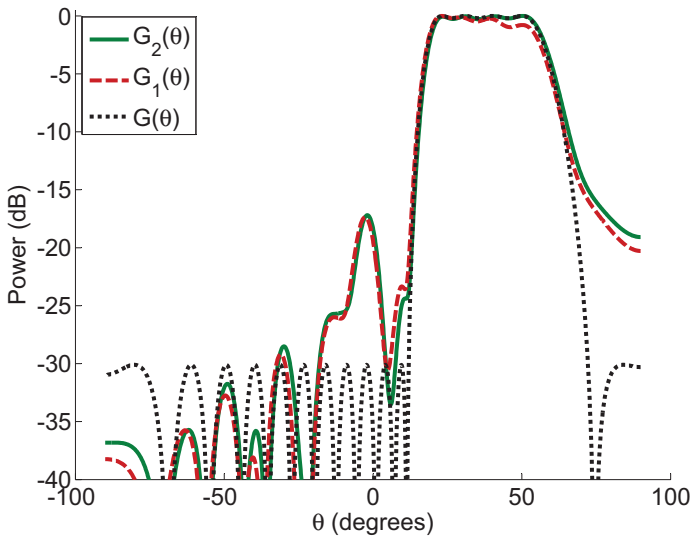

Figure 2.9 Comparison of the space factors $G_1(\theta)$ and $G_2(\theta)$ with the array factor $G(\theta)$. Here, $N_1 = 3$, $N_2 = 12$, $L = 24.6$ cm, $\theta_0 = 20°$, $\theta_1 = 60°$, 0.1 dB ripple, -30 dB sidelobes, $\zeta = 1$, and P = 2. After only two iterations, the space factor matches well with the array factor in the shaped region.

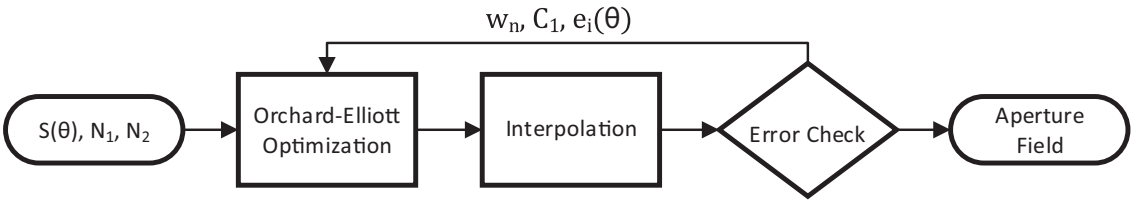

Figure 2.10 Algorithm to compensate for degradation of the far-field pattern resulting from interpolating the excitation coefficients found using the Orchard-Elliott technique.

2.5.1 Aperture Field Methods

Far-field patterns can be synthesized using either continuous (lines or surfaces) sources or discrete (1D and 2D arrays) sources. Popular design methods include the Fourier transform method [42], the Woodward-Lawson method [43,44], and the Orchard-Elliott method [21]. A detailed review of these methods can be found in [36, 41].

In the Fourier transform method, the space factor (for continuous sources) or array factor (for discrete sources) is computed using the Fourier transform relation between the aperture field and far field, given by (2.1). However, the calculated aperture field must be truncated to a finite antenna area. Such apodization of the source leads to significant degradation of the far-field pattern. Moreover, the phase of the far-field pattern must also be stipulated to employ (2.1). Since the only practical concern is the power pattern, specification of the phase diminishes the design freedom.

In [30, 31], an iterative Fourier transform method is employed. Still, the technique requires truncation of the computed aperture field at each step and must work with the phase of the far field.

In the Woodward-Lawson method, the space factor or array factor of a 1D antenna is constructed by summing together N weighted composing functions. Each composing function has a corresponding peak at one of N distinct, equi-spaced angles in the shaped region of the far-field and a null at the other $N-1$ angles. Each function is weighted to attain the magnitude of the prescribed far-field pattern at its corresponding angle. In this way, the desired far-field magnitude is reproduced exactly at the N angles and approximately elsewhere [36]. However, the pattern zeros occur in pairs, which means that the design flexibility for the array is cut in half [41].

For antenna arrays (discrete sources), the Orchard-Elliott method overcomes the aforementioned shortcomings and has proven to be superior for far-field synthesis [36,41]. However, the method is inherently designed for discrete arrays. Nevertheless, discrete arrays can be used to approximate line-source distributions and vice-versa using the concept of sampling [45]. In this chapter, the following procedure is used to find the desired aperture field:

1. The excitation coefficients corresponding to the desired radiation pattern are found using the Orchard-Elliott method. Coarse inter-element spacing is used since fine sampling yields rapidly varying coefficients.
2. Linear interpolation between the excitation coefficients of the coarse array is used to construct the aperture field.
3. The method is applied iteratively to reduce pattern degradation resulting from interpolation. Convergence occurs after a few iterations.

Note that although sinc interpolation would yield a more exact pattern, linear interpolation is used here to yield a more practical aperture field.

2.5.2 A Brief Review of the Orchard-Elliott Method

The far-field array factor F of an equi-spaced linear array of $N+1$ elements is given by a N-degree polynomial in w [21]:

$$F(\psi) = \sum_{n=0}^{N} I_n e^{jnk_0 \Delta x \cos\theta} = \sum_{n=0}^{N} I_n w^n = I_N \prod_{n=1}^{N} (w - w_n). \tag{2.35}$$

Here, Δx is the inter-element spacing, k_0 is the free-space wavenumber, $\psi = k_0 \Delta x \cos\theta$, $w = e^{j\psi}$, and I_n is the complex excitation coefficient of the n^{th} radiating element. The rightmost side of (2.35) is the representation of F as a product of binomials using the N roots w_n of F. The roots are alternatively expressed as complex exponentials $w_n = e^{a_n + jb_n}$, where a_n and b_n are real numbers. In the Orchard-Elliott method, one root is fixed at $w = -1$, N_1 roots are positioned slightly off the Schelkunoff unit circle ($a_n \neq 0$) to control the shaped region, and the remaining N_2 roots are anchored onto the Schelkunoff unit circle ($a_n = 0$) to control the sidelobe region. The total number of discrete, radiating elements is $N + 1$, where $N = N_1 + N_2 + 1$ is the total number of roots. The array factor $F(\psi)$ expressed in decibels is:

$$\begin{aligned} G(\psi) = &\left[\sum_{n=1}^{N-1} 10\log_{10}[1 - 2e^{a_n}\cos(\psi - b_n) + e^{2a_n}]\right] \\ &+ 10\log_{10}[2(1 + \cos\psi)] + C_1. \end{aligned} \tag{2.36}$$

Here, $C_1 = 20\log_{10}|I_N|$. The beam shape is prescribed by the shaping function $S(\theta)$, which is mapped to the ψ domain. Using the gradient descent method, the roots w_n are found such that $G(\psi)$ equals $S(\psi)$ with some prescribed ripple in the range $\psi_1 \leq \psi \leq \psi_0$ and the sidelobes of $G(\psi)$ in the unshaped region equal desired levels. Due to the differing initial positions of the N_1 beam-shaping roots, 2^{N_1} different solutions are achievable with the Orchard-Elliott method. Convergence is usually achieved after about ten iterations for any of these solutions. For more detail, the reader is referred to [21].

2.5.3 Relating Space Factors to Array Factors

Recall that the space factor $f_x(\theta)$ of the leaky-wave antenna is given by (2.1). If it is possible to equate $f_x(\theta)$ to an antenna array factor, the Orchard-Elliott method can be employed directly to design the aperture field. By partitioning the aperture field $E_x(x, 0)$ into N segments of size $\Delta x = {}^{L}/_{N}$, the space factor $f_x(\theta)$ can be written as:

$$\begin{aligned} f_x(\theta) &= \int_0^L E_x(x,0)e^{jk_0 x\sin\theta}dx \\ &= \sum_{n=0}^{N}\left[\int_0^{\Delta x} E_x(x' + n\Delta x, 0)e^{jk_0 x'\sin\theta}dx'\right]e^{jk_0 n\Delta x\sin\theta} \end{aligned}$$

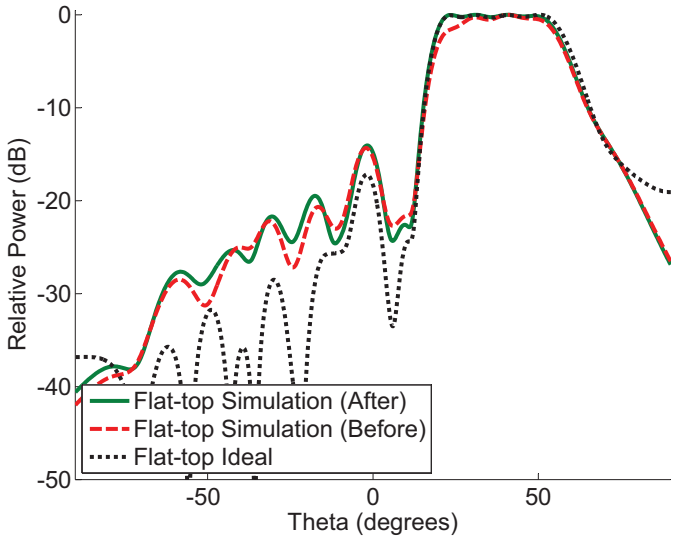

Figure 2.11 Far-field patterns for the flat-top antenna before and after the iterative optimization to reduce error observed in the full-wave simulation.

$$= \sum_{n=0}^{N} B_n(\theta) I_n e^{jk_0 n\Delta x \sin\theta}. \tag{2.37}$$

Here, $B_n(\theta)$ is the element factor of each partition. If $B_n(\theta)$ is independent of n, i.e. $B_n(\theta) = B(\theta)$, then the well-known principle of pattern multiplication is achieved:

$$f_x(\theta) = B(\theta)A(\theta) \tag{2.38a}$$

$$A(\theta) = \sum_{n=0}^{N} I_n e^{jk_0 n\Delta x \sin\theta}. \tag{2.38b}$$

Here, $A(\theta)$ is the array factor. In fact, for small $k_0\Delta x$ (fine sampling), $B_n(\theta) \approx B(\theta)$ in the beam-shaping region and array analysis can be employed. However, the coefficients resulting from the Orchard-Elliott technique vary rapidly for such fine sampling. So instead, a coarse array is designed here using the Orchard-Elliot technique and interpolated to construct the desired continuous aperture field.

2.5.4 Constructing the Aperture Field

To construct the desired aperture field from the computed Orchard-Elliott coefficients, the following procedure is proposed:

1. Construct the aperture field $E_x(x,0) = |E_x(x,0)|e^{j\Psi(x)}$ at discrete points

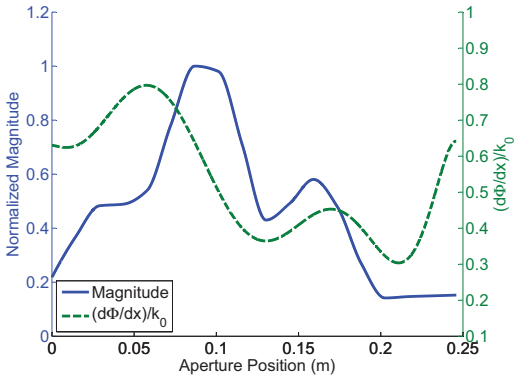

(a) LWA with flat-top beam shape in the range $\theta \in (20°, 60°)$.

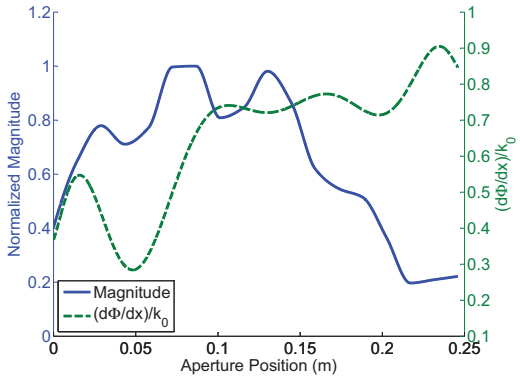

(b) LWA with $\csc^2\theta\cos\theta$ beam shape in the range $\theta \in (15°, 55°)$.

Figure 2.12 Aperture field for the shaped beam patterns resulting from the adapted Orchard-Elliott technique. The derivative $\frac{d\phi}{dx}$ (normalized to k_0) of the phase is plotted to visualize $\beta_{\parallel}(x)$.

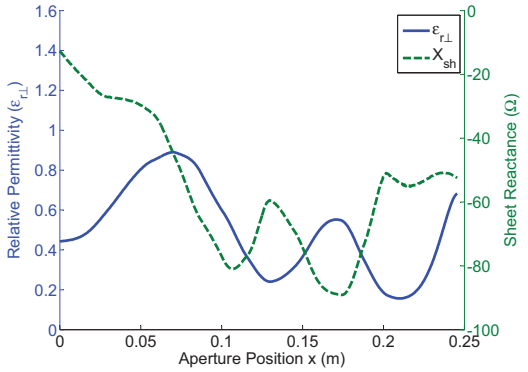

(a) Electrical parameters for the optimized LWA with flat-top beam shape in the range $\theta \in (20°, 60°)$.

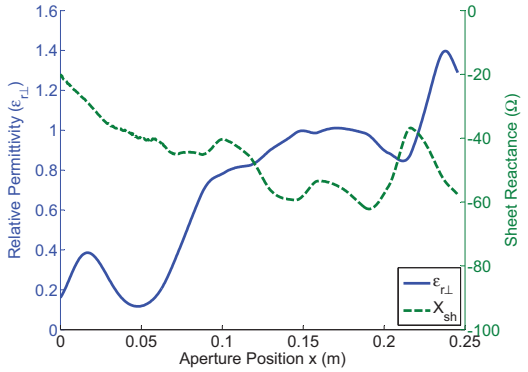

(b) Electrical parameters for the optimized LWA with $\csc^2\theta\cos\theta$ beam shape in the range $\theta \in (15°, 55°)$.

Figure 2.13 The design parameters $\epsilon_{r\perp}$ and X_{sh} for the final antenna designs for arbitrary beam shaping.

$n\Delta x$ along the aperture using the Orchard-Elliot coefficients. Specifically, let $E_x(n\Delta x, 0) = {}^{I_n}/_{\Delta x}$.

2. Construct the remaining magnitude function $|E_x(x,0)|$ using piecewise cubic interpolation [46] between the discrete points $|E(n\Delta x, 0)|$.
3. Construct the remaining phase $\Psi(x)$ by a M^{th} order polynomial using a least-squares fit of the points $\Psi(n\Delta x)$. In this way, the distribution $\beta_{\parallel}(x)$ along the aperture is constructed smoothly.

Note that $|\beta_{\|}(x)| < k_0$ is required along the aperture. Therefore, one must choose among the 2^{N_1} Orchard-Elliott solutions to satisfy this fast-wave condition when constructing the phase. Moreover, one should select the solution yielding the most desirable, e.g. smooth, values of $\alpha_{\|}(x)$ and $\beta_{\|}(x)$.

2.5.5 Compensating for Pattern Error

Interpolation from the coarse array used to construct $E(x,0)$ leads to pattern degradation. Methods such as integrated sampling have been used to compensate for such effects when designing arrays from line sources [47]. However, the task here is the converse. One can simply prescribe a new pattern that includes the error produced from the sparse sampling to compensate for the degradation.

Denote the space factor (in dB) of $E_x(x,0)$ by $G_1(\theta)$. Define an error function $e_1(\theta)$ as follows:

$$e_1(\theta) = \begin{cases} G(\theta) - G_1(\theta) & \theta \in (\theta_0, \theta_1) \\ 0 & \theta \notin (\theta_0, \theta_1) \end{cases}. \tag{2.39}$$

Here, $G(\theta)$ is the desired array factor. Both G and G_1 are normalized to achieve a peak at 0 dB. The error function $e_1(\theta)$ can fluctuate by several dB over θ. Next, define a new shaping function $S_1(\theta)$ as

$$S_1(\theta) = S(\theta) + \zeta e_1(\theta) \tag{2.40}$$

where $\zeta \in (0,1]$ is some constant. Heuristically, including the perturbation $\zeta e_1(\theta)$ in the new shaping function compensates for error by producing a new space factor $G_2(\theta)$ such that:

$$G_2(\theta) \approx G_1(\theta) + \zeta e_1(\theta) = \zeta G(\theta) + (1-\zeta) G_1(\theta) \quad \theta \in (\theta_0, \theta_1). \tag{2.41}$$

Thus, $G_2(\theta)$ is an improvement over $G_1(\theta)$. This compensation approach works best for aperture fields $E(x,0)$ with smoothly varying magnitude and phase. In general, the process is applied iteratively:

$$e_i(\theta) = \begin{cases} G(\theta) - G_i(\theta) & \theta \in (\theta_0, \theta_1) \\ 0 & \theta \notin (\theta_0, \theta_1) \end{cases} \tag{2.42a}$$

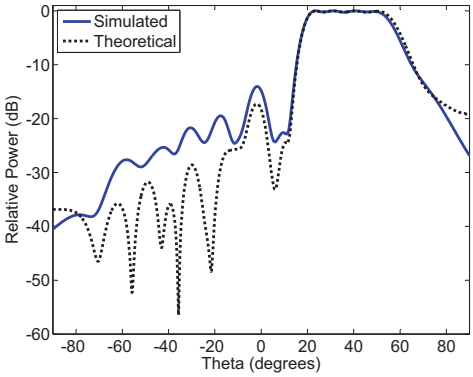

(a) LWA with flat-top beam shape in the range $\theta \in (20°, 60°)$. The simulated fraction F of radiated power to accepted power is 98.5%.

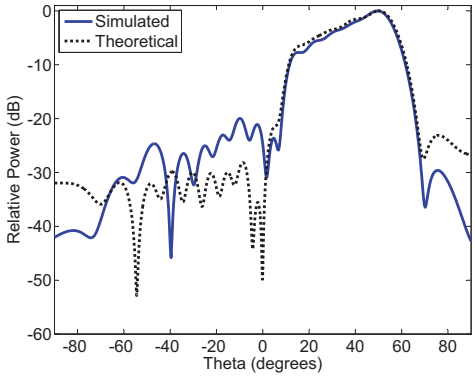

(b) LWA with $\csc^2\theta\cos\theta$ beam shape in the range $\theta \in (15°, 55°)$. The simulated fraction F of radiated power to accepted power is 97.6%.

Figure 2.14 Far-field simulations for the four antenna designs.

$$S_i(\theta) = S_{i-1}(\theta) + \zeta e_i(\theta) \tag{2.42b}$$

$$G_P(\theta) \approx G(\theta) \quad \theta \in (\theta_0, \theta_1). \tag{2.42c}$$

Here, $i \geq 2$ and P is the final iteration. The roots w_n and constant C_1 used in the i^{th} step are copied and used for the $(i+1)^{th}$ step to ensure that the perturbation of S_{i-1} does not disturb the clear maxima and minima required for the function $G_i - S_i$ [21]. From the figure, we see that after only two iterations, the space factor achieved the prescribed flat-top shape. However, note that complete control of the sidelobes is relinquished. Using sinc interpolation between the excitation coefficients, the sidelobes could be better controlled. However, linear interpolation is used to construct a more feasible aperture field.

The far-field patterns achieved during an example iterative process are provided in Fig. 2.9. The example shows is a flat-top beam with $N_1 = 3$, $N_2 = 12$, $\theta_0 = 20°$, $\theta_1 = 60°$, 0.1 dB ripple, -30 dB sidelobes, $\zeta = 1$, and P = 2. A flowchart of the iterative process is provided in Fig. 2.10.

2.6 Designs for Arbitrary Beam Shaping

Using the design procedure enumerated in Sec. 2.4, two antennas are designed here to demonstrate arbitrary beam shaping. The antennas operate at 10 GHz with length L = 24.6 cm ($8.2\lambda_0$), thickness h = 1.57 mm, and $\epsilon_{r\|} = 2.2$. The parameter F is set to 0.98. The two antennas are designed to achieve a flat-top beam shape and

a $\csc^2\theta\cos\theta$ beam shape. Both the attenuation constant $\alpha_{\|}(x)$ and propagation constant $\beta_{\|}(x)$ must be varied along these antennas to generate the desired beam shapes. The electrical parameters were computed by numerically solving the dispersion equation (2.12). This numerical alternative provides better results for aperture fields that vary somewhat rapidly, which may occur for arbitrary beam shaping.

After initially employing the techniques of Sec. 2.5, there is a slight degradation in the simulated beam patterns from COMSOL. This is due to a breakdown of the slowly-varying parameters approximation. Using a similar iterative technique to that described in Fig. 2.10, the degradation can be corrected. The only difference is that the error correction is derived from full-wave simulation results. The proposed procedure is as follows:

1. Design an impedance surface for a prescribed beam shape $S(\theta)$.
2. Simulate the impedance surface using a full-wave solver, such as COMSOL Multiphysics.
3. Calculate the error $e_{sim} = G_P(\theta) - G_{sim}(\theta)$ between the predicted beam shape $G_P(\theta)$ and the simulated beam shape $G_{sim}(\theta)$.
4. If the error is acceptable, then the design is complete. If not, then construct a new shaping function $S'(\theta) = S(\theta) + \xi e_{sim}$ and repeat the process using $S'(\theta)$.

where $\xi \in (0, 1]$ is some constant. Fig. 2.11 provides the far-field patterns of the flat-top design before and after the optimization process. Note that the error was already small, indicating that the slowly-varying parameter approximation is a good one. However, the method does provide the option of fine tuning the final radiation pattern.

The aperture distributions for the final designs are provided in Fig. 2.12(a) and 2.12(b). The derivative $\frac{d\Phi(x)}{dx}$ of the phase (normalized to k_0) is plotted. The electrical parameters are provided in Fig. 2.13. The antennas were fed in the manner depicted in Fig. 2.8. Inspection of the figure shows that the far-field patterns match well with the prescribed patterns.

2.7 Chapter Summary

In this chapter, a technique for generating an arbitrary radiation pattern from a 1-D leaky-wave antenna was demonstrated. The technique is applied to a homogenized model for impedance surfaces. The contributions of this chapters are twofold: (1) a

pattern synthesis technique that overcomes the deficiencies of the geometrical optics approximation by using an efficient gradient search method and (2) independent control of the leakage constant $\alpha_{\parallel}$ and phase constant $\beta_{\parallel}$ using impedance surfaces. The impedance surface consists of a grounded, uniaxial substrate topped by an admittance sheet. The requisite aperture fields were generated by tailoring the electrical parameters of the impedance surface using expressions derived from transverse resonance analysis.

The requisite antenna aperture fields were approximated as a discrete antenna array designed using the Orchard-Elliott synthesis method. In this way, arbitrary far fields were synthesized without the high-frequency approximations inherent to geometrical optics approaches. Moreover, iterative FFT methods were avoided and a variety of radiation patterns were demonstrated.

Four different antennas were designed. Two were designed to achieve stipulated aperture fields with constant $\beta_{\parallel}(x)$ and tapered $\alpha_{\parallel}(x)$: a constant aperture magnitude design for improved directivity, and a design with aperture magnitude distribution corresponding to a Hamming window for reduced sidelobe levels. The third and fourth antennas were designed to achieve stipulated far fields: a flat-top beam shape and a $\csc^2\theta\cos\theta$ beam shape, respectively. Full-wave simulations were used to verify the design process.

However, the proposed impedance surface topology may be difficult to fabricate, since it would require many vias inserted along the antenna to realize the shunt inductances. The next chapter explores an alternative topology that is completely planar and does not require vias. In addition, control of the far-field polarization is explored.

Chapter 3

A Cascaded, Planar Leaky-Wave Topology

3.1 Chapter Introduction

3.1.1 Review of Chapter 2

Leaky-wave modes are fast-wave modes that gradually radiate (leak) power as they travel along their supporting structure [23]. These modes are characterized by a leakage rate $\alpha_{\parallel}$, a phase constant $\beta_{\parallel}$, and a polarization. The synthesis of arbitrary, prescribed radiation patterns using 1-D leaky-wave structures has been investigated by controlling these parameters [27]. In particular, groups have explored spatially-varying the leakage rate and phase constant in one dimension (x) along the leaky-wave structure, i.e. $\alpha_{\parallel}(x)$ and $\beta_{\parallel}(x)$. These studies have featured various topologies, including substrate-integrated waveguides [29] and uniaxial, inhomogeneous dielectrics topped by sheet admittances (see Ch. 2).

3.1.2 A New Topology

However, the structures proposed in [29] and Ch. 2 require many vias. Therefore, they are more difficult to design and fabricate. Moreover, these studies did not demonstrate polarization control. In this chapter, a new leaky-wave, metasurface topology is proposed that can be fabricated using simple, planar fabrication techniques and can control the radiated polarization. The metasurface consists of cascaded, full-tensor electric sheet admittances separated by dielectric layers, backed by a ground plane. In practice, these sheet admittances can be realized using metallically-patterned sheets [48].

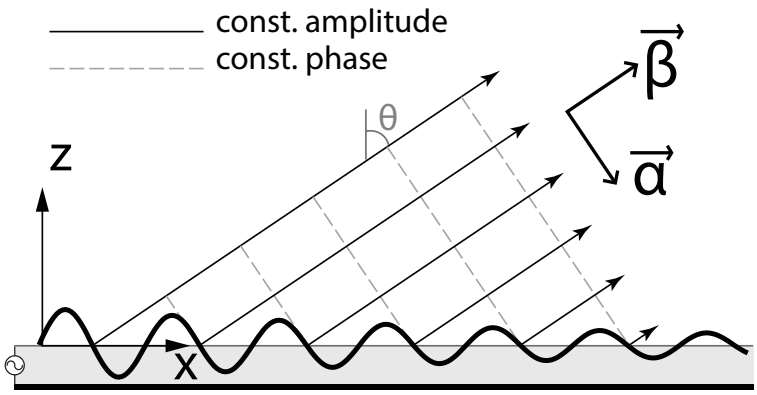

Figure 3.1 A leaky-wave mode traveling along a surface in the x direction. The mode is characterized by a wave vector $\vec{k} = (\beta_{\parallel} - j\alpha_{\parallel})\hat{x} + (\beta_{\perp} - j\alpha_{\perp})\hat{z}$. The leakage rate is given by $\alpha_{\parallel}$ while the phase distribution along the surface is characterized by $\beta_{\parallel}$.

To design the proposed inhomogeneous metasurface, the eigenmode equation for a homogeneous metasurface is first derived, as was done in Ch. 2. This equation relates the electromagnetic parameters of the structure with the supported $\alpha_{\parallel}$ and $\beta_{\parallel}$. Next, an equation for the radiated polarization is derived. These two equations are then applied to design the proposed inhomogeneous metasurface. In particular, the equations are used to find the electric sheet admittances (at each point x of the metasurface) required to achieve the required $\alpha_{\parallel}(x)$, $\beta_{\parallel}(x)$, and polarization. Mitigation of undesired surface-wave modes is also explored. Design examples are provided and verified through full-wave simulation.

3.1.3 Chapter Outline

Sec. 3.2 provides a review of pattern synthesis using leaky-wave antennas. Sec. 3.3 introduces the proposed metasurface topology. Sec. 3.4 presents a full-field eigenmode analysis of the proposed leaky-wave impedance surface, from which the transverse wavenumber $k_{\parallel}$ and the radiated polarization can be determined. Sec. 3.5 analyzes the radiated polarization. The metasurface design procedure is detailed in Sec. 3.6. Finally, simulation results are provided in Sec. 3.7 and show excellent agreement with the design goals.

3.2 A Brief Review of Leaky-Wave Pattern Synthesis

Leaky-wave modes are characterized by a wavevector $\vec{k} = \vec{\beta} - j\vec{\alpha}$ [23]. In this chapter, we investigate surfaces that vary in x only (invariant in y) supporting leaky-wave modes traveling in the x direction, i.e. 1-D leaky-wave surfaces, as depicted in Fig. 3.1. The wavevector is written as $\vec{k} = (\beta_{\parallel} - j\alpha_{\parallel})\hat{x} + (\beta_{\perp} - j\alpha_{\perp})\hat{z}$. The leakage rate is given by $\alpha_{\parallel}$ while the phase distribution along the surface is characterized by $\beta_{\parallel}$.

The aperture electric field distribution $\vec{E}_0(x)$ associated with a prescribed radiation pattern can be computed by employing the modified Orchard-Elliott procedure described in Ch. 2. Alternatively, for simple design goals such as high directivity or low sidelobes, the Fourier relationship between the aperture field and far field can be used [36]. In either case, for leaky-wave structures, the aperture field is then related to $\alpha_{\parallel}(x)$ and $\beta_{\parallel}(x)$ by well-known expressions [23]. In particular, the function $\beta_{\parallel}(x)$ is related to the phase distribution $\Phi(x)$ by

$$\beta_{\parallel}(x) = \frac{d\Phi(x)}{dx}. \tag{3.1}$$

To relate the leakage rate $\alpha_{\parallel}(x)$ to $|\vec{E}_0(x)|$, let us first note that $\alpha_{\parallel}(x)$ is related to the per-unit-length radiated power $P_{rad}(x)$ by

$$\alpha_{\parallel}(x) = \frac{P_{rad}(x)/2}{\frac{1}{F}\int_0^L P_{rad}(\zeta)d\zeta - \int_0^x P_{rad}(\zeta)d\zeta}, \tag{3.2}$$

where

$$P_{rad}(x) = 2\alpha_{\parallel}(x)P(x). \tag{3.3}$$

Here, F is the ratio of total radiated power to accepted input power and $P(x)$ is the available power within the leaky-wave structure at x. The radiated power per-unit-length $P_{rad}(x)$ at a point x is related to the tangential fields at the aperture by [49]:

$$P_{rad}(x) = \frac{1}{2}\,\mathrm{Re}\{E_{x0}(x)H_{y0}(x)^* - E_{y0}(x)H_{x0}(x)^*\}. \tag{3.4}$$

Here, the subscript 0 denotes that the fields are at the aperture. For a given polarization, the relationship between $\alpha_{\parallel}(x)$ and $|\vec{E}_0(x)|$ is provided by combining (3.2)-(3.4).

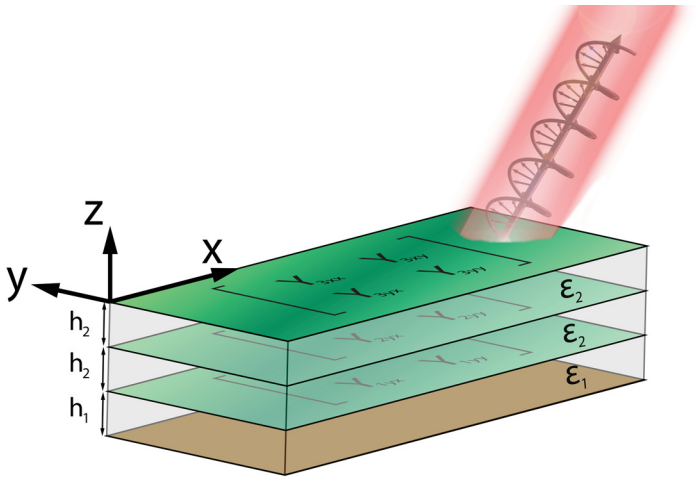

Figure 3.2 The proposed metasurface structure consisting of cascaded, full-tensor electric sheet admittances separated by dielectric layers, back by a ground plane. This structure is capable of producing circular polarization, as depicted in the figure. Three electric sheet admittances are employed in this chapter. However, this number can vary.

For TM-polarized leaky waves, $P_{rad}(x)$ is given by (see Ch. 2)

$$P_{rad}(x) = \frac{|E_{x0}(x)|^2}{2\eta_0 \cos^2\theta_r(x)}, \tag{3.5}$$

where η_0 is the free-space wave impedance and $\theta_r(x)$ is the angle of radiation defined by

$$\theta_r(x) = \sin^{-1}\frac{\beta_\parallel(x)}{k_0}. \tag{3.6}$$

For circularly-polarized waves:

$$P_{rad}(x) = \frac{1}{2}\,\mathrm{Re}\{|E_{x0}(x)|^2\frac{\omega\epsilon_0}{k_{\perp 0}(x)^*} + |E_{y0}(x)|^2\frac{k_{\perp 0}(x)^*}{\omega\mu_0}\}, \tag{3.7a}$$

$$\begin{aligned} P_{rad}(x) &= \frac{1}{2}|E_{x0}(x)|^2\,\mathrm{Re}\{\frac{\omega\epsilon_0}{k_{\perp 0}(x)^*} + \sec^2\theta_r(x)\frac{k_{\perp 0}(x)^*}{\omega\mu_0}\} \\ &\approx \frac{|E_{x0}(x)|^2}{\eta_0\cos\theta_r(x)} = \frac{|E_{x0}(x)|^2 + |E_{y0}(x)|^2}{2\eta_0\cos\theta_r(x)}, \end{aligned} \tag{3.7b}$$

where $k_{\perp 0}(x) = \sqrt{k_0^2 - \beta_\parallel^2(x)}$.

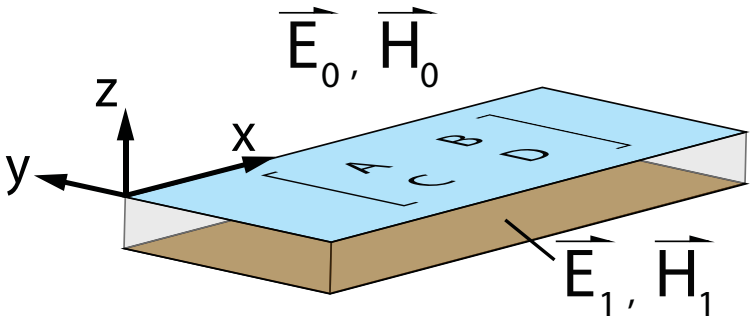

Figure 3.3 A conductor-backed dielectric topped by a boundary condition that relates the tangential electric and magnetic fields on either side of the sheet by an ABCD matrix. The layered sheets depicted in Fig. 3.2 can be analyzed simply as this equivalent ABCD boundary.

3.3 The Metasurface Topology

The proposed leaky-wave metasurface is depicted in Fig. 3.2. The structure consists of cascaded, full-tensor electric admittance sheets separated by dielectric layers, backed by a ground plane. Each sheet is characterized by a 2x2 tensor $\mathbf{Y}_n$:

$$\mathbf{Y}_n = \begin{bmatrix} Y_{nxx} & Y_{nxy} \\ Y_{nyx} & Y_{nyy} \end{bmatrix}, \tag{3.8}$$

where the subscript n denotes the n^{th} sheet. The tensor (3.8) relates the tangential electric field $\vec{E}_{nt}$ at the sheet to the surface current $\vec{J}_{ns}$ on the sheet:

$$\vec{J}_{ns} = \mathbf{Y}_n \vec{E}_{nt}, \tag{3.9}$$

where the subscript t denotes the transverse component. The subscript s emphasizes that we are referring to the surface current. In practice, these admittance sheets can be realized using patterned metallic sheets [48].

To generate prescribed radiation patterns, the sheet admittances $\mathbf{Y}_n$ must vary inhomogeneously as a function of x. The inhomogeneous sheet admittances are represented by $\mathbf{Y}_n(x)$ and are assumed to be a function of x only (invariant in y). The goal is to find the functions $\mathbf{Y}_n(x)$ that achieve the required leakage rate $\alpha_\parallel(x)$ and phase constant $\beta_\parallel(x)$ for a prescribed far-field pattern, as in Ch. 2. To relate the admittance sheet functions $\mathbf{Y}_n(x)$ to $\alpha_\parallel(x)$ and $\beta_\parallel(x)$, the eigenmode equation of a homogeneous structure is applied. Although the eigenmode equation is derived using a homogeneous structure, its application to inhomogenous structures works well if the

admittance sheets vary slowly with x.

3.4 The Eigenmode (Dispersion) Equation

In this section, the sheet admittances $\mathbf{Y}_n$ are related to the leakage rate $\alpha_\parallel$ and phase constant $\beta_\parallel$ through eigenmode analysis. The eigenmode analysis can be performed in a variety of ways. In this chapter, the leaky-wave metasurface is equated to an ABCD boundary condition atop a single, conductor-backed, dielectric layer, as shown in Fig. 3.3. The boundary condition relates the tangential fields in the free-space above $(\vec{E}_0, \vec{H}_0)$ to those in the bottommost dielectric layer $(\vec{E}_1, \vec{H}_1)$:

$$\begin{bmatrix} E_{x1} \\ E_{y1} \\ H_{x1} \\ H_{y1} \end{bmatrix} = \begin{bmatrix} \mathbf{A} & \mathbf{B} \\ \mathbf{C} & \mathbf{D} \end{bmatrix} \begin{bmatrix} E_{x0} \\ E_{y0} \\ H_{x0} \\ H_{y0} \end{bmatrix}. \tag{3.10}$$

Here, **A**, **B**, **C**, and **D** are each a 2x2 matrix [9]. For example, the matrix **A** is given by:

$$\mathbf{A} = \begin{bmatrix} A_{xx} & A_{xy} \\ A_{yx} & A_{yy} \end{bmatrix}. \tag{3.11}$$

The relationship between the ABCD matrix and the cascaded sheets will be provided later in Subsection 3.4.1. For generality, the analysis that follows will simply explore boundary condition (3.10).

The fields within each layer can be decomposed into four plane waves: $+z$-directed and $-z$-directed plane waves of TM^z and TE^z polarizations [50]. Each TM plane wave is characterized by an electric Hertz vector potential $\vec{\Pi}$ along the $\hat{z}$-axis: $\vec{\Pi}^\pm = \Psi^\pm e^{\mp jk_{\perp}z}\hat{z}$. The $+\hat{z}$-directed waves and $-\hat{z}$-directed waves are denoted by the superscripts $+$ and $-$, respectively. Similarly, each TE plane wave is characterized by a magnetic Hertz vector potential $\vec{\Pi}_m$ along the $\hat{z}$-axis: $\vec{\Pi}_m^\pm = \Lambda^\pm e^{\mp jk_{\perp}z}\hat{z}$. Therefore, the fields can be written as:

$$\vec{E}_i^\pm = \left[\frac{\partial}{\partial z}\nabla_\parallel \Psi_i^\pm + |k_\parallel|^2 \Psi_i^\pm \hat{z} - j\omega\mu_0(\nabla_\parallel \Lambda_i^\pm \times \hat{z})\right] e^{\mp jk_{\perp i}z}, \tag{3.12a}$$

$$\vec{H}_i^{\pm} = \left[\frac{\partial}{\partial z}\nabla_{\parallel}\Lambda_i^{\pm} + |k_{\parallel}|^2\Lambda_i^{\pm}\hat{z} + j\omega\epsilon_i(\nabla_{\parallel}\Psi_i^{\pm}\times\hat{z})\right]e^{\mp jk_{\perp i}z}, \tag{3.12b}$$

where $\nabla_{\parallel} = {}^{\partial}/_{\partial_x}\hat{x} + {}^{\partial}/_{\partial_y}\hat{y}$. Recall that the x-axis is aligned with the transverse wavevector $\vec{k_{\parallel}}$, such that $\vec{k_{\parallel}} = k_{\parallel}\hat{x}$. The subscript i identifies the i^{th} region. The conductor-backed dielectric will be denoted as Region 1 and the free-space above the metasurface is denoted as Region 0. The radiation condition [50] dictates that $\Psi_0^- = \Lambda_0^- = 0$. From the phase matching condition, the transverse wavevector $\vec{k_{\parallel}}$ in each region must be equal. The separation relation can be written as $|k_{\parallel}|^2 + k_{\perp i}^2 = \omega^2\mu\epsilon_i$ [49].

According to (3.12), the TM components of the fields are determined solely by Ψ, while the TE components are determined solely by Λ. By noting that $E_{zi}^{\pm} = |k_{\parallel}|^2\Psi_i^{\pm}e^{\mp jk_{\perp i}z}$ and $H_{zi}^{\pm} = |k_{\parallel}|^2\Lambda_i^{\pm}e^{\mp jk_{\perp i}z}$, the fields can be alternatively written as:

$$\vec{E}_i^{\pm} = \left[\frac{\nabla_{\parallel}}{k_{\parallel}^2}\frac{\partial E_{zi}^{\pm}}{\partial z} + E_{zi}^{\pm}\hat{z} - j\omega\mu_0\frac{1}{k_{\parallel}^2}(\nabla_{\parallel}\times H_{zi}^{\pm}\hat{z})\right]e^{\mp jk_{\perp i}z}, \tag{3.13a}$$

$$\vec{H}_i^{\pm} = \left[\frac{\nabla_{\parallel}}{k_{\parallel}^2}\frac{\partial H_{zi}^{\pm}}{\partial z} + H_{zi}^{\pm}\hat{z} + j\omega\epsilon_i\frac{1}{k_{\parallel}^2}(\nabla_{\parallel}\times E_{zi}^{\pm}\hat{z})\right]e^{\mp jk_{\perp i}z}. \tag{3.13b}$$

For the plane waves in this problem, we can write $\nabla_{\parallel} = -j\vec{k_{\parallel}} = -jk_{\parallel}\hat{x}$:

$$\vec{E}_i^{\pm} = \left[\mp\frac{k_{\perp i}}{k_{\parallel}}E_{zi}^{\pm}\hat{x} + E_{zi}^{\pm}\hat{z} + \frac{\omega\mu_0}{k_{\parallel}}H_{zi}^{\pm}\hat{y}\right]e^{\mp jk_{\perp i}z}, \tag{3.14a}$$

$$\vec{H}_i^{\pm} = \left[\mp\frac{k_{\perp i}}{k_{\parallel}}H_{zi}^{\pm}\hat{x} + H_{zi}^{\pm}\hat{z} - \frac{\omega\epsilon_i}{k_{\parallel}}E_{zi}^{\pm}\hat{y}\right]e^{\mp jk_{\perp i}z}. \tag{3.14b}$$

Combining (3.10) and (3.14) yields the following matrix equation:

$$\begin{bmatrix} \frac{k_{\perp 1}}{k_{\parallel}}E_{z1}^{-}e^{jk_{\perp 1}h} - \frac{k_{\perp 1}}{k_{\parallel}}E_{z1}^{+}e^{-jk_{\perp 1}h} \\ \frac{\omega\mu_0}{k_{\parallel}}H_{z1}^{-}e^{jk_{\perp 1}h} + \frac{\omega\mu_0}{k_{\parallel}}H_{z1}^{+}e^{-jk_{\perp 1}h} \\ \frac{k_{\perp 1}}{k_{\parallel}}H_{z1}^{-}e^{jk_{\perp 1}h} - \frac{k_{\perp 1}}{k_{\parallel}}H_{z1}^{+}e^{-jk_{\perp 1}h} \\ -\frac{\omega\epsilon_1}{k_{\parallel}}E_{z1}^{-}e^{jk_{\perp 1}h} - \frac{\omega\epsilon_1}{k_{\parallel}}E_{z1}^{+}e^{-jk_{\perp 1}h} \end{bmatrix} = \begin{bmatrix} \mathbf{A} & \mathbf{B} \\ \mathbf{C} & \mathbf{D} \end{bmatrix} \begin{bmatrix} -\frac{k_{\perp 0}}{k_{\parallel}}E_{z0}^{+}e^{-jk_{\perp 0}h} \\ \frac{\omega\mu_0}{k_{\parallel}}H_{z0}^{+}e^{-jk_{\perp 0}h} \\ \frac{-k_{\perp 0}}{k_{\parallel}}H_{z0}^{+}e^{-jk_{\perp 0}h} \\ -\frac{\omega\epsilon_0}{k_{\parallel}}E_{z0}^{+}e^{-jk_{\perp 0}h} \end{bmatrix}. \tag{3.15}$$

The vanishing tangential electric field at the ground plane requires that:

$$E_x(z=0) = k_\parallel k_{\perp 1} E_{z1}^- - k_\parallel k_{\perp 1} E_{z1}^+ = 0, \tag{3.16a}$$

$$E_y(z=0) = \omega\mu_1 k_\parallel H_{z1}^- + \omega\mu_1 k_\parallel H_{z1}^+ = 0. \tag{3.16b}$$

Substituting condition (3.16) into (3.15), and eliminating the common $k_\parallel$ terms yields:

$$\begin{bmatrix} j2E_{z1}^- k_{\perp 1} \sin k_{\perp 1} h \\ j2H_{z1}^- \omega\mu_1 \sin k_{\perp 1} h \\ 2H_{z1}^- k_{\perp 1} \cos k_{\perp 1} h \\ -2E_{z1}^- \omega\epsilon_1 \cos k_{\perp 1} h \end{bmatrix} = \begin{bmatrix} \mathbf{A} & \mathbf{B} \\ \mathbf{C} & \mathbf{D} \end{bmatrix} \begin{bmatrix} -k_{\perp 0} E_{z0}^+ e^{-jk_{\perp 1}h} \\ \omega\mu_0 H_{z0}^+ e^{-jk_{\perp 1}h} \\ -k_{\perp 0} H_{z0}^+ e^{-jk_{\perp 1}h} \\ -\omega\epsilon_0 E_{z0}^+ e^{-jk_{\perp 1}h} \end{bmatrix} \tag{3.17}$$

Eq. (3.17) can be reduced to the eigenmode equation featured in (3.18):

$$\begin{bmatrix} \left[j\frac{A_{xx}k_{\perp 0}}{k_{\perp 1}} + j\frac{B_{xy}\omega\epsilon_0}{k_{\perp 1}}\right]\cot(k_{\perp 1}h) + \left[-\frac{C_{yx}k_{\perp 0}}{\omega\epsilon_1} - \frac{D_{yy}\omega\epsilon_0}{\omega\epsilon_1}\right] & \left[j\frac{B_{xx}k_{\perp 0}}{k_{\perp 1}} - j\frac{A_{xy}\omega\mu_0}{k_{\perp 1}}\right]\cot(k_{\perp 1}h) + \left[-\frac{D_{yx}k_{\perp 0}}{\omega\epsilon_1} + \frac{C_{yy}\omega\mu_0}{\omega\epsilon_1}\right] \\ \left[j\frac{A_{yx}k_{\perp 0}}{\omega\mu_1} + j\frac{B_{yy}\omega\epsilon_0}{\omega\mu_1}\right]\cot(k_{\perp 1}h) + \left[\frac{C_{xx}k_{\perp 0}}{k_{\perp 1}} + \frac{D_{xy}\omega\epsilon_0}{k_{\perp 1}}\right] & \left[j\frac{B_{yx}k_{\perp 0}}{\omega\mu_1} - j\frac{A_{yy}\omega\mu_0}{\omega\mu_1}\right]\cot(k_{\perp 1}h) + \left[\frac{D_{xx}k_{\perp 0}}{k_{\perp 1}} - \frac{C_{xy}\omega\mu_0}{k_{\perp 1}}\right] \end{bmatrix} \begin{bmatrix} E_{z0}^+ \\ H_{z0}^+ \end{bmatrix} = \begin{bmatrix} 0 \\ 0 \end{bmatrix} \tag{3.18}$$

$$\left(\left[j\frac{A_{xx}k_{\perp 0}}{k_{\perp 1}} + j\frac{B_{xy}\omega\epsilon_0}{k_{\perp 1}}\right]\cot(k_{\perp 1}h) + \left[-\frac{C_{yx}k_{\perp 0}}{\omega\epsilon_1} - \frac{D_{yy}\omega\epsilon_0}{\omega\epsilon_1}\right]\right)\left(\left[j\frac{B_{yx}k_{\perp 0}}{\omega\mu_1} - j\frac{A_{yy}\omega\mu_0}{\omega\mu_1}\right]\cot(k_{\perp 1}h) + \left[\frac{D_{xx}k_{\perp 0}}{k_{\perp 1}} - \frac{C_{xy}\omega\mu_0}{k_{\perp 1}}\right]\right),$$
$$-\left(\left[j\frac{B_{xx}k_{\perp 0}}{k_{\perp 1}} - j\frac{A_{xy}\omega\mu_0}{k_{\perp 1}}\right]\cot(k_{\perp 1}h) + \left[-\frac{D_{yx}k_{\perp 0}}{\omega\epsilon_1} + \frac{C_{yy}\omega\mu_0}{\omega\epsilon_1}\right]\right)\left(\left[j\frac{A_{yx}k_{\perp 0}}{\omega\mu_1} + j\frac{B_{yy}\omega\epsilon_0}{\omega\mu_1}\right]\cot(k_{\perp 1}h) + \left[\frac{C_{xx}k_{\perp 0}}{k_{\perp 1}} + \frac{D_{xy}\omega\epsilon_0}{k_{\perp 1}}\right]\right) = 0. \tag{3.19}$$

The dispersion equation (3.19) above is derived by setting the determinant of the matrix featured in (3.18) equal to 0.

3.4.1 Relating to Sheet Admittances

The ABCD parameters featured in (3.18) and (3.19) are easily related to the cascaded electric sheet admittances $\mathbf{Y_n}$. This was demonstrated in [48] for normal incidence ($\vec{k}_\parallel = 0$). Using a similar derivation for oblique incidence, with $\vec{k_\parallel} = k_\parallel \hat{x}$, the matrix is given by:

$$\begin{aligned} \begin{pmatrix} \mathbf{A} & \mathbf{B} \\ \mathbf{C} & \mathbf{D} \end{pmatrix} = \begin{pmatrix} \mathbf{I} & \mathbf{0} \\ \mathbf{nY_3} & \mathbf{I} \end{pmatrix} \begin{pmatrix} \cos(k_{\perp 2}h_2)\mathbf{I} & -j\mathbf{Z}\sin(k_{\perp 2}h_2) \\ -j\mathbf{Z}^{-1}\sin(k_{\perp 2}h_2) & \cos(k_{\perp 2}h_2)\mathbf{I} \end{pmatrix} \cdots \\ \begin{pmatrix} \mathbf{I} & \mathbf{0} \\ \mathbf{nY_2} & \mathbf{I} \end{pmatrix} \begin{pmatrix} \cos(k_{\perp 2}h_2)\mathbf{I} & -j\mathbf{Z}\sin(k_{\perp 2}h_2) \\ -j\mathbf{Z}^{-1}\sin(k_{\perp 2}h_2) & \cos(k_{\perp 2}h_2)\mathbf{I} \end{pmatrix} \begin{pmatrix} \mathbf{I} & \mathbf{0} \\ \mathbf{nY_1} & \mathbf{I} \end{pmatrix}, \end{aligned} \tag{3.20}$$

where

$$\mathbf{Z} = \begin{bmatrix} 0 & -\eta^{TM} \\ \eta^{TE} & 0 \end{bmatrix}, \tag{3.21}$$

$$\eta^{TM} = \frac{k_{\perp 2}}{\omega \epsilon_2}, \tag{3.22a}$$

$$\eta^{TE} = \frac{\omega \mu_0}{k_{\perp 2}}. \tag{3.22b}$$

Here, the subscript 2 refers to the dielectric spacer layer (see Fig. 3.2).

3.4.2 Special Case: Isotropic Sheet Admittances

For isotropic sheet admittances, the ABCD parameters are of the following form:

$$\mathbf{A} = A_{xx}\mathbf{I}, \tag{3.23a}$$

$$\mathbf{B} = B_{yx}\mathbf{n}, \tag{3.23b}$$

$$\mathbf{C} = C_{yx}\mathbf{n}, \tag{3.23c}$$

$$\mathbf{D} = D_{xx}\mathbf{I}, \tag{3.23d}$$

where $\mathbf{I}$ is the 2-dimensional identity matrix and $\mathbf{n}$ is given by:

$$\mathbf{n} = \begin{bmatrix} 0 & -1 \\ 1 & 0 \end{bmatrix}. \tag{3.24}$$

Under condition (3.23), Eq. (3.19) decomposes into two separable equations: TM and TE dispersion equations. The TM dispersion equation is given by

$$\left[jA_{xx}\frac{k_{\perp 0}}{2k_{\perp 1}} + jB_{xy}\frac{\omega \epsilon_0}{2k_{\perp 1}} \right] \cot(k_{\perp 1}h) + \left[-C_{yx}\frac{k_{\perp 0}}{2\omega \epsilon_1} - D_{yy}\frac{\omega \epsilon_0}{2\omega \epsilon_1} \right] = 0, \tag{3.25}$$

and the TE dispersion equation is given by

$$\left[j\frac{B_{yx}k_{\perp 0}}{\omega \mu_1} - j\frac{A_{yy}\omega \mu_0}{\omega \mu_1} \right] \cot(k_{\perp 1}h) + \left[\frac{D_{xx}k_{\perp 0}}{k_{\perp 1}} - \frac{C_{xy}\omega \mu_0}{k_{\perp 1}} \right] = 0. \tag{3.26}$$

If a single electric admittance sheet is used, then (3.19) reduces to a well-known form [51]:

$$\left(-j\frac{\omega\epsilon_1}{k_{\perp 1}}\cot(k_{\perp 1}h)+Y_{xx}+\frac{\omega\epsilon_0}{k_{\perp 0}}\right)\left(-j\frac{k_{\perp 1}}{\omega\mu_1}\cot(k_{\perp 1}h)+\frac{k_{\perp 0}}{\omega\mu_0}+Y_{yy}\right)=Y_{xy}Y_{yx}. \quad (3.27)$$

3.5 Polarization Analysis

In addition to controlling $k_\parallel$, polarization can also be controlled using the proposed metasurface. Indeed, a relationship between E_{z0}/H_{z0} and $\mathbf{Y}_n$ can be derived using Eq. (3.18):

$$\frac{E_{z0}}{H_{z0}}=-\frac{F_{12}}{F_{11}}=-\frac{F_{22}}{F_{21}}, \quad (3.28)$$

where

$$F_{11}=\left[j\frac{A_{xx}k_{\perp 0}}{k_{\perp 1}}+j\frac{B_{xy}\omega\epsilon_0}{k_{\perp 1}}\right]\cot(k_{\perp 1}h)+\left[-\frac{C_{yx}k_{\perp 0}}{\omega\epsilon_1}-\frac{D_{yy}\omega\epsilon_0}{\omega\epsilon_1}\right], \quad (3.29)$$

$$F_{12}=\left[j\frac{B_{xx}k_{\perp 0}}{k_{\perp 1}}-j\frac{A_{xy}\omega\mu_0}{k_{\perp 1}}\right]\cot(k_{\perp 1}h)+\left[-\frac{D_{yx}k_{\perp 0}}{\omega\epsilon_1}+\frac{C_{yy}\omega\mu_0}{\omega\epsilon_1}\right], \quad (3.30)$$

$$F_{21}=\left[j\frac{A_{yx}k_{\perp 0}}{\omega\mu_1}+j\frac{B_{yy}\omega\epsilon_0}{\omega\mu_1}\right]\cot(k_{\perp 1}h)+\left[\frac{C_{xx}k_{\perp 0}}{k_{\perp 1}}+\frac{D_{xy}\omega\epsilon_0}{k_{\perp 1}}\right], \quad (3.31)$$

$$F_{22}=\left[j\frac{B_{yx}k_{\perp 0}}{\omega\mu_1}-j\frac{A_{yy}\omega\mu_0}{\omega\mu_1}\right]\cot(k_{\perp 1}h)+\left[\frac{D_{xx}k_{\perp 0}}{k_{\perp 1}}-\frac{C_{xy}\omega\mu_0}{k_{\perp 1}}\right]. \quad (3.32)$$

The radiated polarization of a leaky-wave mode is fully characterized by this ratio E_{z0}/H_{z0}, i.e. the TM-to-TE ratio. Indeed, the electric field radiated by the structure (shown in Fig. 3.2) is given by [36]:

$$E_\theta(r,\theta,\phi)\simeq j\frac{ke^{-jkr}}{2\pi r}(f_x\cos\phi+f_y\sin\phi), \quad (3.33a)$$

$$E_\phi(r,\theta,\phi)\simeq j\frac{ke^{-jkr}}{2\pi r}\cos\theta(-f_x\sin\phi+f_y\cos\phi), \quad (3.33b)$$

where f_x and f_y are the tangential components of the electric field spectrum $\vec{f}$ at the aperture:

$$\vec{f}(\beta_\parallel,\beta_y)=e^{j\beta_\perp z}\int_{-\infty}^{+\infty}\int_{-\infty}^{+\infty}\vec{E}_0(x,y,z)e^{j(\beta_\parallel x+\beta_y y)}dxdy. \quad (3.34)$$

For the $\hat{x}$-directed, 1-D leaky-wave metasurfaces considered in this chapter, $\phi=0$.

The radiated polarization is therefore determined by the ratio f_x/f_y and equivalently by

E_{x0}/E_{y0}. But the ratio E_{x0}/E_{y0} is related to E_{z0}/H_{z0} using (3.14):

$$\frac{E_{x0}}{E_{y0}} = -\frac{k_{\perp 0}}{\omega\mu_0}\frac{E_{z0}^{+}}{H_{z0}^{+}} = -\frac{k_{\perp 0}}{\omega\mu_0}\frac{E_{z0}}{H_{z0}}. \tag{3.35}$$

Therefore, the radiated polarization is fully characterized by the ratio E_{z0}/H_{z0}.

3.5.1 Special Case: Circular Polarization

From (3.33), circular polarization at an angle θ requires that:

$$\frac{E_\theta}{E_\phi} = \sec\theta\frac{f_x}{f_y} = j \quad \text{(for RHCP)}, \tag{3.36a}$$

$$\frac{E_\theta}{E_\phi} = \sec\theta\frac{f_x}{f_y} = -j \quad \text{(for LHCP)}. \tag{3.36b}$$

Combining (3.33), (3.34) and (3.36), the ratio E_{x0}/E_{y0} required for circular polarization is given by:

$$\frac{E_{x0}}{E_{y0}} = j\cos\theta \quad \text{(for RHCP)}, \tag{3.37a}$$

$$\frac{E_{x0}}{E_{y0}} = -j\cos\theta \quad \text{(for LHCP)}. \tag{3.37b}$$

Combining (3.35) and (3.37) yields

$$\frac{E_{z0}}{H_{z0}} = -j\frac{\omega\mu_0}{k_{\perp 0}}\cos\theta \quad \text{(for RHCP)}, \tag{3.38a}$$

$$\frac{E_{z0}}{H_{z0}} = j\frac{\omega\mu_0}{k_{\perp 0}}\cos\theta \quad \text{(for LHCP)}. \tag{3.38b}$$

3.6 Metasheet Design

Substituting (3.20) into (3.19) and (3.28) yields the two equations that must be satisfied to achieve a leaky-wave mode of prescribed $\alpha_\parallel$, $\beta_\parallel$, and TM-to-TE ratio (polarization). In the metasurface design procedure, these equations are used to find the electric sheet admittances $\mathbf{Y}_n(x)$ required to achieve a prescribed $\alpha_\parallel(x)$, $\beta_\parallel(x)$, and polarization. Although (3.20) and (3.19) were derived for a homogeneous structure, their application to inhomogeneous structures works well if the admittance sheets vary slowly with x.

However, it is difficult to solve for the values of $\mathbf{Y_n}(x)$ analytically. Here, a nonlinear optimization algorithm is used. In general, there are many solutions to this system of non-

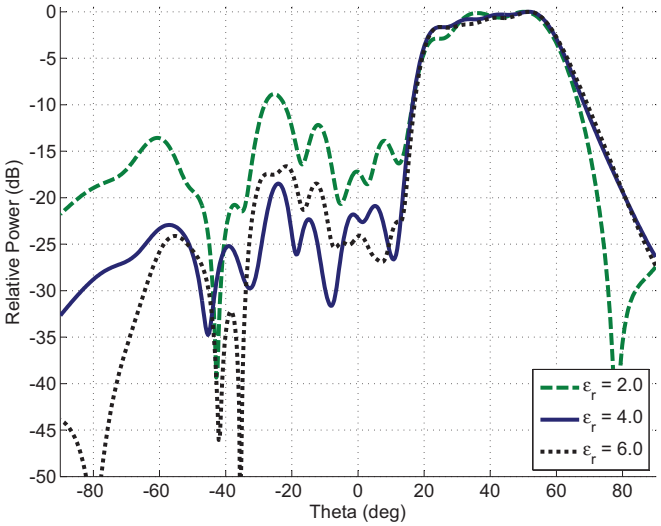

Figure 3.4 Simulated far-field elevation patterns for three metasurface designs employing different spacer permittivities ϵ_2. The prescribed pattern for each is a TM-polarized flattop in the range $\theta \in (20°, 60°)$. The design with $\epsilon_{r2} = 2$ exhibits the most ripple in the shaped region.

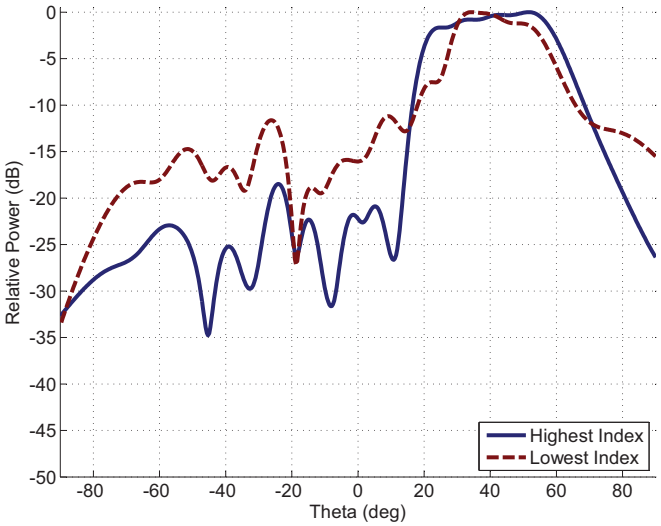

Figure 3.5 Simulated far-field elevation patterns for two metasurface designs employing $\epsilon_2 = 4\epsilon_0$. The prescribed pattern for each is a TM-polarized flattop in the range $\theta \in (20°, 60°)$. The first design employs $\mathbf{Y_n}$ corresponding to the highest surface wave index at each point x. The second design employs $\mathbf{Y_n}$ corresponding to the lowest surface wave index at each point x. Inspection of the plot shows that the first design yields the better pattern.

linear equations. Analysis of dispersion equation (3.19) reveals that each of these solutions will support an additional, undesired, surface wave mode. To minimize degradation of the far-field pattern, the solution generating the surface wave mode of highest index should be

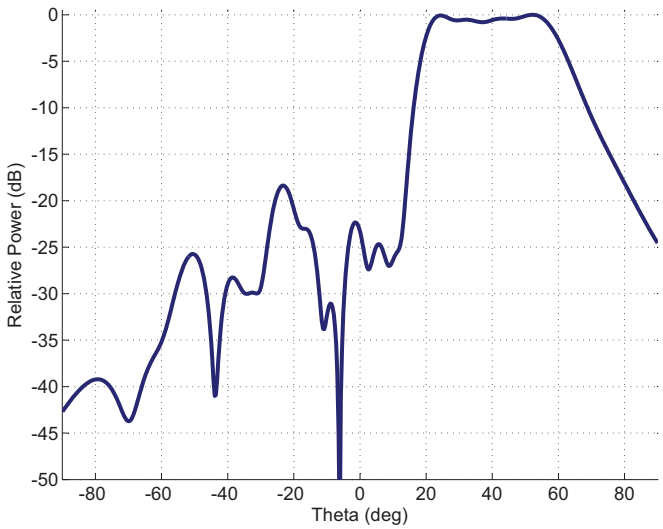

Figure 3.6 Simulated far-field elevation pattern of the first metasurface design after compensating for pattern degradation. The prescribed pattern for each is a TM-polarized flattop in the range $\theta \in (20°, 60°)$. The metasurface employs the following parameters: $f = 10$ GHz, $L = 24.6$ cm, $h_1 = 1$ mm, $\epsilon_1 = \epsilon_0$, $\epsilon_2 = 4\epsilon_0$, and $h_2 = 1.27$ mm.

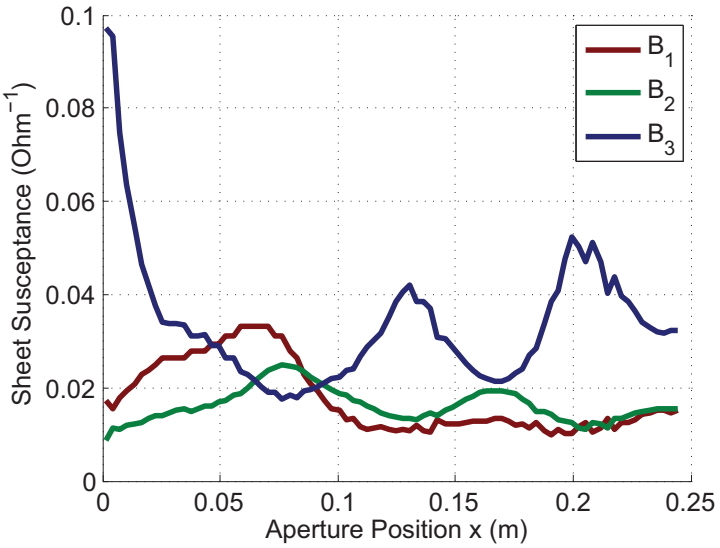

Figure 3.7 Sheet susceptance parameters for the first metasurface design (see Fig. 3.6). Each admittance sheet is isotropic and therefore characterized by a scalar susceptance value.

chosen at each point x. To understand this, let us consider Fourier theory. For an infinite aperture, the visible region ($|\beta_{\|}| < k_0$) of the angular spectrum $f_x(\beta_{\|} = k_0 \sin\theta)$ is unaffected by the presence of surface wave modes. However, a truncation of the aperture will spread the spectrum of the surface wave mode across the light cone (propagating spectrum) [36]. Physically, this means that the surface wave radiates from the edges of the metasurface aperture. However, the degradation is minimized by selecting a solution that generates the

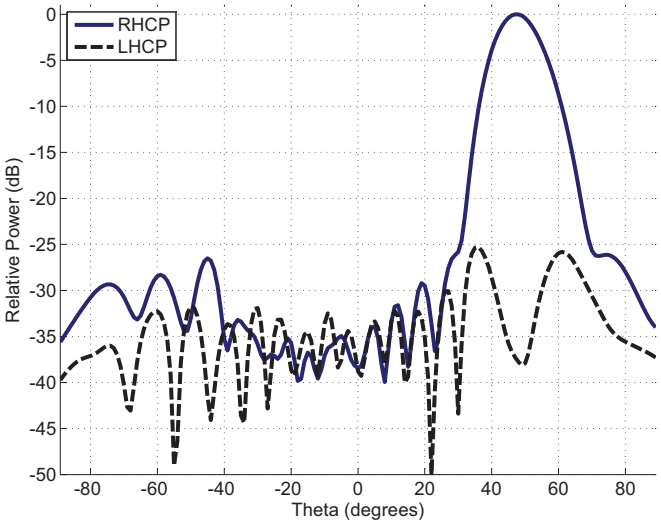

Figure 3.8 Simulated far-field elevation patterns for the second metasurface design, which is designed to generate an RHCP beam at 50° in elevation. The prescribed aperture magnitude distribution is that of a Hamming window to maintain low sidelobes. The metasurface employs the following parameters: $f = 10$ GHz, $L = 24.6$ cm, $h_1 = 1$ mm, $\epsilon_1 = \epsilon_0$, $\epsilon_2 = 10.2\epsilon_0$, and $h_2 = 1.27$ mm.

surface wave with the highest effective index.

The systematic procedure used to design the proposed leaky-wave metasurfaces is as follows:

1. Select a thickness for each dielectric spacer layer. In this chapter, two spacer layers are chosen with equal thickness h_2.
2. Select a permittivity for each dielectric spacer layer. Here, the dielectrics are chosen to have the same permittivity ϵ_2.
3. Numerically, determine the values of the sheet admittances $\mathbf{Y_n}(x)$ that satisfy the dispersion equation (3.19) and the desired TM-to-TE ratio $^{E_{z0}}/_{H_{z0}}$ given by (3.28) at each point x.
4. In general, there are multiple solutions. To minimize degradation of the far-field pattern, select the solution that generates the surface wave mode of highest $|k_\parallel|$ at each point x.

3.7 Design Examples

In this section, two design examples are provided. The first is a metasurface generating a TM-polarized, flattop radiation pattern from $\theta = 20°$ to $\theta = 60°$ in elevation (0° is broadside).

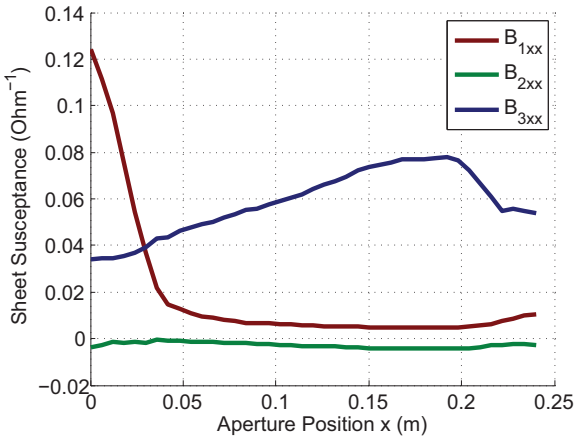

(a) B_{xx} components

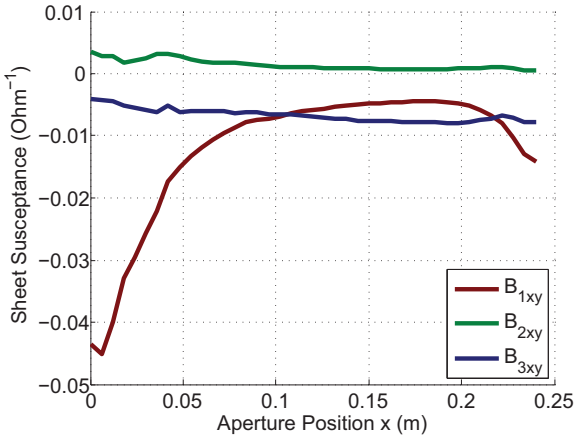

(b) B_{xy} components

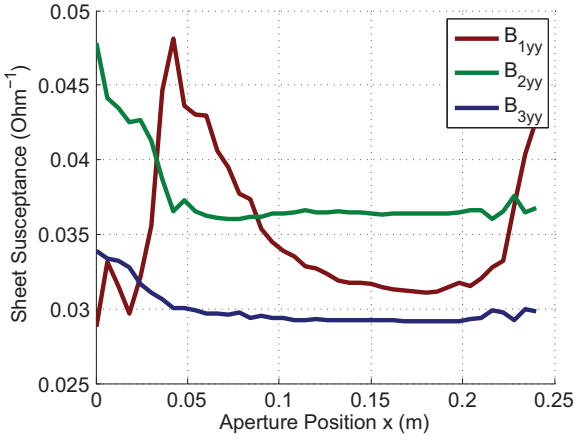

(c) B_{yy} components

Figure 3.9 Sheet susceptance parameters for the second metasurface design (see Fig. 3.8). Each admittance sheet is characterized by a symmetric tensor ($B_{xy} = B_{yx}$).

The metasurface consists of three sheet admittances and dielectric layers, as shown in Fig. 3.2. The metasurface parameters are selected as follows:

- Frequency (f) = 10 GHz
- Antenna Length (L) = 24.6 cm = 8.2 λ_0
- h_1 = 1 mm
- h_2 = 1.27 mm
- $\epsilon_1 = \epsilon_0$

A variety of spacer permittivities ϵ_2 were considered for the design. The requisite tensors $\mathbf{Y_n}(x)$ for each of the considered permittivities ϵ_2 were calculated using the aforementioned design procedure. During this process, it was observed that the index of the undesired surface wave typically increases with ϵ_2. Therefore, the far-field pattern is expected to improve with increasing permittivity ϵ_2. Fig. 3.4 provides the far-field elevation pattern for each ϵ_2, simulated using the commercial electromagnetic solver COMSOL Multiphysics. As expected, the results show that the radiation pattern for the lowest relative permittivity ($\epsilon_{r2} = 2$) exhibits the most degradation in the shaped region. However, there is little improvement for permittivities higher than $\epsilon_{r2} = 4$. Ultimately, $\epsilon_{r2} = 4$ was chosen for the metasurface design.

Simulations for two different metasurface designs using $\epsilon_{r2} = 4$ are shown in Fig. 3.5. The first design finds the $\mathbf{Y_n}(x)$ that maximize the surface wave index at each point x. The second design finds the $\mathbf{Y_n}(x)$ that minimize the surface wave index at each point x. The radiation patterns clearly show that the first method yields a significantly improved radiation pattern, thereby justifying Step 4 of the design procedure.

Still, even the best radiation patterns in Figs. 3.4 and 3.5 exhibit some degradation. This inherent degradation stems from the application of homogeneous analysis to inhomogeneous structures. However, one can iteratively prescribe a desired shaping function to compensate for error, as discussed in Ch. 2. Figure 3.6 presents the far-field results of the final metasurface design, which employed this iterative technique. The figure depicts a high-fidelity, flattop radiation pattern. The sheet suspectance values employed in the design are provided in Fig. 3.7.

The second design example is a metasurface generating right-hand circular polarization (RHCP) at $\theta = 50^\circ$ in elevation while maintaining low sidelobes. To reduce the sidelobes, an aperture magnitude distribution corresponding to a Hamming window is prescribed:

$$|E_\parallel(x)| = 0.54 + 0.46\cos\left(\frac{2\pi(x - L/2)}{L}\right). \tag{3.39}$$

The simulated far-field pattern is provided in Fig. 3.8. The plot is decomposed into RHCP and LHCP components. From the figure, it is clear that RHCP radiation is achieved at

$\theta = 50^\circ$, while LHCP is suppressed. The sheet suspectance values employed in the design are provided in Fig. 3.9.

3.8 Chapter Summary

In this chapter, a new metasurface topology is proposed and analyzed for synthesizing prescribed far-field patterns. The metasurface consists of cascaded, full-tensor electric sheet admittances (anisotropically-patterned metallic sheets) separated by dielectric layers, backed by a ground plane. This topology is advantageous due to its simple, planar fabrication as well as its ability to control polarization. Eigenmode analysis is performed and employed to develop a systemic design procedure.

Two design examples are provided. The first is a metasurface generating a TM-polarized, flattop radiation pattern from $\theta = 20^\circ$ to $\theta = 60^\circ$ in elevation. The second is a metasurface generating right-hand circular polarized beam at $\theta = 50^\circ$ in elevation while maintaining low sidelobes. Full-wave simulation results demonstrate that prescribed radiation patterns can be synthesized with high fidelity.

Chapter 4

An Alternative to Transformation Electromagnetics for Designing Beamformers

4.1 Chapter Introduction

4.1.1 Transformation Electromagnetics: History and Shortcomings

Various exotic electromagnetic devices have been proposed and developed using transformation electromagnetics. Transformation electromagnetics exploits the form invariance of Maxwell's equations under coordinate transformations to design anisotropic, inhomogeneous electromagnetic devices [4]. Examples have included wave collimators, polarization rotators, and cloaks [6, 52–54]. However, these coordinate-transformation techniques often yield material parameters that are difficult to implement, such as highly anisotropic or rapidly-varying materials. Moreover, designs frequently require materials with relative permittivities and permeabilities less than unity, which are inherently dispersive and severely band-limited [54–56].

A variety of techniques have since been proposed to mitigate these problems. For example, in [57] a quasiconformal mapping is used to minimize material anisotropy. Material parameters can also be simplified by restricting device operation to a single illumination [58]. In this case, coordinate-transformation techniques can be avoided altogether [59].

4.1.2 An Alternative to Transformation Electromagnetics

Nevertheless, material parameters resulting from the aforementioned techniques are still often difficult to implement. To improve physical realizability, one can consider avoiding coordinate mapping altogether and instead search a constrained material parameter space

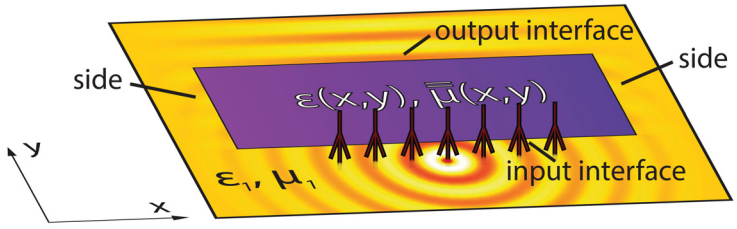

Figure 4.1 A transformation device of material parameter distribution $\epsilon_z(x, y)$ and $\bar{\bar{\mu}}(x, y)$. The device transforms N stipulated input excitation into N prescribed output fields. The transformation region is surrounded by a homogeneous medium of permittivity ϵ_1 and permeability μ_1. The input excitations are $\hat{z}$-directed line currents. In this figure, the center input is excited.

directly. In addition, finding an appropriate coordinate transformation can be difficult or impossible in certain cases, so searching the material space could lead to improved design flexibility.

In this chapter, an optimization procedure is proposed to perform this search of the material parameter space. The procedure is employed to design 2D, inhomogeneous, anisotropic electromagnetic devices that perform a prescribed function under a given set of material parameter constraints. The technique consists of a finite-element method (FEM) forward solver coupled to a constrained minimization algorithm. The minimization algorithm utilizes an analytic gradient to develop a localized approximation of the cost function, which significantly accelerates the optimization. Although the optimization problem is not convex, the proposed technique demonstrates good performance. The tensorial constitutive parameters of the 2D designs can be physically-implemented using printed-circuit board topologies, such as tensor transmission lines [60].

The proposed procedure has two primary advantages over coordinate-transformation methods: (1) it can place constraints on material parameters to improve practicality and bandwidth and (2) it permits the design of devices for which a transformation map may be difficult/impossible to find, such as those with a different prescribed output for each stipulated input. The procedure is applied to the design of two beamformer transformation devices.

4.1.3 Chapter Outline

The chapter is outlined as follows. Section 4.2 briefly describes the formulation of the FEM forward problem. In Section 4.3, the formulation of the minimization algorithm is detailed. Section 4.4 presents the first example design (Design 1). Section 4.5 presents the second design (Design 2).

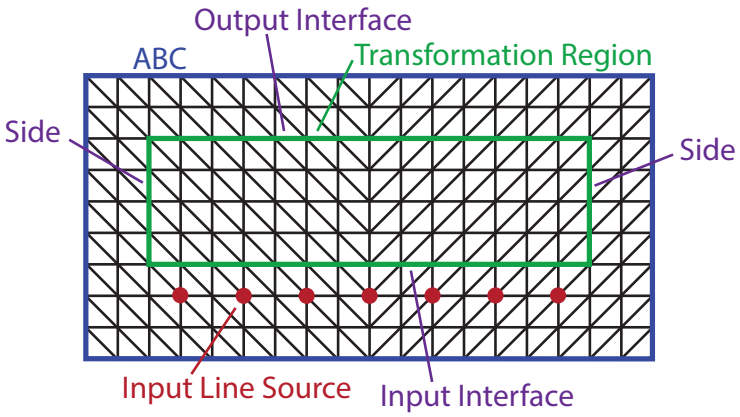

Figure 4.2 Tesselation of the anisotropic, inhomogeneous metamaterial device (transformation region) and its surrounding medium. The domain is enclosed by an absorbing boundary condition (ABC). Here, 7 equally spaced input line-current excitations are depicted.

4.2 FEM Forward Problem

This chapter considers 2D electromagnetic devices consisting of anisotropic, inhomogeneous material parameters that manipulate TE fields ($\vec{E} = E_z\hat{z}$ and $\vec{H} = H_x\hat{x} + H_y\hat{y}$). The relevant material parameters are a scalar permittivity ϵ_z and tensor permeability $\bar{\bar{\mu}}$:

$$\bar{\bar{\mu}} = \begin{bmatrix} \mu_{xx} & \mu_{xy} \\ \mu_{yx} & \mu_{yy} \end{bmatrix}. \tag{4.1}$$

They are assumed to be reciprocal: $\mu_{xy} = \mu_{yx}$.

Fig. 4.1 depicts a 2D electromagnetic device featuring a region of material distribution $\epsilon_z(x, y)$ and $\bar{\bar{\mu}}(x, y)$. This region, referred to as the transformation region, is surrounded by a homogeneous medium of permittivity ϵ_1 and permeability μ_1. These materials can easily be implemented in practice using tensor transmission-line metamaterials [60]. The goal is to find $\epsilon_z(x, y)$ and $\bar{\bar{\mu}}(x, y)$ that transform a specified set of fields incident on the region (input fields) to a prescribed set of transmitted fields (output fields), while obeying material constraints and minimizing power lost out the sides of the region. As in [59], $\hat{z}$-directed line currents laterally displaced on the input side are used as input excitations, since these can be implemented in practice using microstrip input feedlines.

To design the material parameter distribution $\epsilon_z(x, y)$ and $\bar{\bar{\mu}}(x, y)$, a finite-element method (FEM) solver is coupled to a constrained nonlinear optimization algorithm [61]. Here, the FEM solver is implemented by finding the stationary point of the associated Ritz functional [62]

$$\delta \int_{\Omega} \left[(\nabla \times E_z \hat{z}) \bar{\bar{\nu}}_r (x,y) (\nabla \times E_z \hat{z}) - k_0^2 \epsilon_{rz}(x,y) E_z^2 \right] d\Omega$$
$$+ \delta \int_{\Omega} j 2\omega\mu_0 I \delta(\mathbf{r} - \mathbf{r}') d\Omega + \delta \int_{\delta\Omega} \hat{n} \times (\nabla \times u\hat{z}) \cdot E_z \hat{z} d\Gamma = 0, \tag{4.2}$$

where $\bar{\bar{\nu}}_r = \bar{\bar{\mu}}_r^{-1}$, Ω is the domain of interest, and u satisfies the boundary condition along $\delta\Omega$, the contour enclosing Ω. For a detailed derivation of the functional, refer to Appendix A.

With a sufficiently dense tessellation of Ω, the variational problem can be transformed into a matrix problem,

$$\bar{\bar{K}} \mathbf{E_z} = \mathbf{b}, \tag{4.3}$$
$$\mathbf{E_z} = \bar{\bar{K}}^{-1} \mathbf{b}, \tag{4.4}$$

where $\mathbf{E_z}$ is a vector containing the E_z values at the vertices of the mesh, vector $\mathbf{b}$ represents the incident field, and $\bar{\bar{K}}$ is the FEM matrix. Rapid computation of $\mathbf{E_z}$ for multiple excitations $\mathbf{b}$ is performed using LU decomposition. To further expedite the solution process, a permutation matrix $\bar{\bar{P}}$ is computed using the Reverse Cuthill-McKee algorithm to increase the sparsity of the triangular matrices resulting from LU decomposition [63]:

$$\bar{\bar{K}} = \bar{\bar{P}}^T \bar{\bar{K}}' \bar{\bar{P}} = \bar{\bar{P}}^T \bar{\bar{L}}' \bar{\bar{U}}' \bar{\bar{P}}, \tag{4.5}$$

and therefore

$$\bar{\bar{K}}^{-1} = \bar{\bar{P}}^T \bar{\bar{U}}'^{-1} \bar{\bar{L}}'^{-1} \bar{\bar{P}}. \tag{4.6}$$

Substituting (4.6) into (4.4):

$$\mathbf{E_z} = \bar{\bar{P}}^T \bar{\bar{U}}'^{-1} \bar{\bar{L}}'^{-1} \bar{\bar{P}} \mathbf{b}. \tag{4.7}$$

As will be discussed further in Section 4.4, a coarse mesh with linear interpolation functions is used initially to expedite the optimization and subsequently refined. Ultimately, a denser mesh with quadratic interpolation functions is used.

4.3 Optimization

The FEM electromagnetic solver is coupled to a constrained nonlinear optimization algorithm [61] that searches for the necessary material parameters. The employed cost function can be formulated using either the output aperture field (spatial cost function) or the far-field

(spectral cost function). Both options are featured in this chapter (in Sections 4.4 and 4.5, respectively).

Although the optimization problem is not convex in general, the techniques employed here are effective for the design of anisotropic, inhomogeneous electromagnetic devices.

4.3.1 Material Parameters

The electromagnetic device is partitioned into unit cell blocks. Each block is defined by material parameters ϵ_z, ν_{xx}, ν_{xy}, ν_{yy}, where

$$\bar{\bar{\nu}} = \begin{bmatrix} \nu_{xx} & \nu_{xy} \\ \nu_{yx} & \nu_{yy} \end{bmatrix} = \bar{\bar{\mu}}^{-1}. \tag{4.8}$$

Reciprocity ($\nu_{xy} = \nu_{yx}$) is assumed throughout the design process. Note that $\bar{\bar{\nu}}$ is used instead of $\bar{\bar{\mu}}$ to simplify the finite-element code (see (4.2)).

A set of sinusoidal basis functions are used to comprise the material parameter distribution $\epsilon_z(x, y)$ and $\bar{\bar{\nu}}(x, y)$ of the transformation region. This helps reduce the number of independent variables and also ensures that the material parameters are slowly-varying. The basis functions are as follows:

$$\epsilon_z(x,y) = 1 + \sum_{m=0}^{N} \sum_{n=0}^{N-m} a_{mn} \sin\left[(2m-1)\pi u\right] \sin\left[(n-1)\pi p\right], \tag{4.9a}$$

$$\nu_{xx}(x,y) = 1 + \sum_{m=0}^{N} \sum_{n=0}^{N-m} b_{mn} \sin\left[(2m-1)\pi u\right] \sin\left[(n-1)\pi p\right], \tag{4.9b}$$

$$\nu_{yy}(x,y) = 1 + \sum_{m=0}^{N} \sum_{n=0}^{N-m} c_{mn} \sin\left[(2m-1)\pi u\right] \sin\left[(n-1)\pi p\right], \tag{4.9c}$$

$$\nu_{xy}(x,y) = \sum_{m=0}^{N} \sum_{n=0}^{N-m} d_{mn} \sin\left[2m\pi u\right] \sin\left[(n-1)\pi p\right], \tag{4.9d}$$

where

$$u = \frac{x_i - x_{min}}{x_{max} - x_{min}}, \tag{4.10a}$$

$$p = \frac{y_j - y_{min}}{y_{max} - y_{min}}. \tag{4.10b}$$

Here, (x_i, y_j) is the coordinate of the center of the unit cell containing (x, y).

The design of the device reduces to optimizing the material parameter coefficients a_{mn}, b_{mn}, c_{mn}, and d_{mn} of (4.9) to achieve a prescribed output field for each input illumination.

For the remainder of this chapter, these material parameter coefficients will be represented by a single vector $\mathbf{g}$.

4.3.2 Spatial Cost Function

Appendix B provides a detailed derivation of the spatial cost function, which is formulated using an inner product between the achieved output fields and the desired output fields. This cost function will be employed for the design example presented in Section 4.4. The main result is presented here.

For Q different input/output field distribution pairs and material parameter coefficients $\mathbf{g}$, the spatial cost function is given by:

$$s(\mathbf{g}) = \sum_{q=1}^{Q} \left[1 - \frac{|k(h_q(x,\mathbf{g})) \cdot k(h_{q0}(x))^*|^2}{||k(h_{q0}(x))||^4} \right]. \tag{4.11}$$

The subscript q denotes the corresponding input number. The subscript $q0$ denotes the desired output distribution for a specified input number q. The inner product is defined as an integration over the output interface of the transformation region,

$$c(x,\mathbf{g}) \cdot d(x,\mathbf{g}) = \int_{-L/2}^{L/2} c(x,\mathbf{g}) d(x,\mathbf{g}) dx, \tag{4.12}$$

where L is the length of the output interface. The norm $||\dots||$ is defined as

$$||c(x,\mathbf{g})|| = \sqrt{c(x,\mathbf{g}) \cdot c(x,\mathbf{g})^*}. \tag{4.13}$$

The function $h_q(x,\mathbf{g})$ is given by

$$h_q(x,\mathbf{g}) = \sqrt{P_q(x)} \angle E_{qz}(x), \tag{4.14}$$

where $P_q(x)$ is the power density crossing the coordinate x on the output interface (see Fig. 4.1), and $\angle E_{qz}(x)$ is the phase of the electric field at the same location. The function k places an emphasis on the shape of the output fields over the total output power (see Appendix B):

$$k(h_q(x,\mathbf{g})) = h_q(x,\mathbf{g}) \cdot \min\left\{1, \beta \frac{||h_{q0}(x)||}{||h_q(x,\mathbf{g})||}\right\}. \tag{4.15}$$

4.3.3 Spectral Cost Function

For beam-shaping applications, it is often convenient to employ a spectral cost function, due to its direct relation to the far-field pattern [36]. The spectral cost function for the design example presented in Section 4.5 of this chapter is given by

$$s(\mathbf{g}) = \sum_{q=1}^{Q} \int_{-k_0}^{k_0} \left[|\zeta_q(k_x, \mathbf{g})|^2 - |\zeta_{q0}(k_x)|^2 \right] dk_x, \tag{4.16}$$

where $\zeta_q(k_x, \mathbf{g})$ is defined as

$$\zeta_q(k_x, \mathbf{g}) = A_q(k_x) f_q(k_x). \tag{4.17}$$

Here, $f_q(k_x)$ is the Fourier spectrum of the output, which is given by

$$f_q(k_x) = \int_{-\infty}^{\infty} E_{qz}(x) e^{jk_x x} dx, \tag{4.18}$$

and $A_q(k_x)$ is a weighting function. For Design 2 (see Sec. 4.5), the function $A_q(k_x)$ is equal to 1 in the beam-shaping region and 0.2 elsewhere. The prescribed far-field $\zeta_{q0}(k_x)$ is equal to 0 outside of the beam-shaping region.

4.3.4 Optimization Algorithm

To arrive at practical and realizable beamformer designs, the following constrained optimization is employed:

$$\begin{aligned} \underset{\mathbf{g}}{\text{minimize}} \quad & s(\mathbf{g}) \\ \text{subject to} \quad & 1 < \epsilon_z(x,y) < \epsilon_z^u \\ & \nu^l < \nu_1(x,y) < 1 \\ & \nu^l < \nu_2(x,y) < 1 \\ & \max\left\{ \frac{\nu_1(x,y)}{\nu_2(x,y)}, \frac{\nu_2(x,y)}{\nu_1(x,y)} \right\} < \xi, \end{aligned} \tag{4.19}$$

where $\nu_1(x,y)$ and $\nu_2(x,y)$ represent the eigenvalues of the $\bar{\bar{\nu}}(x,y)$ tensor and $s(\mathbf{g})$ is the cost function. In this way, permittivity and permeability values less than unity are avoided, material parameter ranges are bounded, and anisotropy is limited.

To minimize the cost function $s(\mathbf{g})$ under the constraints imposed on material parameters, the active-set algorithm [64] is employed and implemented using MATLAB. The algorithm is accelerated by analytically computing the gradient of the cost function and the constraint

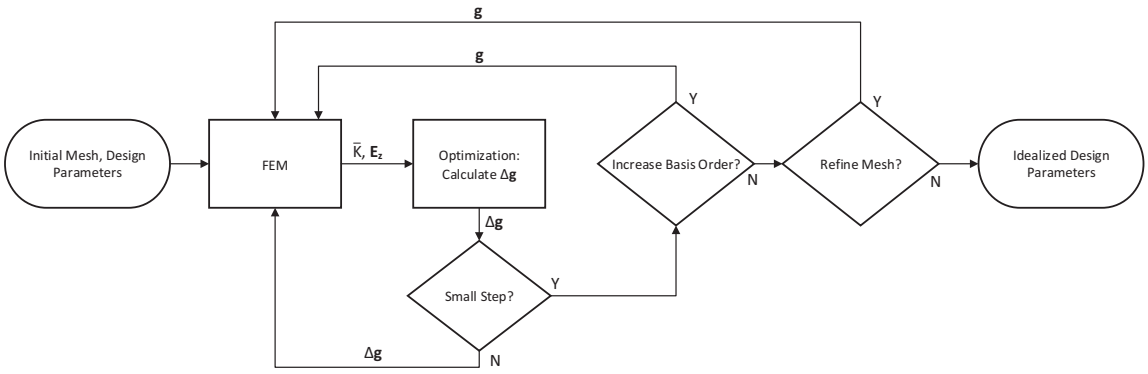

Figure 4.3 Graphical depiction of the algorithm for designing anisotropic, inhomogeneous metamaterial devices. The mesh and design parameters are initialized and fed to the start of the inner design loop, which consists of an FEM electromagnetic solver (forward problem) and a minimization algorithm. The outer design loop controls increments to the order of the material parameter basis functions and the necessary mesh refinements.

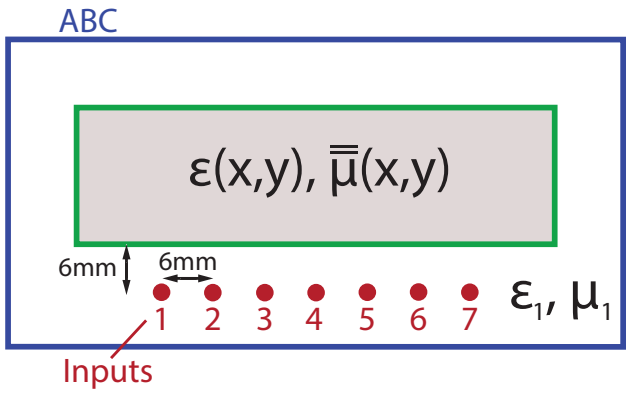

Figure 4.4 Position of the input excitations ($\hat{z}$-directed line currents) for antenna beamformer Design 1.

functions. The gradient is derived by first noting that the matrix $\bar{\bar{K}}$ is of the form [62]

$$\bar{\bar{K}} = \bar{\bar{K}}_0 + \sum_{p=1}^{P} g_p \bar{\bar{A}}_p, \tag{4.20}$$

where g_p is the p^{th} material parameter coefficient of $\mathbf{g}$. The matrices $\bar{\bar{A}}_p$ and $\bar{\bar{K}}_0$ are fixed. From (4.4), it follows that the partial derivative $\partial \mathbf{E_z}/\partial g_p$ is given by:

$$\frac{\partial \mathbf{E_z}}{\partial g_p} = \frac{\partial}{\partial g_p}\left(\bar{\bar{K}}^{-1}\mathbf{b}\right) = \frac{\partial \bar{\bar{K}}^{-1}}{\partial g_p}\mathbf{b}. \tag{4.21}$$

An expression for $\partial K^{-1}/\partial g_p$ is found as follows:

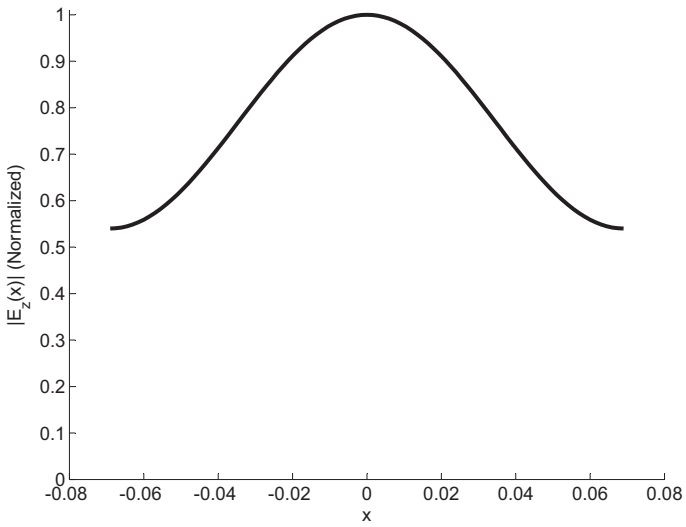

Figure 4.5 The magnitude output magnitude profile $|E_z(x)|$ for each input of beamformer Design 1. The magnitude is tapered to reduce sidelobe levels.

$$\frac{\partial}{\partial g_p}\left(\bar{\bar{K}}^{-1}\bar{\bar{K}}\right) = \frac{\partial}{\partial g_p}\left(\bar{\bar{I}}\right),$$
$$\frac{\partial \bar{\bar{K}}^{-1}}{\partial g_p}\bar{\bar{K}} + \bar{\bar{K}}^{-1}\frac{\partial \bar{\bar{K}}}{\partial g_p} = 0. \tag{4.22}$$

According to (4.20), ${}^{\partial \bar{\bar{K}}}/_{\partial g_p} = \bar{\bar{A}}_p$, and therefore:

$$\frac{\partial K^{-1}}{\partial g_p} = -K^{-1}\bar{\bar{A}}_p K^{-1}. \tag{4.23}$$

Eq. (4.21) can now be rewritten as:

$$\frac{\partial \mathbf{E_z}}{\partial g_p} = \frac{\partial \bar{\bar{K}}^{-1}}{\partial g_p}\mathbf{b} = -K^{-1}\bar{\bar{A}}_p K^{-1}\mathbf{b}. \tag{4.24}$$

Substituting (4.4) and (4.6) into (4.24) yields,

$$\frac{\partial \mathbf{E_z}}{\partial g_p} = -\bar{\bar{P}}^T\bar{\bar{U}}'^{-1}\bar{\bar{L}}'^{-1}\bar{\bar{P}}\bar{\bar{A}}_p\mathbf{E_z}. \tag{4.25}$$

Expression (4.25) yields an analytic expression for the gradient of cost function $s(\mathbf{g})$.

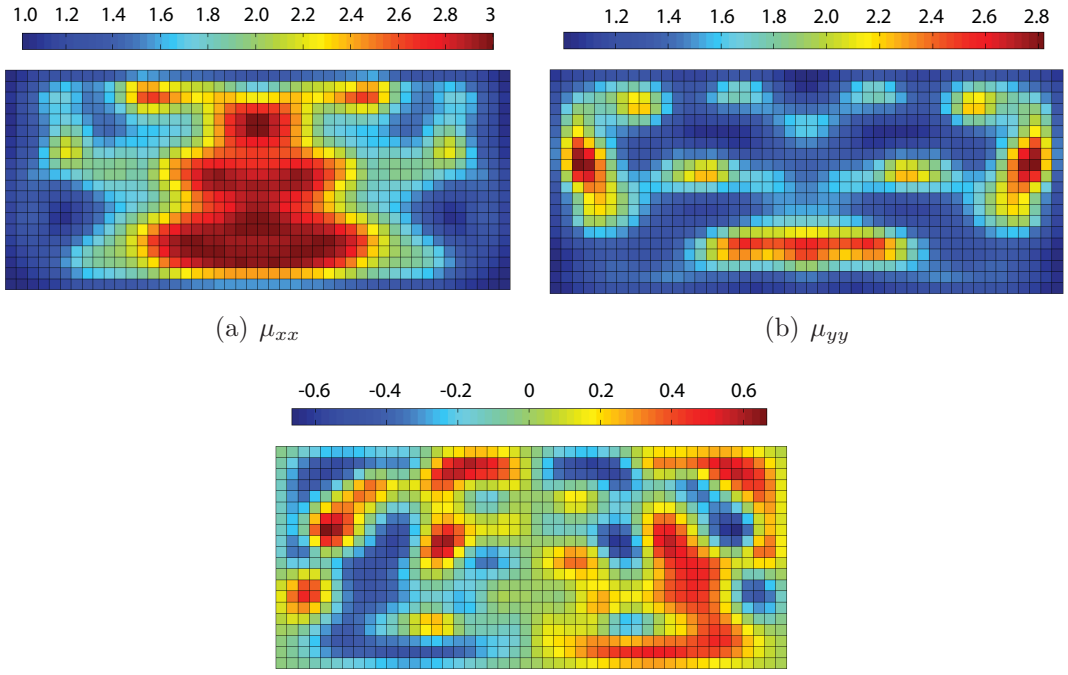

(a) μ_{xx} (b) μ_{yy}

(c) μ_{xy}

Figure 4.6 Material parameters for antenna beamformer Design 1. The permittivity is $\epsilon_z = 1$ for all cells. Due to the symmetry of the prescribed radiation patterns, even symmetry across the y-axis is enforced on the permeability entries μ_{xx} and μ_{yy} and odd symmetry is enforced on μ_{xy}.

4.3.5 Design Flow

A flowchart of the design process is shown in Fig. 4.3. Initially, the order N of the material parameter basis functions is set to $N = 1$ to expedite the algorithm. In addition, a coarse mesh with simple, linear interpolation functions is employed. The material coefficients $\mathbf{g}$ are initialized to 0. After minimizing the cost function, N is incremented to include higher-order basis functions. The coefficients corresponding to any new basis functions are initialized to 0. The algorithm continues incrementing N until a desired limit N_{max} is achieved. For the designs presented in Sec. 4.4 and Sec. 4.5, $N_{max} = 8$ and $N_{max} = 9$, respectively. Subsequently, the mesh is refined and quadratic interpolation functions are used to find a more accurate solution.

4.4 Beamformer Design 1

In this section, the first design example (referred to as Design 1) is presented. The desired function of Design 1 is to transform 7 specified input excitations to 7 prescribed output beams, while minimizing power lost out the sides of the transformation region. As in [59],

$\hat{z}$-directed line currents laterally displaced along the input face are used as input excitations, since these can be implemented in practice using microstrip input feedlines. The 7 output beams are prescribed to radiate at the following azimuthal angles: $\mathbf{\Phi}$ = (-30°, -20°, -10°, 0°, 10°, 20°, 30°). The optimization is performed at 10 GHz, but due to the true-time-delay nature of the beamformer (similar to the Rotman lens [65, 66]), the radiated beams are essentially frequency invariant.

4.4.1 Initial Design Parameters

At the start of the design process, the following parameters are defined:

- Specified input field excitations: $\mathbf{b}_q$
- Desired output field profiles: $h_{q0}(x)$
- Cell size: d
- Beamformer dimensions
- Frequency: f
- Material parameters (ϵ_1, μ_1) of surrounding isotropic, homogeneous medium (see Fig. 4.4)
- Material constraints

The subscript q refers to the particular input/output pair. For the antenna beamformer design presented here, $f = 10$ GHz, $d = 3$mm, $\nu^l = 1/3$, $\xi = 2$, $\epsilon_1 = \epsilon_0$, and $\mu_1 = 2.957\mu_0$. Recall that ν^l is the lower limit enforced on the eigenvalues of $\bar{\bar{\nu}}$ and ξ is the upper limit on the anisotropy of each unit cell (see Subsection 4.3.4).

The transformation region is comprised of 46 cells ($4.6\lambda_0$) along x and 20 cells ($2\lambda_0$) along y. In addition, it is assumed that the 7 line-current input excitations are placed 6mm away from the input interface, spaced 6mm apart (see Fig. 4.4).

4.4.2 Stipulated Inputs and Desired Outputs

The prescribed magnitude distribution of the electric field $|E_z(x)|$ at the output interface of the beamformer is the same for each of the 7 inputs. Only the output phase distribution (beam pointing direction) is varied for each input. As a result, the beams broaden with increasing radiation angle (away from broadside). The output magnitude profile $|E_z(x)|$ is tapered to reduce the sidelobes of the radiation pattern. The normalized profile is chosen to be

$$|E_z(x)| = \frac{1}{2}\left[1 + \alpha + (\alpha - 1)\cos\left(\frac{2\pi(x - L/2)}{L}\right)\right], \tag{4.26}$$

where L is the length of the antenna beamformer, $\alpha = 0.54$, and x is the position along the output interface of the transformation region. The field magnitude profile (4.26) is plotted in Fig. 4.5. This particular profile corresponds to the average of a Hamming window and a uniform window. Alternative magnitude profiles could also be chosen to reduce sidelobes.

Recall that the desired azimuthal beam pointing directions are chosen to be $\mathbf{\Phi}$ = (-30°, -20°, -10°, 0°, 10°, 20°, 30°), with respect to broadside, for the equi-spaced line-current input excitations. In a practical, tensor transmission-line implementation, a flare antenna would be placed at the output interface to transform the guided wave at the output interface to a radiated wave [60]. Refraction of the output wave would occur, due to the refractive index difference between the medium (ϵ_1, μ_1) surrounding the transformation region and free space, in accordance with Snell's law [67]. The exit angle θ_q from the output interface of the transformation region for a desired angle of radiation ϕ_q is given by:

$$\theta_q = \sin^{-1}\left[\sqrt{\frac{\epsilon_0\mu_0}{\epsilon_1\mu_1}}\sin\phi_q\right], \tag{4.27}$$

where subscript q denotes the prescribed output number. So, to achieve the prescribed radiation angle, the output phase is stipulated as

$$\angle E_{zq}(x) = -k_1 x \sin\theta_q, \tag{4.28}$$

where k_1 is the index of the medium surrounding the transformation region.

4.4.3 Optimization Results

The optimization for Design 1 was performed using the spatial cost function defined by (4.11), which was found to work best. The material parameters for the design are provided in Fig. 4.6. For simplicity, the permittivity was fixed to $\epsilon_z(x, y) = 1$ for each cell. Due to the symmetry of the prescribed radiation patterns, even symmetry is enforced for μ_{xx} and μ_{yy}, while odd symmetry is enforced for μ_{xy}.

The beamformer design was verified using the commercial electromagnetic solver COMSOL Multiphysics. A spatial plot of electric field (E_z) for the broadside input (input 4) at $f = 10$ GHz is provided in Fig. 4.7. The output phase profiles at $f = 10$ GHz are provided in Fig. 4.8, which shows negligible phase error. The output magnitude profiles at $f = 10$ GHz are provided in Fig. 4.9. Far-field plots of the output beams are shown in Fig. 4.10 for 8-12 GHz. The results show excellent agreement with the prescribed performance of the beamformer.

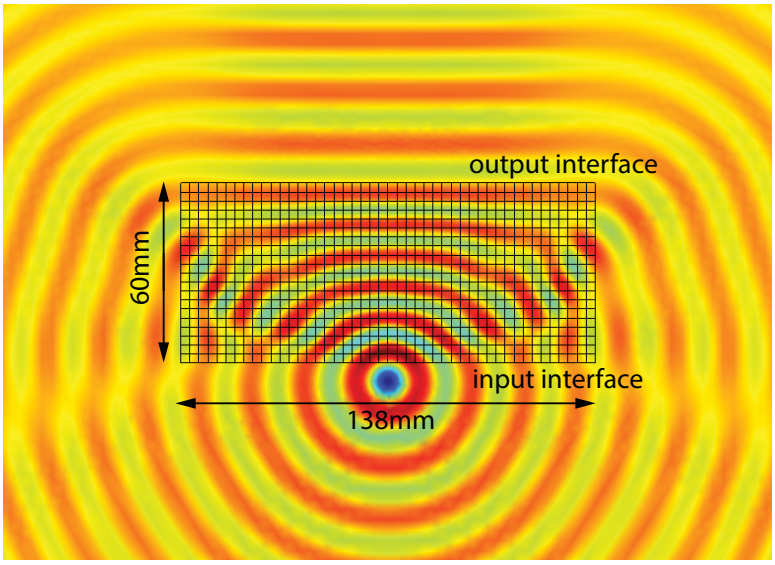

Figure 4.7 Spatial plot of E_z for beamformer Design 1 at $f = 10$GHz, computed using the commercial electromagnetic solver COMSOL Multiphysics.

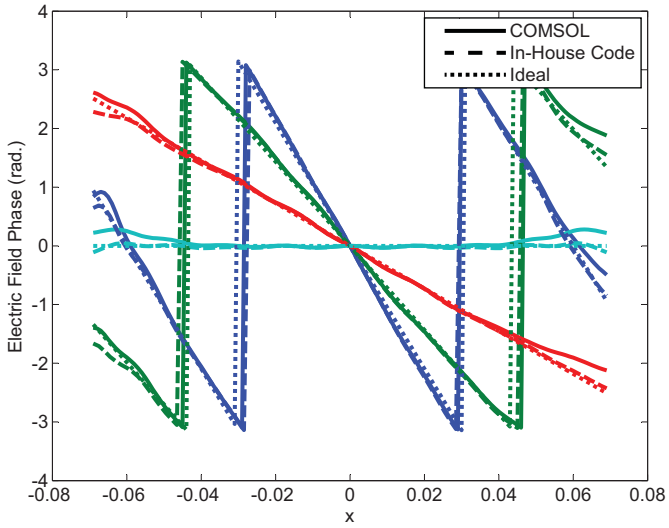

Figure 4.8 Relative phase of the electric field at the output interface of the beamformer for each input excitation of Design 1. The phase profiles corresponding to the three remaining inputs are not shown due to the symmetry of the beamformer. The plots show very good agreement between COMSOL, the in-house FEM code, and the prescribed phase.

4.5 Beamformer Design 2

In this section, a second design example (referred to as Design 2) is presented to highlight the beam-shaping capabilities of the optimization approach. In this example, 3 input/output pairs are designed. Each input produces a flattop radiation pattern with 40° beamwidth covering the following angular ranges:

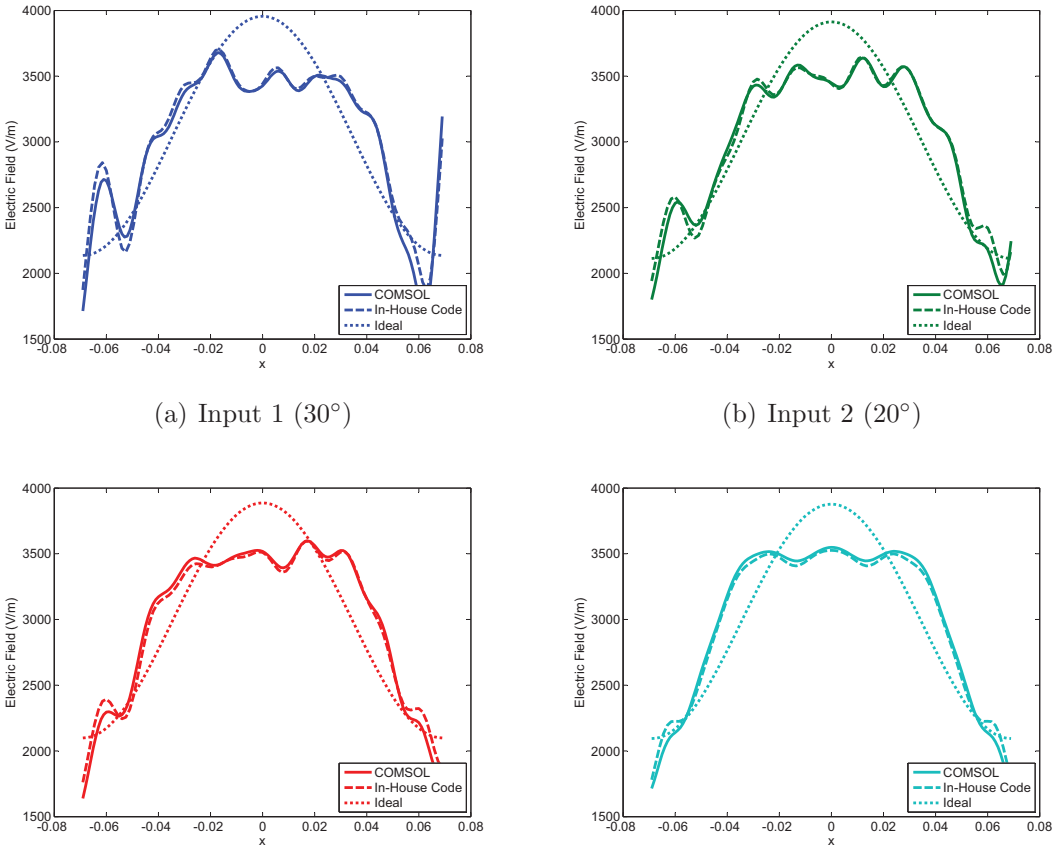

(a) Input 1 (30°)

(b) Input 2 (20°)

(c) Input 3 (10°)

(d) Input 4 (0°)

Figure 4.9 Magnitude profile of the output electric field for Design 1. The last three inputs are omitted due to symmetry. The plots show very good agreement between COMSOL Multiphysics and the in-house FEM code. Although the ideal magnitude profile is not achieved exactly, the far-field results match the prescribed radiation angles with reduced sidelobe levels. Excitation currents of 1 Ampere are used for each input.

1. $\theta \in (-60°, -20°)$
2. $\theta \in (-20°, 20°)$
3. $\theta \in (20°, 60°)$

4.5.1 Design Parameters

The parameters of the beamformer are as follows: $f = 10$ GHz, $d = 3$mm, $\nu^l = 1/4$, $\xi = 2$, $\epsilon_1 = \epsilon_0$, and $\mu_1 = 2.957\mu_0$. The transformation region is comprised of 56 cells ($5.6\lambda_0$) along x and 23 cells ($2.3\lambda_0$) along y. The input excitations are assumed to be 3 $\hat{z}$-directed line currents placed 6mm away from the input interface and spaced 30mm apart.

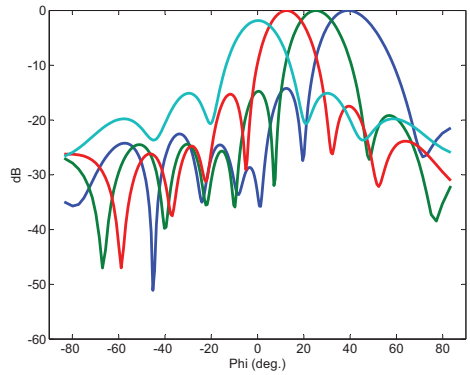

(a) 8 GHz

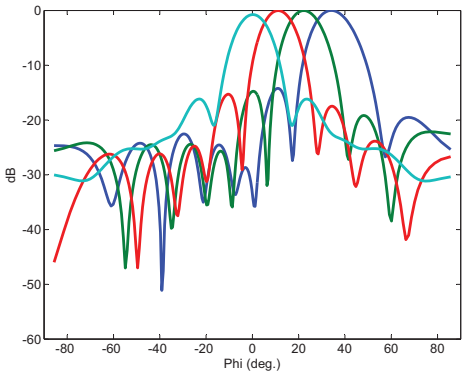

(b) 9 GHz

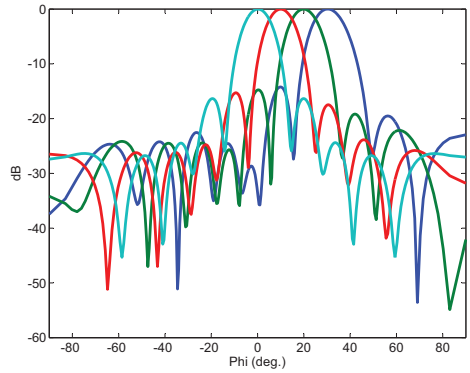

(c) 10 GHz

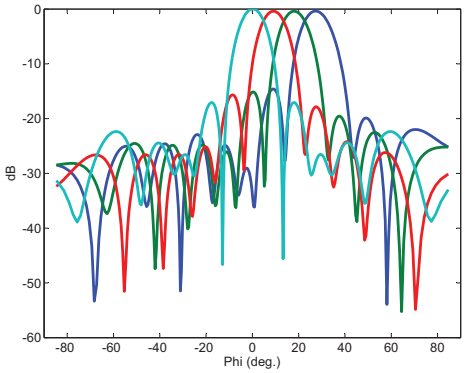

(d) 11 GHz

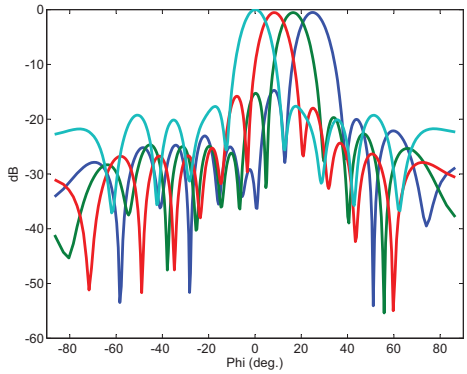

(e) 12 GHz

Figure 4.10 Azimuthal far-field plots of the output beams for beamformer Design 1, computed using COMSOL Multiphysics ($\sin\phi = k_x/\omega\sqrt{\epsilon_0\mu_0}$). Each plot is normalized to the input with highest spectral magnitude at the same frequency. Due to the symmetry of the beamformer, the output beams for negative angles are not shown.

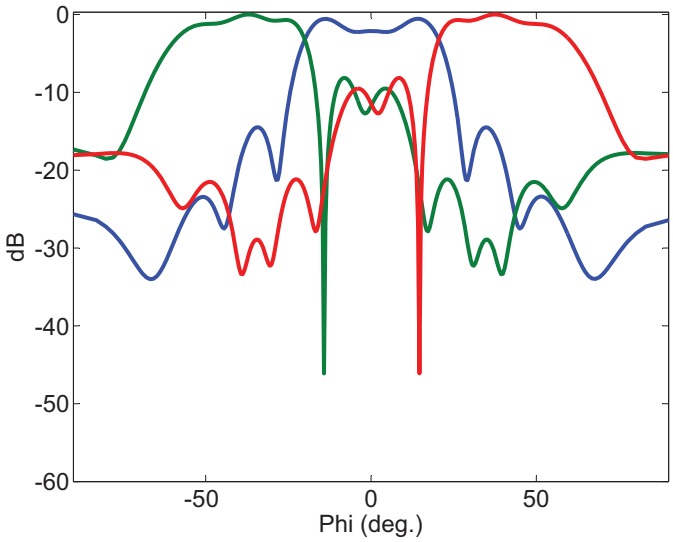

Figure 4.11 Azimuthal far-field plot of the output beams for beamformer Design 2, computed using COMSOL Multiphysics ($\sin\phi = {}^{k_x}/_{\omega\sqrt{\epsilon_0\mu_0}}$).

4.5.2 Optimization Results

Using the spectral cost function defined by (4.16), the optimization is performed for Design 2. The design was simulated using COMSOL Multiphysics. A far-field plot of the output beams is shown in Fig. 4.11. Once again, the results show excellent agreement with the prescribed goals of the beamformer.

4.6 Chapter Summary

In this chapter, an alternative to transformation electromagnetics is reported for designing 2D, inhomogeneous, anisotropic electromagnetic devices. The technique couples a custom FEM forward solver to a constrained, nonlinear minimization algorithm. The technique has two primary advantages over transformation electromagnetics: 1) it constrains material parameters to improve practicality and bandwidth and 2) it permits the design of devices for which a transformation map may be difficult to impossible to find, such as electromagnetic devices with multiple inputs and multiple outputs. The technique is accelerated by an analytic expression for the gradient of the cost function. Simulation results show close agreement with the prescribed behavior of the designed beamformers.

In the next chapter, measurement results for the fabricted, printed-circuit, 7-port beamformer are presented.

Chapter 5
Printed Beamformer Design

5.1 Chapter Introduction

5.1.1 Review of Chapter 4

The advent of metamaterials has opened up a world of possibilities, particularly with the introduction of coordinate-transformation design techniques [4,5]. These techniques, referred to as transformation electromagnetics, exploit the form-invariance of Maxwell's equations under coordinate transformations to find anisotropic, inhomogeneous material parameters that achieve a prescribed function. Examples have included wave collimators, polarization rotators, and cloaks [6, 52–54].

However, metamaterials and transformation electromagnetics are not without their faults. It is well-known that metamaterials with $\epsilon < \epsilon_0$ or $\mu < \mu_0$ are inherently dispersive [7]. This limits the performance of not only negative-refractive index lenses [2] but also the electromagnetic devices designed using transformation electromagnetics, which often exhibit such material parameters. Transformation electromagnetics may also yield parameters that are difficult to implement, such as highly-anisotropic materials. In addition, for certain designs, it may be difficult or impossible to find an appropriate coordinate mapping to utilize the technique.

Unlocking the full potential of metamaterials requires improvements to these existing design techniques. In Ch. 4, an alternative to transformation electromagnetics was introduced that couples a custom finite-element method (FEM) solver to a constrained, nonlinear minimization algorithm. This new technique has two primary advantages over transformation electromagnetics: (1) it can place constraints on material parameters to improve practicality and bandwidth and (2) it permits the design of devices for which a transformation map may be difficult or impossible to find, such as those with several specified inputs and outputs. In this new technique, the electromagnetic devices are first modeled as a 2D medium featuring a transformation region of unknown inhomogeneous, anisotropic material parameters: scalar

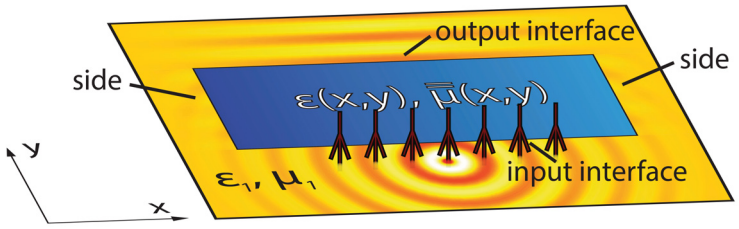

Figure 5.1 The proposed beamformer is first modeled as a 2D medium featuring a transformation region of unknown inhomogeneous, anisotropic material parameters: permittivity $\epsilon_z(x, y)$ and tensor permeability $\bar{\bar{\mu}}(x, y)$. A homogeneous medium of permittivity ϵ_1 and permeability μ_1 surrounds the transformation region. Optimization is then employed to design $\epsilon_z(x, y)$ and $\bar{\bar{\mu}}(x, y)$.

$\epsilon_z(x, y)$ and tensor permeability $\bar{\bar{\mu}}(x, y)$. Optimization is then employed to design $\epsilon_z(x, y)$ and $\bar{\bar{\mu}}(x, y)$, which can be physically-realized using tensor transmission-line metamaterials.

5.1.2 Printed-Circuit Implementation

In this chapter, a beamformer example is designed and fabricated, which was not done in Ch. 4. The beamformer contains 7 input ports that are designed to switch in 10° increments from -30° to 30°. The beamformer is designed at 10 GHz, but due to the low-pass nature of the tensor transmission-line metamaterials and the beamformer's true-time-delay nature (similar to the Rotman lens [65, 66]), the radiated beams are essentially frequency-invariant.

The proposed beamformer offers several advantages over traditional beamformers, such as the Butler matrix [68], Blass matrix [69], Rotman lens [65], and Luneburg lens [70]. In particular, the design approach has allowed for the stipulation of arbitrary output fields. Moreover, it permits flat input and output interfaces, which can be advantageous for system integration.

5.1.3 Chapter Outline

In Sec. 5.2, the design procedure introduced in Ch. 4 is reviewed briefly. In Sec. 5.3, the design of the printed-circuit beamformer using tensor transmission-line metamaterials is detailed. Simulation results are also provided in Sec. 5.3. Measurement results are presented in Sec. 5.4. Excellent agreement is demonstrated between the measured results and the prescribed design goals.

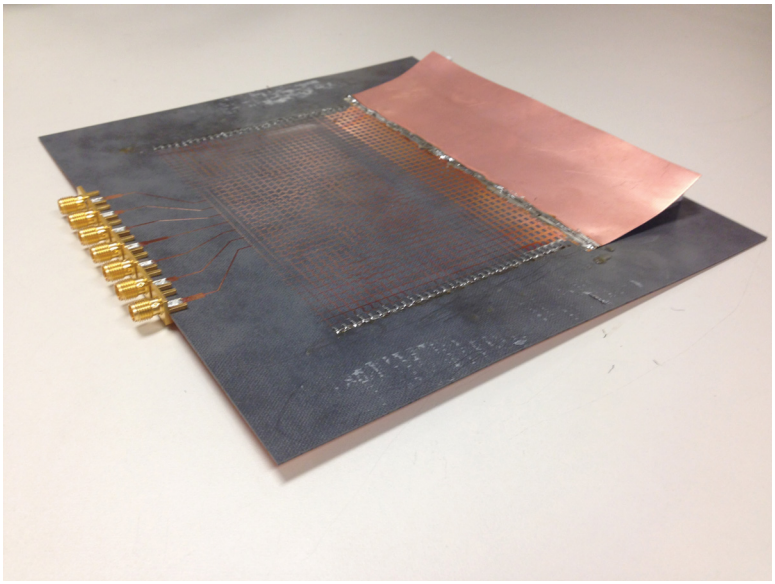

(a)

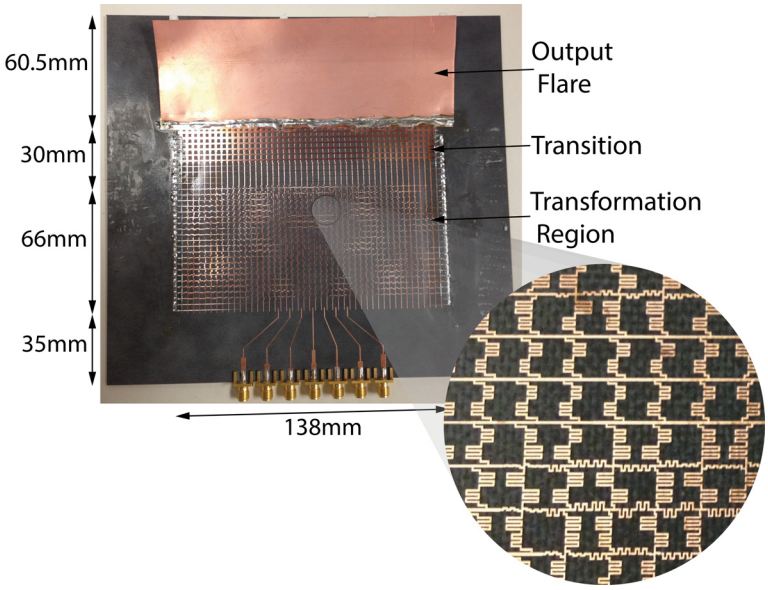

(b)

Figure 5.2 Fabricated printed-circuit beamformer. The beamformer is terminated by an output flare. Surface-mount resistors are soldered to the sides of the beamformer.

5.2 Review: Optimization Design Procedure

In Ch. 4, a new technique was proposed to address the shortcomings of transformation electromagnetics in designing 2D inhomogeneous, anisotropic electromagnetic devices. The technique couples a custom finite-element method (FEM) full-wave solver to a constrained, nonlinear minimization algorithm. In particular, the electromagnetic devices are first modeled as a 2D medium (see Fig. 5.1) featuring a transformation region of unknown inhomogeneous,

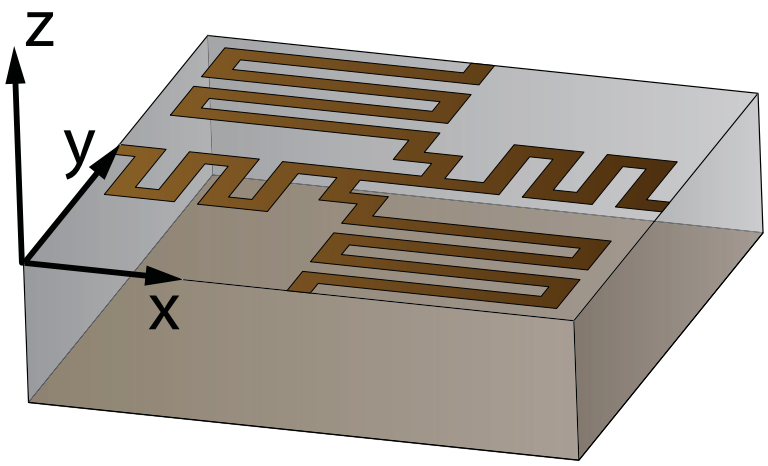

Figure 5.3 Example of a tensor transmission-line unit cell used in the beamformer design.

anisotropic material parameters: scalar permittivity $\epsilon_z(x,y)$ and tensor permeability $\bar{\bar{\mu}}(x,y)$. A homogeneous medium of permittivity ϵ_1 and permeability μ_1 surrounds the transformation region. Optimization is then employed to design $\epsilon_z(x,y)$ and $\bar{\bar{\mu}}(x,y)$, which can be physically-realized using tensor transmission-line metamaterials [60].

The 2D medium is partitioned into unit cell blocks. Each block is defined by material parameters ϵ_z, ν_{xx}, ν_{xy}, ν_{yy}, where

$$\bar{\bar{\nu}} = \begin{bmatrix} \nu_{xx} & \nu_{xy} \\ \nu_{yx} & \nu_{yy} \end{bmatrix} = \bar{\bar{\mu}}^{-1}. \tag{5.1}$$

Reciprocity ($\nu_{xy} = \nu_{yx}$) is assumed throughout the design process. Note that $\bar{\bar{\nu}}$ is used instead of $\bar{\bar{\mu}}$ to simplify the finite-element code (see Ch. 4).

A set of sinusoidal basis functions are used to comprise the material parameter distribution $\epsilon_z(x,y)$ and $\bar{\bar{\nu}}(x,y)$ of the transformation region. This helps reduce the number of independent variables in the optimization and also ensures slowly-varying material parameters. The basis functions are as follows:

$$\epsilon_z(x,y) = 1 + \sum_{m=0}^{N} \sum_{n=0}^{N-m} a_{mn} \sin\left[(2m-1)\pi u\right] \sin\left[(n-1)\pi p\right], \tag{5.2a}$$

$$\nu_{xx}(x,y) = 1 + \sum_{m=0}^{N} \sum_{n=0}^{N-m} b_{mn} \sin\left[(2m-1)\pi u\right] \sin\left[(n-1)\pi p\right], \tag{5.2b}$$

$$\nu_{yy}(x,y) = 1 + \sum_{m=0}^{N} \sum_{n=0}^{N-m} c_{mn} \sin\left[(2m-1)\pi u\right] \sin\left[(n-1)\pi p\right], \tag{5.2c}$$

$$\nu_{xy}(x,y) = \sum_{m=0}^{N} \sum_{n=0}^{N-m} d_{mn} \sin\left[2m\pi u\right] \sin\left[(n-1)\pi p\right], \tag{5.2d}$$

where

$$u = \frac{x_i - x_{min}}{x_{max} - x_{min}}, \tag{5.3a}$$

$$p = \frac{y_j - y_{min}}{y_{max} - y_{min}}. \tag{5.3b}$$

Here, (x_i, y_j) is the coordinate of the center of the unit cell containing (x, y).

The device design reduces to optimizing the coefficients a_{mn}, b_{mn}, c_{mn}, and d_{mn} of (4.9) so that the achieved output field matches the prescribed output field for each input illumination. The optimization problem can be written as follows:

$$\begin{aligned} \underset{\mathbf{g}}{\text{minimize}} \quad & s(\mathbf{g}) \\ \text{subject to} \quad & 1 < \epsilon_z(x,y) < \epsilon_z^u \\ & \nu^l < \nu_1(x,y) < 1 \\ & \nu^l < \nu_2(x,y) < 1 \\ & \max\left\{ \frac{\nu_1(x,y)}{\nu_2(x,y)}, \frac{\nu_2(x,y)}{\nu_1(x,y)} \right\} < \xi \end{aligned} \tag{5.4}$$

where ν_1 and ν_2 represent the eigenvalues of the $\bar{\bar{\nu}}$ tensor, $\mathbf{g}$ is the vector of the material coefficients, and $s(\mathbf{g})$ is the cost function, which is roughly the error in the achieved output field. Constraints are imposed to avoid permittivities and permeabilities less than unity, limit anisotropy, and bound the range of material parameters. At each iteration of the optimization, the achieved output field is calculated using an in-house FEM code. The optimization package in MATLAB then updates the material coefficients to reduce the output error under the imposed material constraints. This update is accelerated by computing the analytic gradient of the cost function (see Ch. 4).

5.3 Design and Fabrication

In Ch. 4, the material parameters $\epsilon_z(x,y)$ and $\bar{\bar{\mu}}(x,y)$ were designed for a 7-port beamformer designed to radiate at the following azimuthal angles: $\mathbf{\Phi}$ = (-30°, -20°, -10°, 0°, 10°, 20°, 30°). This section details the design of the beamformer's printed-circuit implementation, which is shown in Fig. 5.2. The beamformer is designed at 10 GHz, but due to the low-pass nature of the tensor transmission-line metamaterials and the beamformer's true-time-delay nature (similar to the Rotman lens [65, 66]), the radiated beams are essentially frequency-invariant.

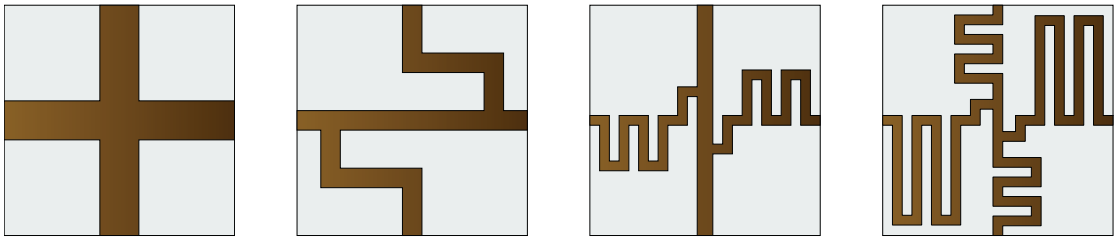

(a) Isotropic, metallic grid

(b) Topology with offset junctions to rotate the principal axes.

(c) Topology with inductive meandering for increased index in one direction.

(d) Topology with inductive meandering in both directions.

Figure 5.4 A variety of tensor transmission-line topologies.

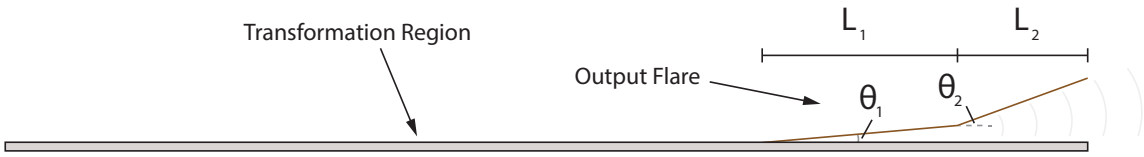

Figure 5.5 Profile view of the printed-circuit beamformer and its output flare.

5.3.1 Tensor Transmission Lines

Each cell of the 2D, inhomogeneous, anisotropic medium can be physically-implemented using tensor transmission-line metamaterials [60, 71]. An example of a printed tensor transmission-line unit cell is provided in Fig. 5.3. These transmission-line metamaterials can possess diagonal and off-diagonal terms in the effective permeability tensor $\bar{\bar{\mu}}$, while still maintaining a rectangular unit cell, rather than a skewed cell. Using the commercial full-wave solver Ansys HFSS, the effective material parameters (ϵ_z, $\bar{\bar{\mu}}$) of a given unit cell can be extracted [71]. This process is referred to as homogenization.

The homogenization procedure employed here is similar to that reported in [71], but with a slight modification. Instead of extracting both ϵ_z and $\bar{\bar{\mu}}$ from the unit cell eigenmode simulation, only the product, $\epsilon_z\bar{\bar{\mu}}$ (the tensor index), is extracted. That is, only the isofrequency dispersion ellipse is characterized for a given unit cell. This modification was made because it is difficult to independently control ϵ_z and $\bar{\bar{\mu}}$ in the unit cell shown in Fig. 5.3, since it does not feature any shunt loading elements. This modified approach works well when the material parameters of the beamformer are smoothly varying, in which case the impedance matching between unit cells of the beamformer can be neglected.

The tensor $\epsilon_z\bar{\bar{\mu}}$ for a given unit cell (e.g. the cell in Fig. 5.3) is extracted from eigenmode simulations performed using the commercial full-wave solver Ansys HFSS. Specifically, the homogenization procedure is as follows:

1. Eigenmode simulations are performed for 8 different propagation angles $\psi = \tan^{-1} k_y/k_x$ at 45° increments. Periodic boundary conditions are applied in the $\hat{x}$ and $\hat{y}$ directions.
2. The output of each HFSS eigenmode simulation is frequency. However, since the unit cell topology is non-dispersive around the intended operation frequencies, frequency scaling is employed to extract sample points of the isofrequency dispersion ellipse.
3. The tensor $\epsilon_z\bar{\bar{\mu}}$ is calculated by fitting the simulated sample points to an ellipse using the algorithms discussed in [72].

5.3.2 Constructing a Cell Database

To design the printed-circuit beamformer, a database of tensor transmission-line unit cells was developed. The database records the effective index tensor $\epsilon_z\bar{\bar{\mu}}$ for a large variety of tensor transmission-line unit cell geometries. In total, the database contains 1164 cells. The geometric variables include the size of the meandered inductance, the offset of the junctions, and the width of the lines (see Fig. 5.4). For fabrication purposes, line widths and line spacings of 5 mil or greater were maintained.

The cells were designed on the dielectric substrate Rogers RT/Duroid 5880, which is characterized by the following properties:

- $\epsilon_r = 2.2$
- dielectric thickness = 0.7874mm (31 mil)
- copper thickness = 70μm (2 oz)
- $\tan\delta = 0.0009$

The range of material parameters available in the cell database are used to determine the material parameter constraints in (5.4).

5.3.3 Design Generation

The printed-circuit beamformer is designed using an inhomogeneous distribution of units cells taken from the database. Specifically, each unit cell in the transformation region and the surrounding medium is generated as follows:

1. The database is searched for the unit cell that best matches the desired $\epsilon_z\bar{\bar{\mu}}$.
2. Interpolation of the database is employed to obtain an even more accurate unit cell implementation.

Table 5.1 Simulated Gain (dB)

f	1	2	3	4	5	6	7
10.0 GHz	4.2	6.2	6.5	6.8	6.5	6.2	4.2
11.0 GHz	7.2	8.8	8.9	8.9	8.9	8.8	7.2
12.0 GHz	7.3	7.0	6.9	7.5	6.9	7.0	7.3
13.0 GHz	7.8	8.7	8.6	8.4	8.6	8.7	7.8

Table 5.2 Simulated Radiation Efficiency

f	1	2	3	4	5	6	7
10.0 GHz	30%	37%	35%	34%	35%	37%	30%
11.0 GHz	33%	42%	40%	37%	40%	42%	33%
12.0 GHz	36%	40%	38%	37%	38%	40%	36%
13.0 GHz	33%	32%	33%	30%	33%	32%	33%

3. The complete printed-circuit design is drawn in HFSS using a Visual Basic script.

To transition the guided waves of the beamformer to radiated, output waves, a flare antenna is attached to the beamformer output. The flare geometry was designed through parametric analysis. With reference to Fig. 5.5, the dimensions of the output flare are $L_1 = 30$mm, $L_2 = 20$mm, $\theta_1 = 5°$, and $\theta_2 = 20°$. The transition between the transformation region and the flare consists of an isotropic mesh grid with a trace width increasing in the $\hat{y}$ direction, as shown in Fig. 5.2.

In addition, surface-mount resistors were soldered to the two sides of the beamformer to mitigate reflections. A value of 200Ω is employed, since it closely matches the Bloch impedance (at normal incidence) of the unit cells directly surrounding the transformation region.

5.3.4 Phase Error Correction

After simulating the complete printed-circuit beamformer, one may find that there is some small error in the output aperture field. This is simply because there is still some inherent error in designing the beamformer with printed circuits. Using a procedure similar to the radiation pattern correction methods employed in Ch. 2, the phase error can be reduced. The procedure is as follows:

1. Design the transformation region for prescribed output fields $h_{0q}(x, \mathbf{g})$ and stipulated input fields (see Ch. 4). Here, the subscript q denotes the input/output number.
2. Design the printed-circuit beamformer using the cell database. Simulate the complete beamformer using a commercial full-wave solver, e.g. Ansys HFSS.

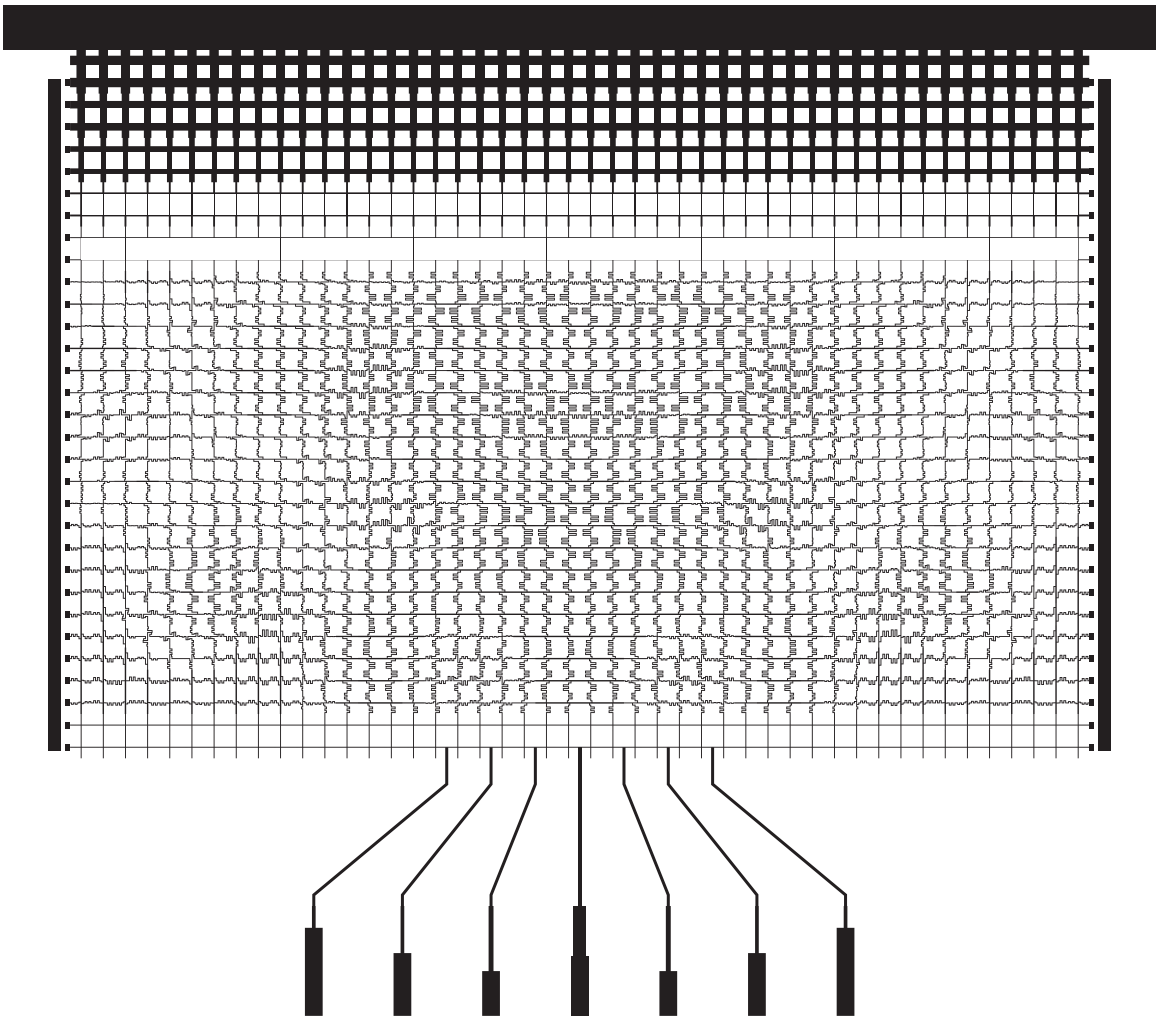

Figure 5.6 Photomask for fabricating the beamformer. A flare antenna is soldered at the beamformer output and plated vias are inserted along the sides to connect to ground. Surface mount resistors are soldered at the 31 (62 total) locations along the sides of the beamformer.

3. Calculate the error $e_{sim}(x) = \angle h_{0q}(x, \mathbf{g}) - \angle h_q(x, \mathbf{g})$ between the desired aperture field phase $\angle h_{0q}(x, \mathbf{g})$ and the simulated aperture field phase $\angle h_q(x, \mathbf{g})$.
4. If the error is acceptable for each input, then the design is complete. If not, then construct new prescribed output aperture fields $h'_{0q}(x, \mathbf{g}) = \angle h_{0q}(x, \mathbf{g}) + w(x)e_{sim}(x)$, where $0 < w(x) < 1$ for all x along the output face. A Tukey window [73] with Tukey parameter $\alpha = 0.1$ is used for $w(x)$.
5. Repeat the design procedure using $h'_{0q}(x, \mathbf{g})$, i.e. return to Step 1.

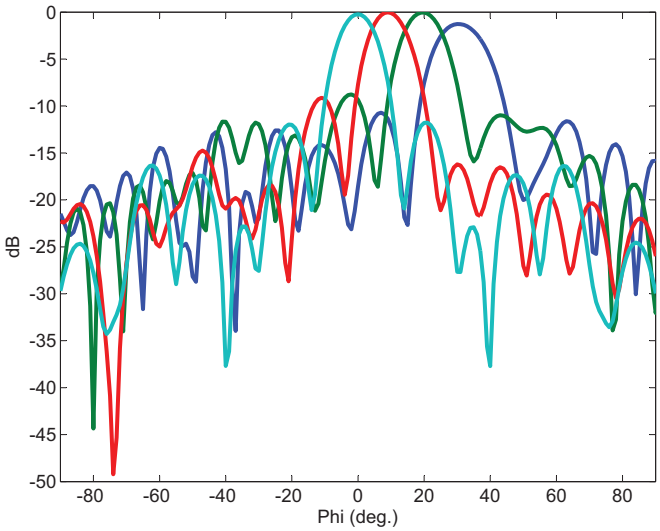

Figure 5.7 Far-field plot of E_θ for the printed beamformer, simulated using the commercial full-wave solver HFSS at 10 GHz. Due to the symmetry of the beamformer, the last three plots are omitted. Each plot is normalized to the far-field plot with the highest magnitude.

5.3.5 Impedance Matching

The input ports are matched to the impedance $Z_0 = 50\Omega$ at 10 GHz. The impedance transformations required for a simultaneous, complex-conjugate match at each port were computed using the S-parameter matrix extracted from the full-wave HFSS simulation of the unmatched beamformer. The matching networks are realized using series transmission lines of particular characteristic impedances, similar to quarter-wave transformers. A 50Ω transmission line connects the edge-launch SMA connectors with the transmission-line matching networks. The matching networks are shown in the final printed-circuit design, provided in Fig. 5.6.

5.3.6 Simulation of Printed-Circuit Design

The final printed-circuit design was simulated using the commercial full-wave solver Ansys HFSS. The simulated, azimuthal, co-polarized far-field plots of E_θ for the beamformer are provided in Fig. 5.7. The results show close agreement with the prescribed design goals at 10 GHz. Simulated gain and radiation efficiencies are provided in Tables 5.1 and 5.2, respectively.

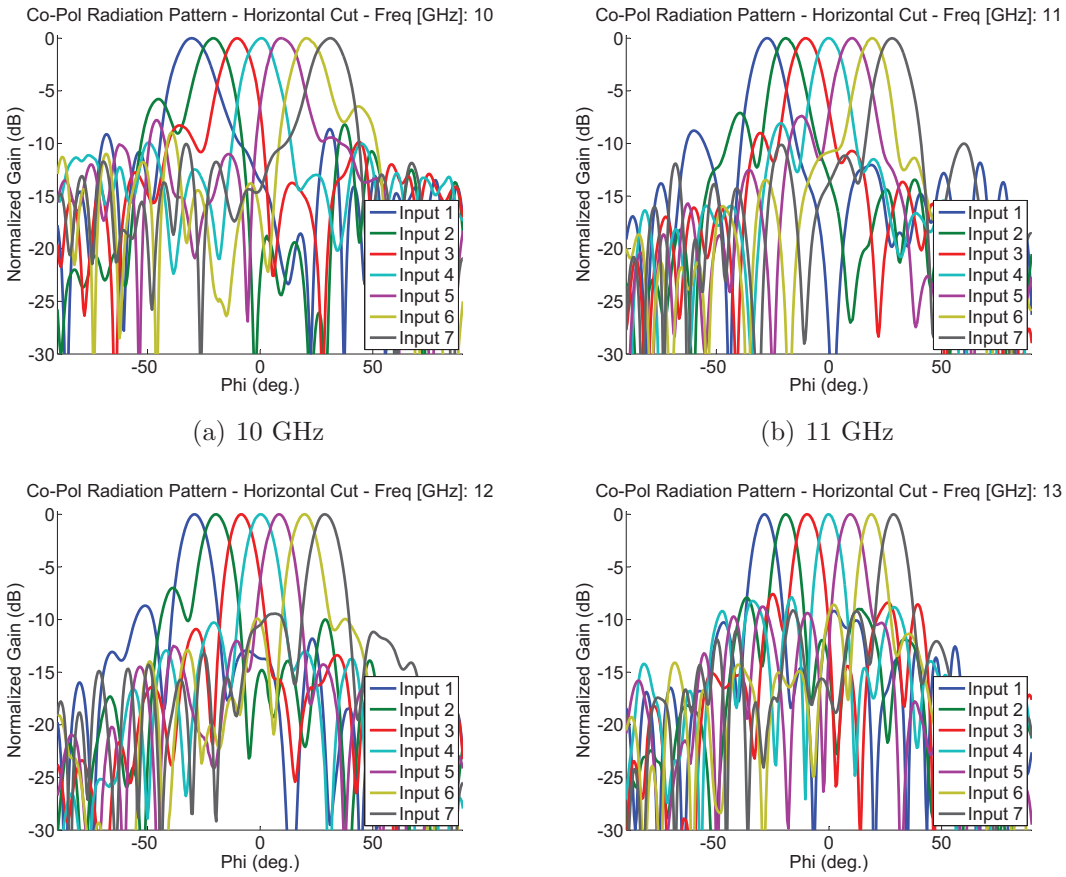

(a) 10 GHz

(b) 11 GHz

(c) 12 GHz

(d) 13 GHz

Figure 5.8 Measured azimuthal, co-polarized far-field patterns. Each plot has been normalized to its own peak.

5.4 Measurement Results

The printed-circuit layout shown in Fig. 5.6 was etched onto the dielectric substrate using a commercial printed-circuit board (PCB) fabrication process. The surface mount resistors, flare, and input connectors were then soldered to the board. Supports for the flare were fabricated using styrofoam.

The measured azimuthal, co-polarized far-field patterns for each input from 10 GHz to 13 GHz are provided in Fig. 5.8. The plots show that the azimuthal angles of the radiated beams match the prescribed angles $\mathbf{\Phi}$ = (-30°, -20°, -10°, 0°, 10°, 20°, 30°) closely over a broad range of frequencies. This frequency invariance is due to the true-time-delay nature of the beamformer. In addition, the sidelobe levels remain low. Cross-polarization levels are low, with measured values of -15dB to -20dB relative to co-polarization. The input S-parameters are provided in Fig. 5.9. The measured gain and 3-dB beamwidths are provided in Tables 5.3 and 5.4, respectively.

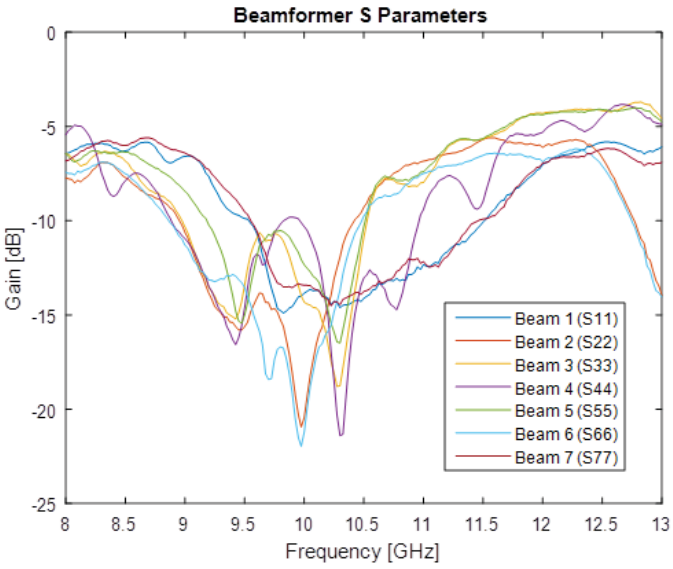

Figure 5.9 Input S-parameters for each of the 7 input ports.

Table 5.3 Measured Gain (dB)

f	1	2	3	4	5	6	7
10.0 GHz	7.7	8.1	7.4	5.6	7.0	7.5	6.5
11.0 GHz	7.5	8.0	9.5	10.0	9.1	7.4	7.0
12.0 GHz	8.7	9.6	9.0	9.9	9.1	10.3	8.1
13.0 GHz	8.9	9.7	6.5	6.7	6.6	10.1	8.6

Table 5.4 Measured 3-dB Beamwidths

f	1	2	3	4	5	6	7
10.0 GHz	18°	15°	14°	14°	15°	15°	16°
10.5 GHz	14°	14°	14°	14°	15°	16°	14°
11.0 GHz	13°	13°	13°	13°	13°	13°	14°
11.5 GHz	13°	12°	12°	12°	12°	12°	12°
12.0 GHz	12°	12°	11°	12°	11°	12°	12°
12.5 GHz	10°	10°	10°	10°	10°	11°	11°
13.0 GHz	9°	9°	11°	9°	10°	9°	9°

Coupling between the input feedlines degrades the radiation patterns between 8 GHz and 9.5 GHz. With improvements in the feedline design, performance at these frequencies could be drastically improved.

5.5 Chapter Summary

This chapter introduced the design of a compact, broadband, printed-circuit beamformer with prescribed output beams. The beamformer is first modeled as a 2D medium featuring a transformation region of unknown inhomogeneous, anisotropic material parameters: scalar permittivity $\epsilon_z(x, y)$ and tensor permeability $\bar{\bar{\mu}}(x, y)$. Then, a recently-developed optimization procedure is employed to design $\epsilon_z(x, y)$ and $\bar{\bar{\mu}}(x, y)$, which can be physically-realized using tensor transmission-line metamaterials.

The beamformer includes 7 input ports designed to radiate beams at the following azimuthal angles: $\mathbf{\Phi}$ = (-30°, -20°, -10°, 0°, 10°, 20°, 30°). Measurement results show that the beamformer achieves the prescribed radiation angles from 10 GHz to 13 GHz while maintaining low sidelobe levels. Simulated radiation efficiencies are between 30% and 43% for each input from 10 GHz to 13 GHz. Performance below 10 GHz is degraded due to coupling between the input feedlines.

The beamformer prototype offers several advantages, including a compact design, the stipulation of arbitrary output fields, flat input/output interfaces, frequency-invariant beams, light weight, and a simple fabrication procedure.

Chapter 6

Planar Loop Resonators for Wireless Power Transfer

6.1 Chapter Introduction

6.1.1 Non-Radiative Power Transfer

Development of wireless power technologies has gained significant attention in recent years to match emerging consumer demands. Wireless power transfer systems can be categorized as either radiative or non-radiative. Radiative techniques developed during the 20^{th} century culminated in the demonstration of microwave-powered helicopter flight in 1964 [74]. However, such far-field techniques often require sophisticated tracking and are susceptible to line-of-sight interference. This is not the case for resonant magnetic coupling, which is a method of wireless non-radiative power transfer (WNPT) first pioneered in the late 19^{th} century [75–77]. This method operates in the near field and is attractive because it is simple, reliable, and inexpensive. Recently, research on resonant magnetic coupling was reinvigorated by the implementation of an efficient mid-range power transfer system in 2007 [11]. Since that time, significant commercial interest has been directed toward wireless power for consumer electronics [12, 13], medical [14–17], and automotive applications [18].

In general, wireless power transmission is a three-step process [74]: DC-to-RF conversion, RF transmission through free space, and RF-to-DC rectification. Therefore, the overall system efficiency depends on the loop-to-loop efficiency as well as the RF conversion and rectification efficiencies. In resonant magnetic coupling, loop-to-loop efficiency is a function of the quality factor Q of the resonant loops, the mutual inductance M between the loops, and impedance matching. The focus of Chapters 6 and 7 is to design compact, high-Q, easy-to-fabricate loop resonators for efficient power transfer.

6.1.2 Loop Resonator Topologies

Coaxial, loop resonators, referred to as shielded-loop resonators [20], were recently used as receiving and transmitting loops in a WNPT system. These resonators are compact, low loss and simple to feed. A similar resonator was subsequently pursued in [78] for WNPT. An RLC circuit model was derived for these loops in [20] using the properties of the coaxial transmission line from which they are constructed. Aside from power transfer, these resonant loops could be used for near-field communication [79, 80]. Non-resonant versions have been used for magnetic-field probing [81, 82].

The loops in [20, 78] were fabricated using lengths of semi-rigid coaxial transmission line. However, these types of loops can be difficult to fabricate. Moreover, their fabrication may not be easily repeatable. An alternative, planar structure made from a printed circuit board (PCB) would not only be simpler to fabricate but would also allow transmission-line properties, such as the characteristic impedance Z_0, to be tailored. These resonators could be used to wirelessly power single chips [83] or 3-D integrated circuits [20, 84, 85]. The demand for chip real estate makes these compact, planar loop resonators advantageous. The planar loop resonators make economical use of space, since the inductance and capacitance are formed using the same conductive loops. This need for compact WNPT structures in practical systems is often stressed in literature [86–88].

6.1.3 Planar Alternatives

In this chapter, planar stripline and microstrip loop resonators are proposed and analyzed. In coaxial shielded loops, currents exist on the interior and exterior of the outer conductor, separated by the skin effect [20]. However, this chapter shows that such separation is not required. Equations for characteristic impedance Z_0, conductor attenuation α_c, and dielectric attenuation α_d [39, 89, 90] are used to develop first-order mathematical models for the stripline and microstrip resonators. The models are compared to both full-wave simulation and measurement. The trends of efficiency versus loop parameters are explored and compared for the different structures. The effect of re-positioning the slit in the ground conductor of the planar loops is also explored.

6.1.4 Chapter Outline

Sec. 6.2 discusses the theory behind the previously-used coaxial shielded-loop resonators. Sec. 6.3 introduces the proposed, planar resonator alternatives. Analytical modeling techniques are reviewed in Sec. 6.4. Comparisons between analysis, simulation, and measurement of the stripline resonator and microstrip resonator are presented in Sec. 6.5 and Sec. 6.6, respectively.

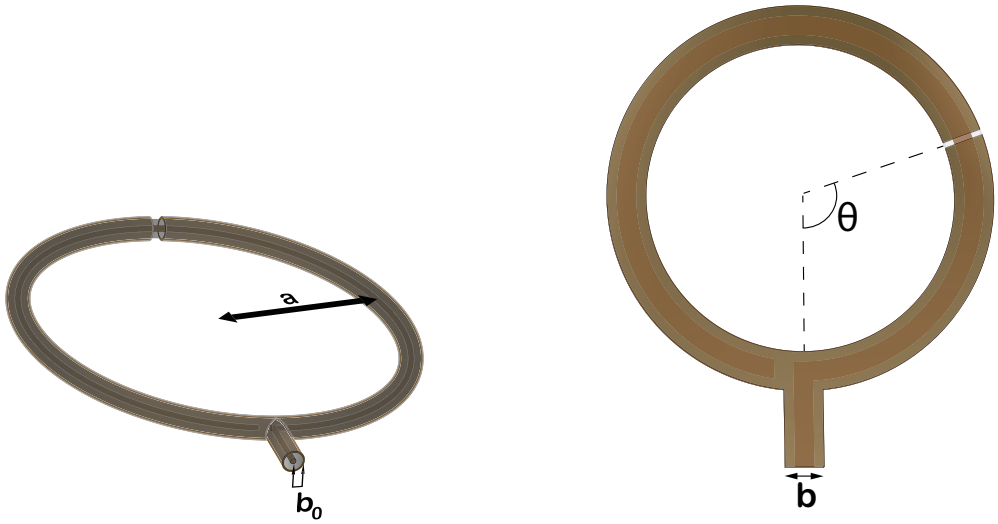

(a) A coaxial shielded-loop resonator. A loop is formed from a length of coaxial transmission line. The outer ground conductors are connected together. The outer conductor in this graphic is semitransparent, revealing that the inner conductor is open-circuited. A small piece of the outer conductor is removed halfway around the loop.

(b) A planar, stripline loop resonator with a shifted slit in the ground conductor. The effect of shifting the slit is discussed in this chapter.

Figure 6.1 Coaxial and planar loop resonators.

6.2 Previous Loop Resonator Topology

The proposed planar loop resonators behave in much the same way as their coaxial counterparts, referred to as coaxial shielded-loop resonators [20]. Therefore, coaxial shielded loops are reviewed before introducing planar loop resonators. In addition, re-positioning the slit in the ground conductor is discussed.

6.2.1 Coaxial Shielded-Loop Resonators

Figure 6.1(a) shows a shielded-loop resonator constructed from a loop of coaxial transmission line with circular cross section. The outer conductor is continuous except for a small slit halfway around the loop. Figure 6.2 shows the behavior of the current on a coaxial shielded-loop resonator. The current enters the input of the loop and propagates along the interior of the coaxial line to the slit in the outer ground conductor. It then wraps around the exterior of the loop to the opposite end of the slit, returning to the interior and ending at the open-circuited stub. The current does not traverse the slit directly due to the high reactance presented by the gap. As a result, the width of the slit does not appreciably affect the resonant frequency. If the outer conductor is thick (several skin depths), a current propagating on the interior of the outer conductor will be isolated from the current

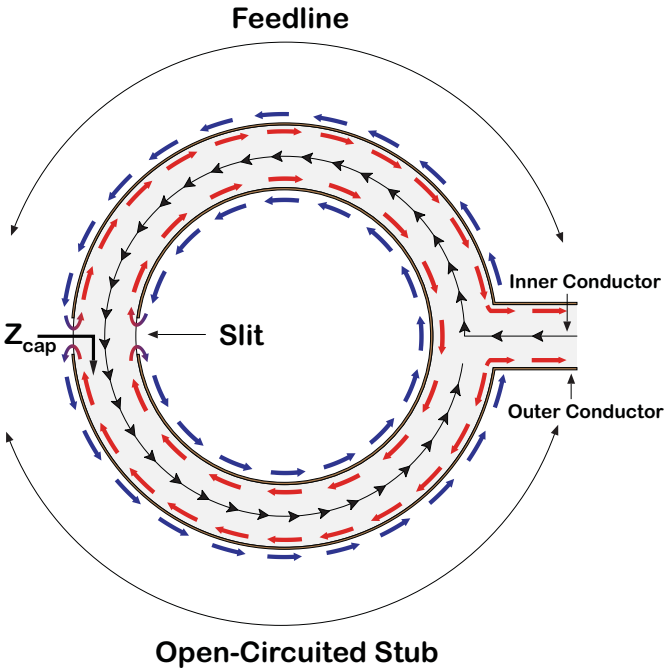

Figure 6.2 The behavior of currents for a coaxial shielded-loop resonator. The current enters the input of the loop and propagates along the interior of the line to the slit in the outer shell. The ground current on the interior (red), wraps around to and propagates along the exterior of the structure (blue). This exterior current returns to the interior and ends in the open-circuited stub section.

propagating on its exterior. This results in a loop current (inductor) in series with the open-circuited stub. The stub can be modeled as a capacitor for electrical lengths less than a quarter-wavelength ($\lambda/4$). Two magnetically-coupled, symmetric, coaxial shielded-loop resonators are modeled by the circuit shown in Fig. 6.3. The circuit includes the feed line, which precedes the slit. The feed line transmission line is characterized by a propagation constant β, a physical length l, and a characteristic impedance Z_0. The parasitic resistance R represents conductor, dielectric, and radiative losses. The input source is represented by input voltage v_s and input impedance R_s.

6.2.2 Circuit Model

As discussed in [20], loop resonators can be modeled as RLC resonators. For a coaxial cross section, the inductance of the loop can be approximated using the following well-known equation [91]:

$$L = \mu r \left[\ln\left(\frac{8a}{b_0}\right) - 1.75 \right]. \tag{6.1}$$

Here, a is the mean radius of the loop and b_0 is the radius of the conductor cross section. For an electrically-small stub of length l ($\beta l << 1$), the impedance Z_{cap} looking into the

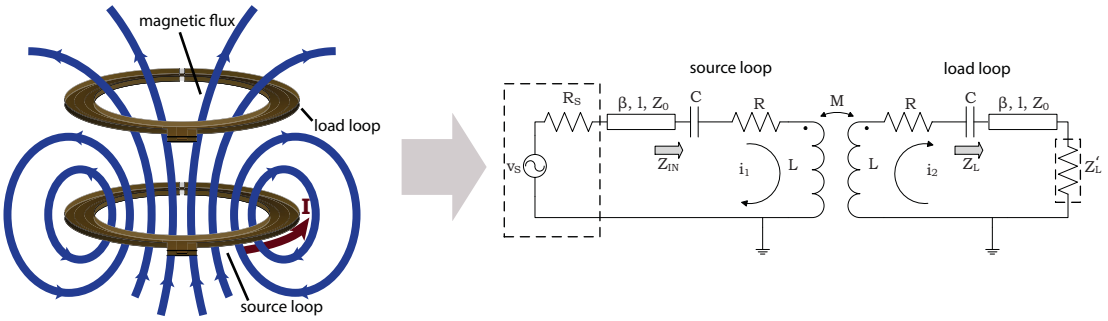

Figure 6.3 Depiction of magnetic coupling between two identical loop resonators and the associated circuit model. The resonators shown are of the planar type presented in this chapter. The feed line transmission line is characterized by a propagation constant β, a physical length l, and a characteristic impedance Z_0. The input source is represented by input voltage v_s and input impedance R_s.

open-circuited stub is:

$$Z_{cap} = \frac{-j}{\omega C} \approx jZ_0/(\beta l) = \frac{-j}{\omega C' l}. \tag{6.2}$$

Therefore, the capacitance of the stub is simply:

$$C = C'l \quad , \quad \beta l << 1. \tag{6.3}$$

Here, C' is the per-unit-length capacitance of the transmission line. From L and C, the resonant frequency can be determined:

$$\omega_0 = \frac{1}{\sqrt{LC}}. \tag{6.4}$$

The resistance R accounts for four loss mechanisms: radiative loss, exterior conductor loss, equivalent series resistance (ESR) of the capacitor, and feed line loss. The resistances representing these losses are given by the following expressions [78]:

$$R_{rad} = 31170 \left(\frac{\pi a^2}{\lambda^2}\right)^2, \tag{6.5}$$

$$R_c = \frac{a}{A'_S}\sqrt{\frac{f\mu\pi}{\pi\sigma}}, \tag{6.6}$$

$$R_{ESR} = Real[Z_0 \coth(\gamma\pi a)], \tag{6.7}$$

$$R_{feed} = R'\pi a, \tag{6.8}$$

where λ is the free-space wavelength at the frequency of operation, γ is the complex propagation constant of the transmission line, R' is the per-unit-length resistance of the transmission line, and A'_S is the outer conductor perimeter for a cross-sectional slice of the loop. For the

coaxial shielded-loop resonator shown in Figure 6.1(a), $A'_S = 2\pi b_0$. The complex propagation constant is defined as in [39]:

$$\gamma = \sqrt{(R' + j\omega L')(G' + j\omega C')}, \tag{6.9}$$

where G' and L' are the per-unit-length dielectric conductance and per-unit-length inductance, respectively. For the circuit model in Figure 6.3, the feed line loss is included in R and the propagation constant γ is purely imaginary ($j\beta$).

In (6.6), a uniformly-distributed surface current is assumed, while (6.8) assumes that the feed line is half the circumference of the loop. For electrically-small loops, R_{ESR} can be simplified to:

$$R_{ESR} = Real\left[\frac{1}{\pi a(G' + j\omega C')}\right]. \tag{6.10}$$

The πa term in (6.7) and (6.10) results from the length of the open-circuited stub being half the loop circumference.

Knowing the transmission-line properties (R', G', L', C'), the external geometry of the structure, and the resonant frequency ω_0 using (6.4), the Q of the resonator can be determined:

$$Q(\omega) = \frac{\omega L}{R}. \tag{6.11}$$

These equations can also be applied to loop resonators made from planar transmission lines, which will be discussed in Sec. 6.3. However, these equations are only an approximation. A more accurate extraction of the resonator parameters can be performed through full-wave simulation. In this chapter, equations (6.1) through (6.11) are referred to as the first-order design equations. For the planar loop resonators presented in Sec. 6.3, another equation is added to relate the width of a planar cross section to the radius of a coaxial cross section.

6.2.3 Location of the Ground Slit

The shielded-loop resonators used previously for wireless non-radiative power transfer employed a slit halfway around the loop [20], as shown in Fig. 6.1(a). For shielded-loops used in field probing, this location is chosen to minimize the probe's response to the electric field [81, 82]. However, this is of less concern for wireless power transfer applications. Furthermore, the arguments made thus far to justify the operation of these planar structures did not stipulate a specified location for the slit. Therefore, a structure with a slit 10° from input (see Fig. 6.1(b)) will be introduced. Reducing the length of the feed line may be advantageous, since this improves the performance of the loop over a broad frequency range (see Appendix D).

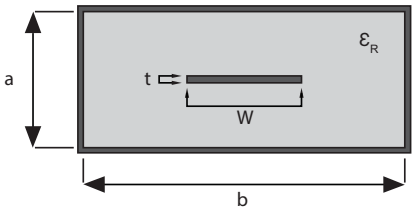

(a) The cross section for a planar analog to the coaxial, shielded-loop resonator using a plated-stripline transmission line. The center conductor is a planar strip and the outer conductor is of rectangular shape.

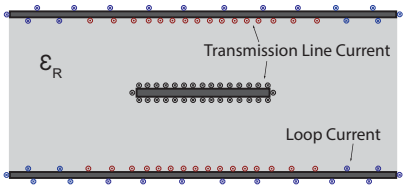

(b) The cross section for the unplated loop resonator using a stripline transmission line. The separation of currents are depicted in the structure. The loop current on the exterior now exists partially on the interior of the ground conductor. This behavior has been verified through full-wave simulation. The opposing currents on the ground conductor will separate.

Figure 6.4 Plated and unplated stripline cross sections for planar loop resonators.

6.3 Planar Shielded-Loop Resonators

Coaxial, shielded-loop resonators (see Fig. 6.1(a)) can be difficult to fabricate, especially with repeatability. A planar structure, like that shown in Figure 6.1(b), made from a printed circuit board is simpler to fabricate and allows tailoring of transmission-line properties, such as the characteristic impedance Z_0. The cross section of a planar loop resonator made from a plated stripline is shown in Fig. 6.4(a). To fabricate this structure, a loop can be cut from a PCB and its edges plated. Without plating, the dielectric on the edges of the loop is exposed, as shown in Figure 6.4(b), and the currents on the interior and exterior of the ground conductor are no longer physically isolated.

In Sec. 6.2, the behavior of the coaxial shielded-loop resonator was explained by the physical separation of the currents on the ground conductor. However, simulation shows that a stripline loop resonator behaves similarly whether it is plated or not (Fig. 6.4(a) and 6.4(b), respectively). For unplated structures, the loop current on the ground conductor naturally separates from the transmission-line current, as shown in Fig. 6.4(b). Therefore, these currents can be treated separately as a transmission-line current and a loop current. It will be shown that there are only minor differences in the extracted resonator parameters for loops having cross sections corresponding to Fig. 6.4(a) or Fig. 6.4(b).

The cross section for an alternative loop resonator using a microstrip transmission line is shown in Fig. 6.5. With only two metal layers, this structure is simpler to fabricate.

Analytically characterizing these planar structures is challenging. For example, the inductance is not solely due to the outer loop current, since the transmission line itself contributes to the overall inductance. However, a first-order approximation can be made with some simplifying assumptions. In particular, let's assume that the loop current flows uniformly on the exterior of the ground conductor. The formulas for resistive loss then

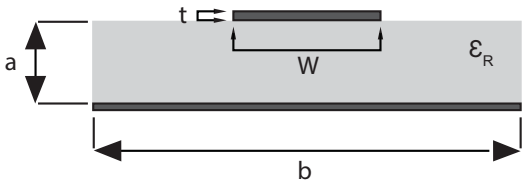

Figure 6.5 The cross section for a loop resonator using a microstrip transmission line.

become significantly simpler. The capacitance from the open-circuited stub can be easily approximated using (6.3). Assuming that the transmission line does not contribute to the total loop inductance, the inductance of a thin annulus can be used. This chapter combines equation (6.1) with the following relationship:

$$b_0 = \frac{b}{4}, \tag{6.12}$$

where b_0 is the radius of the conductor cross section in equation (6.1) and b is the width of planar cross section in the planar structure (see Fig. 6.4(a)). This relationship between round wires and strips can be found in [92]. For each type of loop resonator, the properties of the transmission line and the geometry of the loop are all that are needed for this first-order analysis.

6.4 Analytical Modeling

In Sec. 6.2, the theory governing the loop resonators was presented along with a corresponding RLC model. To determine the values of R, L, and C, the geometry and transmission-line properties of the resonators must be used. Therefore, design equations for both stripline and microstrip transmission lines are presented in this section. The resulting models will be subsequently compared to both simulation and experiment.

6.4.1 Useful Transmission-Line Equations

In this chapter, Wheeler's formulas are used to compute the characteristic impedance Z_0 of a centered stripline [89]. The formulas from Hammerstad and Jensen are used to calculate the characteristic impedance Z_0 of a microstrip transmission line [90].

The equations for Z_0 can also be used to calculate R', G', C', and L'. Indeed, the conductor attenuation α_c is computed using Wheeler's incremental inductance rule, which is valid for any type of transmission line [39]:

$$\alpha_c = \frac{R_s}{2Z_0\eta}\frac{dZ_0}{dl}, \tag{6.13}$$

where l refers to the distance by which the walls of the conductors recede (see [39]) and R_s is the sheet resistance of the conducting surfaces, which can be derived from the frequency f and conductivity σ [39]:

$$R_s = \sqrt{\frac{f\mu\pi}{\sigma}}. \tag{6.14}$$

Equation (6.14) assumes a uniform current distribution on the conductor's surface. However, due to the proximity effect this is only an approximation [93]. Therefore, the conductor attenuation α_c will be slightly higher than predicted by (6.13).

The dielectric attenuation α_d is computed using the following formula presented in [39], which is also valid for any type of transmission line:

$$\alpha_d = \frac{k \tan \delta}{2} (Np/m). \tag{6.15}$$

The per-unit-length resistance R' and conductance G' are also needed. From [94], these can be computed for a transmission line using α_c and α_d, respectively:

$$R' = 2\alpha_c Z_0, \tag{6.16a}$$

$$G' = \frac{2\alpha_d}{Z_0}. \tag{6.16b}$$

The per-unit-length capacitance C' and inductance L' are required as well. Since the transmission-line fields are quasi TEM:

$$v_p = \frac{c}{\sqrt{\epsilon_{eff}}}, \tag{6.17a}$$

$$C' = \frac{1}{v_p Z_0}, \tag{6.17b}$$

$$L' = Z_0^2 C'. \tag{6.17c}$$

Here, v_p is the phase velocity of the wave and ϵ_{eff} is the effective permittivity of the transmission line. For stripline, $\epsilon_{eff} = \epsilon_R$, where ϵ_R is the relative permittivity of the dielectric.

Using R', G', L', C', and Z_0 for the various geometries, the values of R, L, and C for the circuit model (see Figure 6.3) are calculated. The resulting Q and resonant frequency f_0 for each geometry is compared to those extracted from full-wave simulation.

6.5 Stripline Loop Resonators

Stripline loop resonators are simulated using the commercial electromagnetic solver Ansys HFSS. To extract the resonator R, L, and C parameters, the S-parameters are de-embedded to the location of the slit. Then, the de-embedded input impedances are used to extract the RLC parameters.

6.5.1 Extraction Example

To demonstrate the RLC extraction procedure for these structures, an example is provided here for a plated-stripline loop resonator with an inner conductor width $W = 10$ mm. From the full-wave simulation, the characteristic impedance Z_0 and electrical length βl of the feed line is found to be 17.6 Ω and 17.8° respectively, at 30 MHz. Using these numbers, the simulated input impedance $Z_{IN}(f)$ versus frequency f is de-embedded to the location of the slit by first converting to S-parameters and applying a frequency-dependent phase shift:

$$S_{11} = \frac{Z_{IN}(f) - Z_0}{Z_{IN}(f) + Z_0}, \tag{6.18}$$

$$S'_{11} = S_{11} e^{j2\pi \frac{17.8}{180} \frac{f}{30}}. \tag{6.19}$$

Here, S'_{11} denotes the de-embedded S-parameters, f is in MHz, and $Z_0 = 17.6$ Ω. The de-embedded input impedance $Z'_{IN}(f)$ is given as:

$$Z'_{IN}(f) = Z_0 \frac{1 + S'_{11}}{1 - S'_{11}}. \tag{6.20}$$

The resonant frequency f_0 is given by the frequency at which $\mathrm{Im}\{Z'_{IN}(f_0)\} = 0$. The input reactances at two distinct frequencies near f_0 is used to determine L and C. The resonator resistance R is simply the real part of the input impedance at resonance. The RLC parameters for the selected example are provided in Table 6.1.

6.5.2 Plated-Stripline Resonator

First, a set of plated-stripline resonators with varying inner conductor widths are simulated to test the model presented in Sec. 6.2. Referring to the cross section in Fig. 6.4(a), the properties of the simulated loop were:

- Conductor: copper ($\sigma = 5.8e7$ S/m)
- Dielectric: Rogers RT/Duroid 5880

Table 6.1 Parameters for plated-stripline resonator from full-wave simulation.

W	f_0 (MHz)	L (μH)	C (pF)	R (Ω)	$Q(f_0)$
2 mm	54.7	0.400	21.2	0.532	258
3 mm	49.1	0.379	27.7	0.394	297
4 mm	44.9	0.376	33.5	0.325	325
5 mm	41.7	0.367	39.7	0.279	345
6 mm	39.2	0.357	46.4	0.240	365
7 mm	37.0	0.350	52.9	0.215	378
8 mm	35.2	0.342	59.9	0.195	388
9 mm	33.6	0.344	65.5	0.183	396
10 mm	32.2	0.337	72.6	0.166	410

- ϵ_R: 2.2
- $\tan\delta$: 0.009
- Copper thickness (t): 70 μm
- Loop radius (r_0): 9 cm
- Cross-sectional width (b): 20 mm
- Cross-sectional thickness (a): 3.32 mm

From the extracted data, shown in Table 6.1, a few observations can be made. The resistance of the resonator decreases with increasing signal trace width W. Narrower widths exhibit higher loss due to increased current densities. Loop inductance also decreases with increasing signal width W. This is because the transmission line contributes to the overall inductance of the structure. This contribution decreases with increasing width W. Such a phenomenon can be seen even from (6.1), where the inductance of a loop of coaxial cross section decreases with increasing cross-sectional radius.

Figure 6.6 shows the resonant frequency and Q factor extracted from full-wave simulation compared with those computed using the first-order design equations presented in Sec. 6.2. The computed resonant frequencies match fairly well with simulation and the Q factors exhibit the proper trend. The design equations generally overestimate the Q factor.

6.5.3 Unplated Stripline Resonator

Next, a set of unplated-stripline resonators (see Fig. 6.4(b)) with varying inner conductor widths are simulated. The geometry and material properties are the same as for the plated case, but without metal plating on the edges.

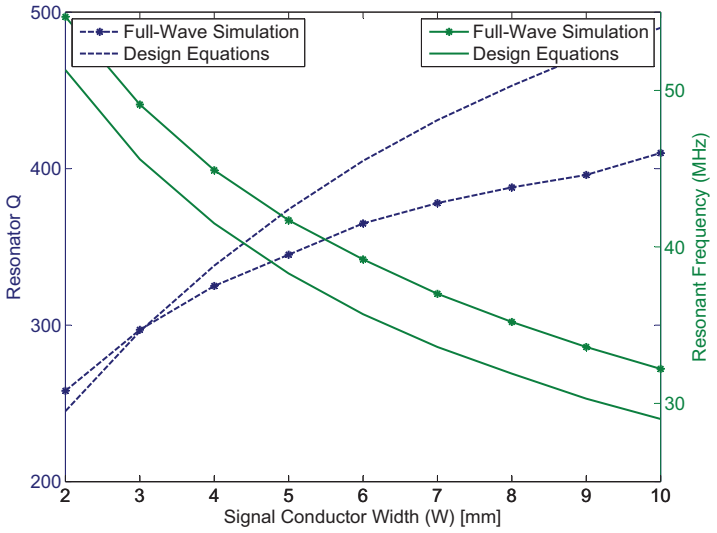

Figure 6.6 The Q factor and resonant frequency of plated-stripline loop resonators as a function of signal width W (see Figure 6.4(a)). Calculated results using first-order design equations are compared to those from simulation.

Table 6.2 Parameters for unplated stripline resonator from full-wave simulation.

W	f_0 (MHz)	L (μH)	C (pF)	R (Ω)	$Q(f_0)$
2 mm	54.5	0.406	21.0	0.527	264
3 mm	49.1	0.381	27.6	0.381	308
4 mm	45.0	0.372	33.6	0.343	307
5 mm	41.8	0.362	40.0	0.264	360
6 mm	39.2	0.357	46.0	0.231	382
7 mm	37.1	0.353	52.2	0.205	401
8 mm	35.3	0.344	59.3	0.183	415
9 mm	33.7	0.338	66.1	0.168	427
10 mm	32.3	0.336	72.2	0.155	440

From Table 6.2, the extracted resonator parameters for the unplated-stripline resonators are essentially the same as for the plated-stripline resonators. However, the resistances of the unplated loops are slightly higher than for the plated loops. This occurs because the current is more spread out on the plated loop. Thus, plating the loops lowers the resistance but also adds a fabrication step.

6.5.4 Plated-Stripline Resonator with Shifted Slit

As mentioned in Sec. 6.2, the slit in the ground conductor need not be placed opposite the input. Moving the slit toward the input feed line simply increases the length of the

Table 6.3 Parameters for plated-stripline resonator with shifted ground slit from full-wave simulation.

W	f_0 (MHz)	L (μH)	C (pF)	R (Ω)	$Q(f_0)$
2 mm	37.8	0.416	42.5	0.388	255
3 mm	34.0	0.396	55.4	0.302	280
4 mm	31.2	0.386	67.5	0.255	296
5 mm	29.0	0.368	81.8	0.219	306
6 mm	27.3	0.360	94.5	0.194	319
7 mm	25.8	0.351	108.5	0.175	326
8 mm	24.5	0.348	121.1	0.164	327
9 mm	23.5	0.338	136.2	0.147	339
10 mm	22.5	0.335	149.0	0.139	343

Table 6.4 Comparison of simulation, experiment, and the first-order model for the unplated- stripline loop resonator ($W = 10$ mm).

	f_0 (MHz)	L (μH)	C (pF)	R (Ω)	$Q(f_0)$
Simulation	32.3	0.336	72.2	0.16	440
Measurement	32.1	0.326	75.4	0.20	348
Model	29.0	0.364	82.5	0.14	490

capacitive stub section. In addition, it decreases the length of the input feed line, which does not contribute to either the structure's overall inductance or capacitance, and can adversely affect the efficiency of a WNPT system (see Appendix D). Therefore, structures are also simulated for loops with the slit in the ground conductor 10° from the input feed line (see Fig. 6.1(b)). All other dimensions are the same as before. The extracted data is given in Table 6.3. From Table 6.3, the capacitance of the structure doubles, while the inductance remains roughly the same. Furthermore, the resistance of the structure decreases. Although the frequencies are lower, the Q of the structure at resonance is slightly larger due to the reduced loss.

6.5.5 Experimental Results

Unplated stripline loops with a ground slit opposite the input were fabricated to compare with the simulation and the analytical model. Two Rogers RT/Duroid 5880 substrates were etched, bonded together using FR406 no-flow prepreg, and cut to form the loops. Figure 6.7 shows the fabricated stripline loop resonator. The dimensions of the loop are the same as that for the loop described by Table 6.2. A trace width $W = 10$ mm is used. The simulation and experimental results for this loop are shown in Table 6.4.

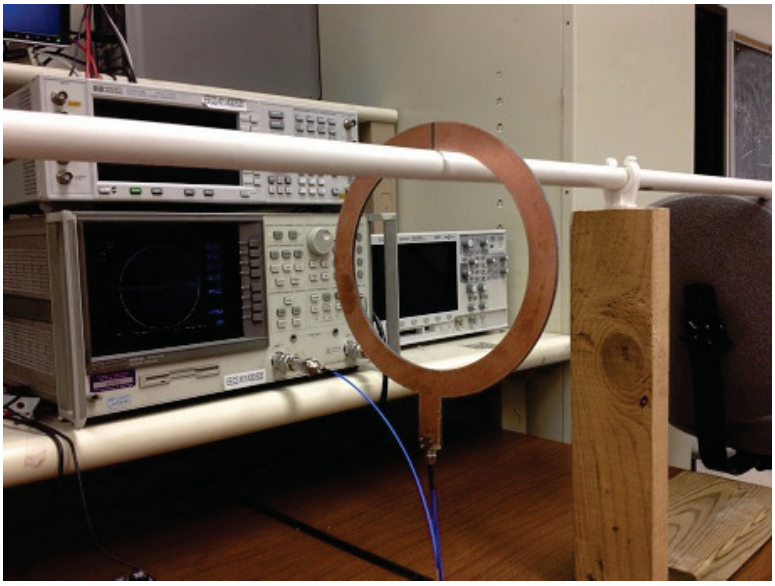

Figure 6.7 A plated-stripline loop resonator. The radius of the loop is 9 cm.

6.6 Microstrip Loop Resonators

Microstrip loop resonators are simulated using the commercial electromagnetic solver HFSS. The resonator parameters R, L, and C are determined using the methods presented in Sec. 6.4.

6.6.1 Simulation Results

A set of planar, microstrip loop resonators with varying signal conductor widths are simulated to compare to the stripline loop resonators. The same dielectric and conductor as before are used. Referring to Fig. 6.5, the other properties of the loop were:

- r_0: 9 cm
- Cross-sectional width (b): 20 mm
- Cross-sectional thickness (a): 1.575 mm

From Table 6.5, it can be seen that the capacitance of the microstrip structure is lower than for the stripline structure. This follows from the decreased per-unit-length capacitance of the microstrip transmission line. The total inductance is increased because the height of the structure is decreased and the current on the ground conductor is more confined.

The resistance of the structure is lower compared to the stripline structure at similar frequencies. This is due to the fact that the fields partially exist in the air above the substrate, resulting in lower dielectric loss. However, this also means that the effective

Table 6.5 Parameters for microstrip resonator from full-wave simulation.

W	f_0 (MHz)	L (μH)	C (pF)	R (Ω)	$Q(f_0)$
2 mm	68.6	0.414	13.0	0.598	299
3 mm	61.6	0.409	16.4	0.477	331
4 mm	57.1	0.391	19.9	0.394	356
5 mm	53.4	0.381	23.4	0.343	372
6 mm	50.9	0.372	26.4	0.291	407
7 mm	48.4	0.362	29.8	0.256	430
8 mm	46.0	0.367	32.6	0.248	427
9 mm	44.2	0.364	35.6	0.229	442
10 mm	42.8	0.358	38.7	0.203	474

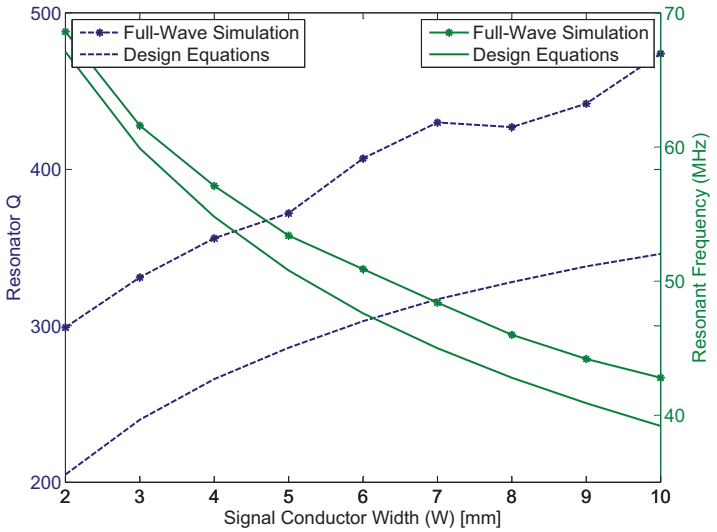

Figure 6.8 The Q factor and resonant frequency of microstrip loop resonators as a function of signal width W (see Figure 6.5). Calculated results using first-order design equations are compared to those from simulation.

permittivity of the structure can be affected by objects in air directly above the substrate. Thus, the capacitance of the overall structure can be altered, which will detune the resonator. This is one disadvantage of the microstrip structure. On the other hand, fewer conductor layers are required and losses are lower.

Figure 6.8 shows the resonant frequency and Q factor extracted from full-wave simulation compared with those computed using the first-order model in Sec. 6.2. Again, the computed resonant frequencies match fairly well, and the Q factors exhibit the proper trend. The design equations, however, underestimate the Q factor.

Table 6.6 Parameters for microstrip resonator with shifted ground slit from full-wave simulation.

W	f_0 (MHz)	L (μH)	C (pF)	R (Ω)	$Q(f_0)$
2 mm	46.4	0.443	26.5	0.369	350
3 mm	42.4	0.431	32.7	0.289	398
4 mm	39.3	0.421	39.0	0.267	389
5 mm	36.9	0.407	45.8	0.234	403
6 mm	34.8	0.408	51.3	0.219	407
7 mm	32.9	0.401	58.2	0.209	398
8 mm	31.5	0.377	67.6	0.185	403
9 mm	30.3	0.384	71.8	0.179	409
10 mm	29.3	0.375	79.0	0.167	412

Table 6.7 Parameters of RLC resonator using lumped matching.

f_0 (MHz)	L (μH)	C (pF)	R (Ω)	$Q(f_0)$
42.4	0.469	30.0	0.244	512

6.6.2 Microstrip Resonator with Shifted Slit

As with the stripline structures, a microstrip loop resonator with the ground slit shifted 10° from the feed is also simulated. The extracted resonator parameters are shown in Table 6.6. As before, the capacitances double while the inductances remain roughly the same. The Q factor of these resonators are similar to the original microstrip resonators described in the previous section, despite the lower frequencies.

6.6.3 Comparison with Lumped Matching

Here, the performance of the non-shifted microstrip loop resonator of width $W = 10$ mm is compared to the traditional lumped topology. To this end, an inductive loop is simulated using the commercial electromagnetic solver Ansys HFSS. The loop has radius $r_0 = 9$ cm and width 20 mm. The resulting inductance is $L = .469$ μH and the parasitic resistance is $R = 0.184$ Ω. To match the resonant frequency $f_0 = 42.9$ MHz to that of the microstrip resonator, a 30 pF lumped capacitor is selected from Murata with equivalent series resistance of 0.06 Ω. The result is an RLC resonator with characteristics given in Table 6.7.

Although the Q and inductance of the lumped system is higher, achievable resonant frequencies are limited by by the availability of lumped capacitors. Moreover, the lumped capacitors limit the power-handling capabilities of the system.

Table 6.8 Comparison of simulation, experiment, and the first-order model for the microstrip loop resonator ($W = 10$ mm).

	f_0 (MHz)	L (μH)	C (pF)	R (Ω)	$Q(f_0)$
Simulation	42.8	0.358	38.7	0.20	474
Measurement	42.1	0.347	41.3	0.24	381
Model	39.2	0.364	45.3	0.26	346

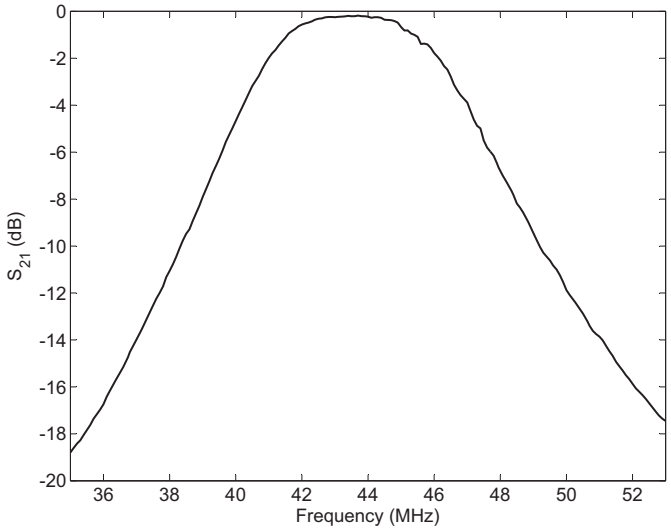

Figure 6.9 Power transfer efficiency for two coupled microstrip loop resonators separated by 10 cm. A trace width $W = 10$ mm and an ideal L-matching network are assumed.

6.6.4 Experimental Results

Microstrip loops with a ground slit opposite the input were fabricated to compare with simulations and the analytical model. The loops were milled and cut from a Rogers RT/Duroid 5880 substrate. The dimensions of the loop are the same as that for the loop described by Table 6.5. A trace width $W = 10$ mm is used. The simulation and experimental results for this loop are shown in Table 6.8.

6.6.5 Bandwidth

To explore the bandwidth of a system of coupled loops, the S-parameters of two microstrip loop resonators ($W = 10$ mm) separated by 10 cm are measured. The power transfer efficiency S_{21} is plotted in Figure 6.9 assuming an impedance match at 42.8 MHz using an ideal L-matching network. The system achieves a power transfer efficiency of 96% and a 3-dB bandwidth of 6 MHz. Since wireless power transfer systems typically employ continuous waves, this bandwidth is sufficient.

6.7 Chapter Summary

This chapter introduced planar alternatives to coaxial shielded-loop resonators with a circular cross section, used previously for wireless non-radiative power transfer (WNPT). It was shown that physically shielding the transmission-line current from the inductive loop current is not required to maintain the resonant behavior of the structure. Therefore, the stripline loops' edges need not be plated. Structures with varying conductor widths were analyzed and simulated. Increased widths lowered both loss and the resonant frequency. For the same signal trace width W, the microstrip loops exhibited higher Q values than the stripline loops. Structures were fabricated and their measured values matched well with simulation.

These planar loops offer a number of advantages over other resonant loops. First, the structures are inherently suitable for printed circuit boards and integrated circuits, since they are planar. Second, the structures are physically compact. Essentially, these structures are capacitors made from a pair of conductive annuli onto which a loop current (inductance) is impressed. Third, the widths of the signal conductor can be easily varied to manipulate the loop parameters, such as the characteristic impedance. Fourth, the power-handling capabilites are superior to a simple loop with a lumped series capacitor. Finally, the fabrication variance for the capacitance of the structure is lower than that of a lumped series capacitor.

It was also shown in simulation that the location of the slit in the ground conductor of the proposed loops need not be directly opposite the input feed line. Instead, its location can be used to vary the capacitance and therefore the resonant frequency of the resonators. Moreover, a significant length of feed line can adversely affect the performance of the WNPT system (see Appendix D).

In the next chapter, it is demonstrated that the parameters of the loop resonator can be tailored to provide a 2-port, complex-conjugate impedance match at a prescribed distance, thereby eliminating the need for external matching networks.

Chapter 7

Self-Matching for Planar Loop Resonators

7.1 Chapter Introduction

7.1.1 Self-Matching

The focus of this chapter is to design high-Q, planar loops using distributed impedance-matching elements incorporated into the structure itself, thereby alleviating external matching requirements. To this end, the planar loop resonators introduced in Chapter 6 are redesigned. Specifically, the feedline and capacitive stub of the resonators are tailored to ensure the coupled loops are impedance matched at a prescribed coupling distance. This self-matching technique is advantageous because it removes the need for external matching networks. Moreover, a self-matched WNPT system is inherently more compact.

7.1.2 Chapter Outline

In this chapter, a brief review of the WNPT system using planar loop resonators proposed in Chapter 6 is presented in Sec. 7.2. In Sec. 7.3, the theory of impedance matching using transmission lines and capacitive stubs integrated into the resonator is reported. In Section 7.4, an analysis of system parameters such as characteristic impedance, dielectric material, and dielectric thickness is provided. From this analysis, a comprehensive design procedure is proposed and used to develop two pairs of resonators in Section 7.5. The first pair is designed for a full, 2-port impedance match at a coupling distance of 15 cm (1.67 loop radii), while the second is designed for 20 cm (2.22 loop radii). The designs yield loop-to-loop power transfer efficiencies of 91% and 85%, respectively.

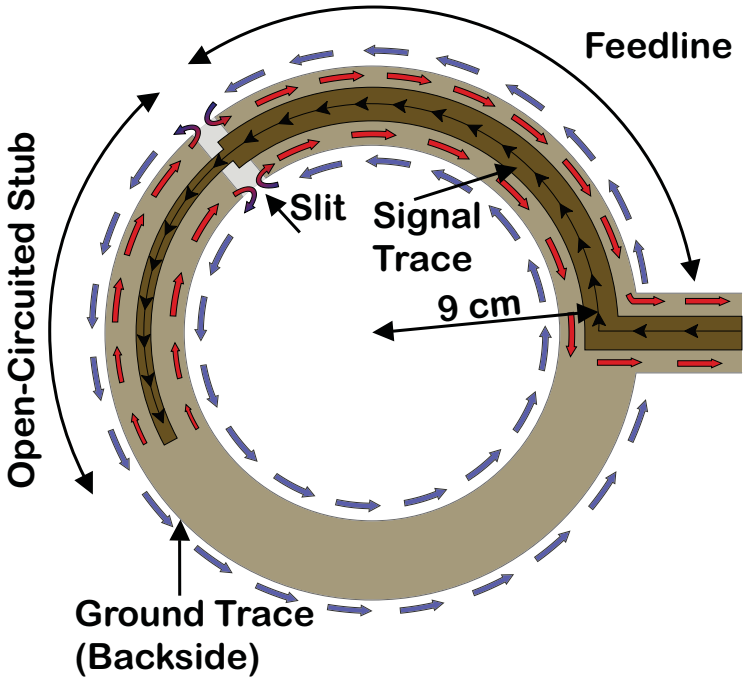

(a) The currents along the planar loop resonator. The current enters the input of the loop and traverses the transmission line. Upon reaching the slit, the current on the interior of the ground conductor wraps around to the exterior. After looping around to the opposite side of the slit, the current terminates at the open-circuited stub. A single planar loop resonator is shown here, but the full system requires two coaxially-aligned loops.

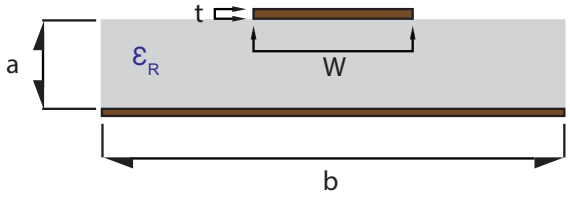

(b) Cross section of the microstrip loop resonator.

Figure 7.1 The proposed self-matched microstrip loop resonator for wireless non-radiative power transfer (WNPT). The feedline and capacitive stub can be designed to achieve an impedance match at a prescribed coupling distance.

7.2 System Overview

7.2.1 Review of Loop Resonators

The planar loop resonators employed in this chapter were first discussed in Chapter 6, and an example is illustrated in Figure 7.1(a). These structures are realized by forming a loop using a length of planar transmission line. The ground conductor of the resulting annulus

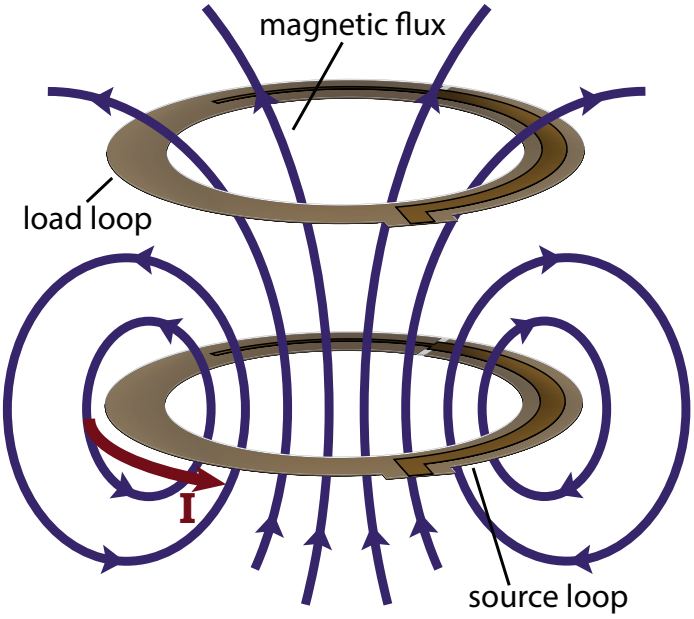

(a) Magnetic coupling between loop resonators.

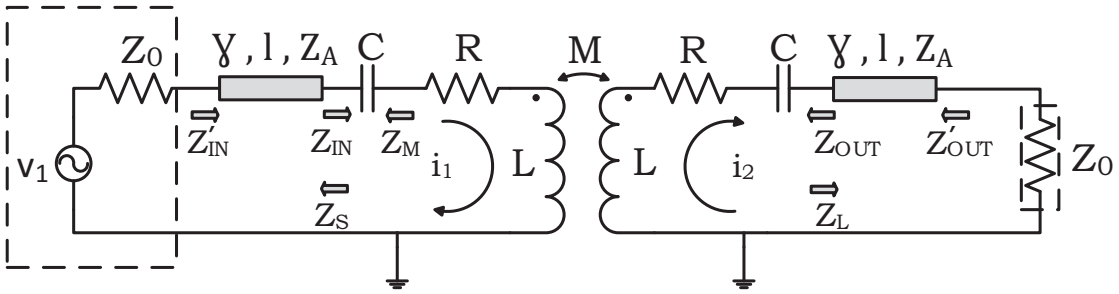

(b) Circuit model for magnetically-coupled loop resonators.

Figure 7.2 Depiction of the magnetic coupling between two identical loop resonators and the associated circuit. The coupling is represented by the mutual inductance M.

is continuous except for a small slit at a prescribed distance from the input. The signal conductor's width may vary and is ultimately left open-circuited, as shown in the figure. Convenient planar transmission lines to use include microstrip and stripline. In this chapter, microstrip realizations are the focus due to their ease of fabrication. The cross section of a microstrip line is shown in Figure 7.1(b).

Figure 7.1(a) also depicts the current flow along the loop resonator. The current enters

the input of the loop and traverses the transmission line. Upon reaching the slit, the current on the interior of the ground conductor wraps around to the exterior, where it loops around to the opposite side of the slit. The current then returns to the interior of the ground conductor and terminates at the open-circuited stub. Essentially, the result is a loop inductance in series with an open-circuited stub, which acts as a capacitor. The feedline before the slit is modeled as a transmission line.

7.2.2 Coupled System

Figure 7.2 shows a system of symmetric, magnetically-coupled loop resonators. The magnetic coupling is represented by the mutual inductance M, which decreases with increasing separation of loop resonators. The parasitic resistance R represents conductor, dielectric, and radiation losses, as in Chapter 6. The input feedline is characterized by a complex propagation constant $\gamma = \alpha + j\beta$, a physical length l, and a characteristic impedance Z_A. The attenuation constant α along the feedline is assumed small ($\alpha \approx 0$). Maximum power transfer efficiency occurs for a 2-port complex-conjugate match, given by:

$$Z_S = Z_L = Z_{IN}^* = Z_{OUT}^*. \tag{7.1}$$

For the symmetric system (identical loops) of magnetically-coupled loop resonators in Figure 7.2, the input impedance Z_{IN} is given by [20]:

$$Z_{IN} = j(\omega L - \frac{1}{\omega C}) + R + \frac{(\omega M)^2}{j\omega L - \frac{j}{\omega C} + R + Z_L}. \tag{7.2}$$

As discussed in [20], combining (7.1) and (7.2) gives the condition for a 2-port complex-conjugate match:

$$Z_S = Z_{IN}^* = j(\frac{1}{\omega C} - \omega L) + \sqrt{R^2 + (\omega M)^2}, \tag{7.3}$$

$$Z_M = -j\omega L + \sqrt{R^2 + (\omega M)^2}. \tag{7.4}$$

The goal of this chapter is to tailor the parameters of planar loop resonators to satisfy condition (7.3) without using external matching networks.

7.2.3 Frequency Tuning

From (7.3), the optimal impedance conditions depend on the mutual impedance M, which varies with the relative orientation and separation of the coupled loops. Therefore, it is

difficult to maintain an impedance match over a range of coupling distances. One solution is to use active matching networks that dynamically tune impedances, as discussed in [19, 95]. However, such systems are often complex. As a compromise between simplicity and improving efficiency, frequency-tuning methods can be used [19, 95]. In frequency-tuned systems, the operating frequency of the system tracks one of two resonant frequencies of the WNPT system resulting from the frequency splitting that occurs when the loops are strongly coupled. The higher of these two frequencies is referred to as the odd mode, while the lower is referred to as the even mode [20, 95]. In Section 7.5, experimental efficiency data will be provided for the frequency-tuned system.

7.3 Matching With Low-Impedance Lines

In single-stub impedance matching, a length of transmission line and a stub can be used to match a passive load impedance to a characteristic impedance Z_0 [39]. The stub serves as a reactive element. Inspection of Figure 7.2(b) shows that the planar loop resonator intrinsically incorporates a transmission line in series with a capacitor (reactive element) into its structure. Therefore, one can consider exploiting the feedline and capacitive stub to achieve a 2-port impedance match. This is similar to the series-stub matching method. Matching equations are derived for this case and presented next.

7.3.1 Matching Equations

Figure 7.3 demonstrates the proposed impedance transformation from Z_0 to Z_M on a Smith chart. Two examples are provided in the figure. Here, a transmission line of characteristic impedance Z_A and electrical length βl transforms the impedance Z_0 to Z_S, which must lie on the same constant resistance circle as Z_M. Then, a series capacitor translates the impedance to the point Z_M. Appendix E provides an alternative explanation that helps visualize the constraints on Z_A and βl.

Consider the case when all design parameters are fixed except for three variables: Z_A, C, and βl. From (7.4), Z_M is fixed. The required values of these three variables for an impedance match can be derived by writing an equation for impedance Z_S using the well-known equation for the impedance at the input of a transmission line [39]:

$$Z_S = Z_A \frac{Z_0 + jZ_A \tan(\beta l)}{Z_A + jZ_0 \tan(\beta l)}. \tag{7.5}$$

Here, Z_0 acts as the load impedance in the equation. Using (7.1) and (7.5), an equation

for βl can be derived:

$$\beta l = \tan^{-1}\left(-j\frac{(Z_0 - Z_{IN}^*)Z_A}{Z_0 Z_{IN}^* - Z_A^2}\right) \in \mathbb{R}. \tag{7.6}$$

From (7.6) it is clear that since $\beta l \in \mathbb{R}$, then the following condition must be satisfied:

$$\mathrm{Re}\left\{\frac{(Z_0 - Z_{IN}^*)Z_A}{Z_0 Z_{IN}^* - Z_A^2}\right\} = 0. \tag{7.7}$$

Therefore:

$$Z_A = \sqrt{\frac{Z_0^2 R_{IN} - Z_0|Z_{IN}|^2}{Z_0 - R_{IN}}}, \tag{7.8}$$

and as a result:

$$\beta l = \tan^{-1}\left(\frac{Z_A X_{IN}(Z_0^2 - Z_A^2)}{(Z_0 R_{IN} - Z_A^2)^2 + (Z_0 X_{IN})^2}\right). \tag{7.9}$$

The values of X_{IN} and R_{IN} can be determined from the capacitance C and mutual coupling M, respectively. Since an impedance match is desired, from (7.3) X_{IN} must be equal to:

$$\begin{aligned} X_{IN} &= j(\omega L - \frac{1}{\omega C}), \\ C &= \frac{1}{\omega^2 L - \omega X_{IN}}. \end{aligned} \tag{7.10}$$

Similarly, R_{IN} must be equal to:

$$R_{IN} = \sqrt{R^2 + (\omega M)^2}. \tag{7.11}$$

For design purposes, consider the low-loss case ($R \approx 0$). In this case:

$$R_{IN} \approx \omega M. \tag{7.12}$$

Using (7.8), (7.9), (7.10), and (7.12), the characteristic impedance Z_A and electrical length βl can be determined for a given ω, M, Z_0, and C. In this case, C is a free parameter. Alternatively, one could set Z_A and solve for C. In this case, X_{IN} can be written as a function of Z_A using (7.8):

$$X_{IN} = \sqrt{Z_0 R_{IN} - \frac{Z_A^2(Z_0 - R_{IN})}{Z_0} - R_{IN}^2}. \tag{7.13}$$

In the derivation of (7.13), both a positive and negative sign in front of the square root

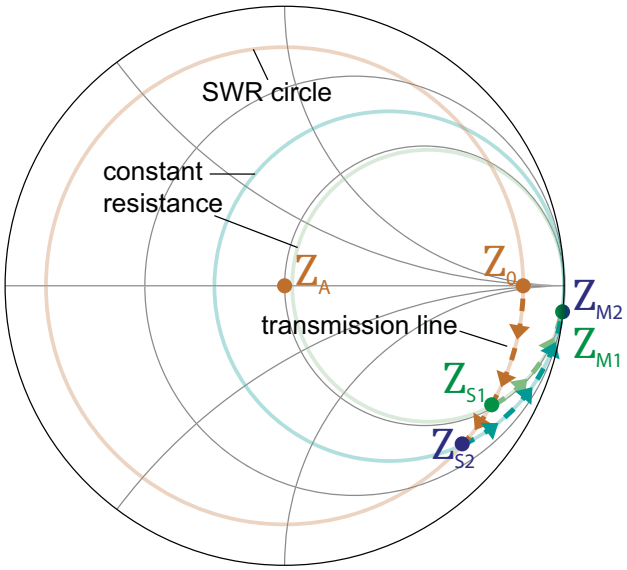

Figure 7.3 The impedance transformation curves for two different WNPT system designs are provided. The mutual coupling M for Design 1 (green) is larger than that of Design 2 (blue). Therefore, $R_{IN1} > R_{IN2}$, as shown in the Smith chart. Appendix E provides an alternative view of the impedance transformation.

are valid. However, a positive sign is chosen for the square root so that βl from (7.9) is minimized. The capacitance C can then be determined by substituting (7.13) into (7.10). Note that (7.13) constrains the value of Z_A (with $Z_A < Z_0$) to:

$$Z_A \leq \sqrt{R_{IN} Z_0}. \tag{7.14}$$

In WNPT systems, R_{IN} is often a low value due to weak mutual coupling (low M). Thus, the characteristic impedance Z_A of the feedline must be relatively low. Moreover, in the next section it will be shown that decreasing the value of characteristic impedance Z_A well below this bound results in decreasing electrical lengths βl from (7.9). For this reason, low-impedance transmission lines are used to design the self-matched loop resonators presented in this chapter.

7.3.2 Parameter Trends

Figure 7.4 provides some insight into how Z_A, X_{IN}, and βl behave as a function of the system parameters. Figure 7.4(a) shows that the electrical length βl of the feedline must increase as R_{IN} decreases. This can be shown mathematically by taking the partial derivative of (7.9) with respect to R_{IN}. Recall from (7.12) that R_{IN} decreases as the matching distance decreases.

Similarly, it can be shown that $\frac{\delta \beta l}{\delta X_{IN}} \geq 0$ and $\frac{\delta X_{IN}}{\delta Z_A} \geq 0$. By combining these two partial

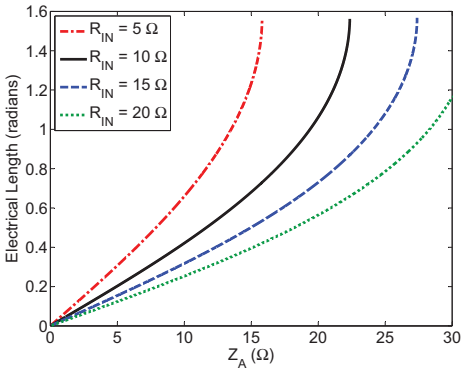

(a) A plot of the required electrical length βl of the feedline as a function of Z_A. Here, $Z_0 = 50\,\Omega$. Curves are provided for the cases $R_{IN} = 5\,\Omega, 10\,\Omega, 15\,\Omega$, and $20\,\Omega$. Clearly, βl increases with increasing Z_A.

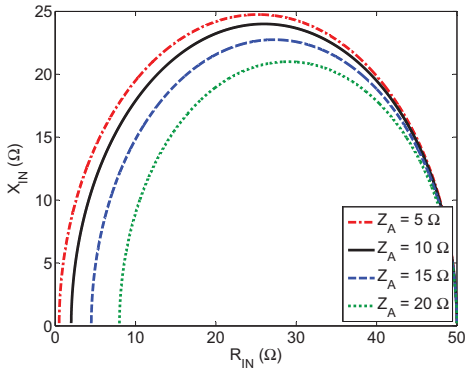

(b) A plot of the reactance X_{IN} presented by the feedline as a function of R_{IN}. Here, $Z_0 = 50\,\Omega$. Curves are provided for the cases $Z_A = 5\,\Omega, 10\,\Omega, 15\,\Omega$, and $20\,\Omega$.

Figure 7.4 A family of curves generated by equations (7.9) and (7.13). These curves provide an insight into the design of the self-matched WNPT system.

derivatives, it is clear that the required electrical length of the feedline will decrease with decreasing characteristic impedance Z_A:

$$\frac{\delta \beta l}{\delta Z_A} \leq 0. \tag{7.15}$$

A more detailed behavior of βl vs. Z_A is shown in Figure 7.4(a). Note that low values of Z_A result in short electrical lengths βl. This is the motivation behind using low-impedance transmission lines in the designs.

The behavior of the reactance X_{IN} presented by the feedline as a function of R_{IN} is given in 7.4(b).

7.4 Design Variables

In Section 7.3, design equations were derived to relate Z_A, βl, and C to the fixed parameters of the system. The conclusions were that three variables are used to design the impedance match: Z_A, C, and βl. One of these variables can be chosen and the other two solved for. In this section, a design procedure in which Z_A is fixed is presented along with a detailed analysis of the design variables. The design procedure is as follows:

1. Choose the operating frequency f.
2. Establish the port impedances Z_0, e.g. set $Z_0 = 50\,\Omega$.
3. Choose the transmission line type.

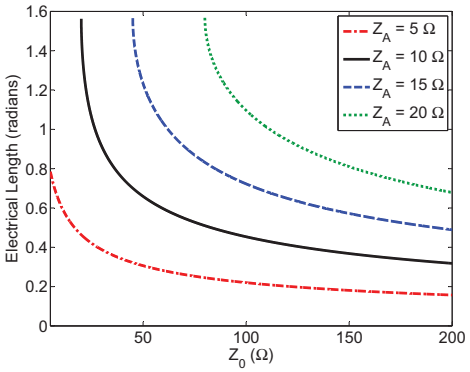

(a) A plot of the required electrical length βl for the feedline as a function of Z_0. Here, $R_{IN} = 5\ \Omega$. Curves are provided for the cases $Z_A = 5\ \Omega, 10\ \Omega, 15\ \Omega$, and $20\ \Omega$. These curves show that changing the characteristic impedance Z_0 of the ports changes the required electrical length βl of the feedline.

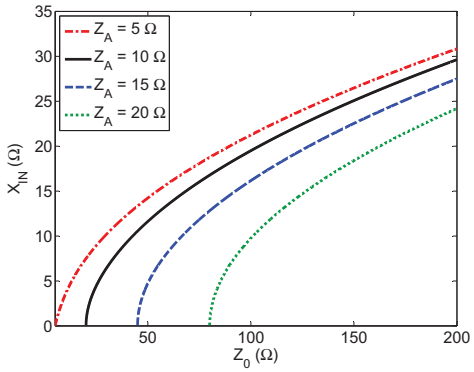

(b) A plot the reactance X_{IN} presented by the feedline as a function of Z_0. Here, $R_{IN} = 5\ \Omega$. Curves are provided for the cases $Z_A = 5\ \Omega, 10\ \Omega, 15\ \Omega$, and $20\ \Omega$. These curves show that changing the characteristic impedance Z_0 of the ports changes the required reactance X_{IN} presented by the feedline.

Figure 7.5 A family of curves generated by equations (7.9) and (7.13). These curves provide an insight into the design of the self-matched WNPT system.

4. Choose the dielectric substrate.
5. Choose a ground conductor width b (see Fig. 7.1(b)).
6. Choose a coupling distance for the impedance match.
7. Estimate the total loop inductance L and the mutual inductance M.
8. Using (7.12), estimate R_{IN}.
9. Choose the feedline conductor width W_{FEED}.
10. Calculate Z_A for the transmission line. In this chapter, this is done using the full-wave electromagnetic solver Ansys HFSS.
11. Solve for X_{IN} using (7.13).
12. Solve for the capacitance C using (7.10).
13. Choose the signal conductor width W_{CAP} for the capacitive stub.
14. Solve for the required length of the capacitive stub to achieve C.
15. Solve for βl of the feedline using (7.9).
16. Simulate and adjust parameters if necessary.

In the following sections, considerations for establishing the parameters (e.g. frequency) of the system are provided.

7.4.1 Operating Frequency

The operating frequency for a self-matched loop resonator system is limited by the radius of the loop. Indeed, the circumference of the loop must be long enough to incorporate the required low-impedance feedline and capacitive stub. This becomes easier at higher frequencies. For the design in this chapter, a frequency of 38 MHz was chosen. This is the same frequency used in [20].

Other considerations for the operating frequency of the WNPT system should also be taken, such as frequency allocation and constraints on allowable field levels versus frequency (see [96]).

7.4.2 Choosing the Dielectric

The input impedance Z_{cap} of the capacitive stub is given by (see Chapter 6):

$$Z_{cap} \approx \frac{1}{l(G' + j\omega C')}, \tag{7.16}$$

where l is the physical length of the capacitive stub, G' is the per-unit-length conductance, and C' is the per-unit-length capacitance. The following microstrip formulas are provided in Chapter 6:

$$C' = \frac{\sqrt{\epsilon_{eff}}}{cZ_0}, \tag{7.17a}$$

$$G' = \frac{k_0\sqrt{\epsilon_{eff}}\tan\delta_{eff}}{Z_0}, \tag{7.17b}$$

where ϵ_{eff} and $\tan\delta_{eff}$ are the effective permittivity and effective loss tangents of the transmission line, respectively. The subscript eff is used since electric fields exist in both air and the dielectric for microstrip lines. For stripline transmission lines, $\epsilon_{eff} = \epsilon_R$, where ϵ_R is the permittivity of the dielectric.

For a fixed capacitance $C = C'l$, the total conductance $G = G'l$ can be found using (7.17a) and (7.17b):

$$G = G'l = \omega C \tan\delta_{eff}. \tag{7.18}$$

For a fixed reactance $1/(\omega C)$ of the capacitive stub, the conductance is proportional to $\tan\delta_{eff}$. Therefore, to minimize the loss in the capacitive stub, $\tan\delta_{eff}$ should be minimized.

However, one should also appreciate the benefits of a substrate with a high dielectric constant. For a given dielectric height and signal trace width, lower values of Z_A are achievable. From Figure 7.4(a), this leads to shorter feedline lengths βl. Moreover, higher

dielectric constants increase β, which further reduces physical line lengths l. The designs for this chapter use a Rogers RT/Duroid 5880 substrate, which has a low permittivity and loss tangent.

7.4.3 Transmission Line Type

The type of transmission line, e.g. microstrip or stripline, should also be considered during the design process, as in Chapter 6. A few considerations to consider are:

- Effects of nearby dielectics
- Losses
- Ease of matching
- Fabrication
- Cost

In this chapter, microstrip lines are employed due to their simplicity of fabrication. Moreover, a microstrip line has lower dielectric losses than a stripline since the fields partially exist in air. However, this also means that the microstrip line is more susceptible than stripline to detuning by surrounding objects. The per-unit-length capacitance of the microstrip is also lower than that of the stripline, which results in higher characteristic impedances Z_A for the feedline. This results in longer electrical lengths βl, as shown in Figure 7.4(a).

7.4.4 Line Impedance

From (7.15), decreasing the impedance Z_A of the feedline will decrease the electrical length βl required for an impedance match. Therefore, a low Z_A is desirable. However, realizing low impedance transmission lines may require wide signal traces or thin dielectrics. Therefore, the impedance Z_A of the feedline has a lower bound. The designs in this chapter use a 254 μm dielectric thickness (a), 15 mm width (W), and relative permittivity of 2.2 for the microstrip feedline to yield a characteristic impedance of approximately 3.85 Ω. These values were chosen after simulating several different combinations of dielectric thickness and signal widths.

7.4.5 System Impedance Z_0

Figure 7.5 plots the behavior of βl and X_{IN} (using (7.9) and (7.13)) as a function of the system impedance Z_0. These curves show that changing Z_0 changes the required reactance

X_{IN} presented by the feedline, as well as its electrical length βl. Doing so may reduce loss by shortening the length of the capacitive stub. However, the designs in this chapter assume $Z_0 = 50\,\Omega$.

7.4.6 Mechanical Considerations

Mechanical stability associated with the planar loop resonator should also be considered. To construct low-impedance transmission lines, thin dielectrics are advantageous since they result in high per-unit-length capacitances C' and low per-unit-length inductances L' [39]. This results in low characteristic impedances Z_A ($Z_A = \sqrt{L'/C'}$). However, for stand-alone loop resonators, the mechanical stability inherent with thicker dielectrics should be considered. For the designs in this chapter, the 254 μm dielectric thickness was found to be sufficient.

7.5 Simulation and Experimental Results

Two different pairs of resonators are designed and fabricated in this section. The first pair (Design 1) is designed to achieve a full 2-port impedance match at a coupling distance of 15 cm. The second pair (Design 2) is designed for an impedance match at 20 cm. Although higher efficiencies could be achieved with smaller matching distances, these distances were chosen to demonstrate the feasibility of self-matched systems for even these weaker mutual inductances values. Given the discussion presented in Section 7.4, the following parameters of the loops were established:

- Operating Frequency (f) = 38 MHz
- Loop Radius (r) = 9 cm
- Height (a) = 254 μm
- Signal Width (W) = 15 mm
- Ground Width (b) = 20 mm
- Dielectric: Rogers RT/Duroid 5880
- Relative Permittivity (ϵ_R) = 2.2
- Loss Tangent ($\tan\delta$) = 0.009
- Conductor: copper (σ = 5.8e7 S/m)
- Conductor Thickness (t) = 70 μm

Figure 7.1(b) labels the dimensions of the loop cross-section for reference. As mentioned in Section 7.2, the width of the capacitive stub can differ from the width of the feedline. However, in this chapter, the low-impedance feedline and the capacitive stub both use a signal width (W) of 15 mm for simplicity.

7.5.1 The Designs

Having established the aforementioned parameters, prescribing a desired coupling distance for a 2-port impedance match will determine the remaining two variables of the system: the length of the feedline and the length of the capacitive stub. To solve for the two unknown lengths, the self-inductance L of the loops and the mutual inductance M at both distances must be estimated, as mentioned in Section 7.4. In Chapter 6, the self-inductance L for planar loop resonators is approximated by combining the formula for the self-inductance of a loop [91] of circular cross section and a relationship between rectangular and circular cross sections. In this way, the self-inductance of these 9 cm loops is estimated to be $L \approx 364$ nH. To estimate the mutual inductance, the formula presented in [20] for filamentary currents is used.

The characteristic impedance of the feedline is estimated to be $Z_A \approx 3.85\Omega$ using the full-wave electromagnetic solver Ansys HFSS. The electrical length of the feedline βl and the input reactance X_{IN} can be found using (7.9) and (7.13), respectively. The capacitance C can be calculated from X_{IN} using (7.10). Equation (7.12) is used to approximate R_{IN}.

HFSS can be used to find the effective permittivity ϵ_{eff} of the microstrip line (and therefore β). The required physical feedline length l can then be determined. The physical length l_{CAP} of the capacitive stub is approximated by $l_{CAP} = C/C'$, where C' is the per-unit length capacitance given by:

$$C' = \frac{\sqrt{\epsilon_{eff}}}{cZ_A}. \tag{7.19}$$

Here, c is the speed of light in a vacuum.

7.5.2 Full-Wave Simulation: Parameter Adjustments

After using the physical parameters provided in Table 7.1 in the full-wave simulation of the structure, one finds that the resulting operating frequency and impedance-matched distance differ slightly from the intended values. This is due to the approximations made when calculating L and M. Therefore, the parameters must be adjusted after performing an initial full-wave simulation.

Using the trends provided in Section 7.3.2, the parameters were adjusted appropriately. For example, recall that $\frac{\delta\beta l}{\delta R_{IN}} \leq 0$ and $R_{IN} \approx \omega M$. Therefore, if the simulated impedance-

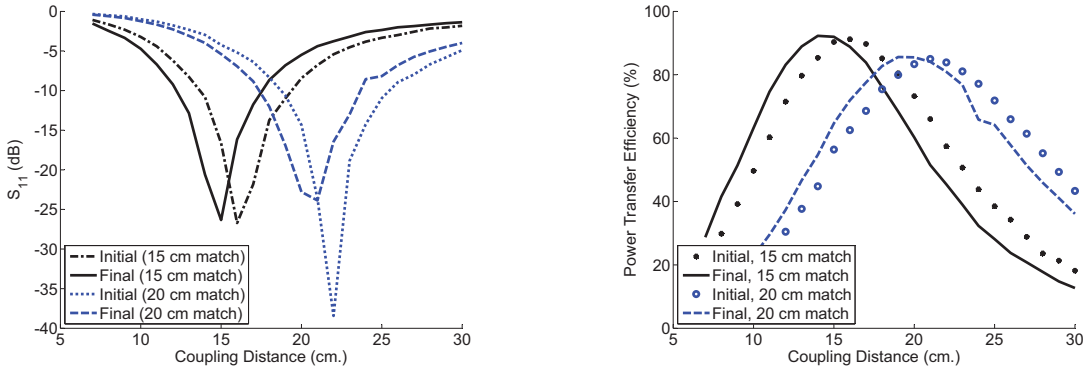

(a) Input reflection coefficient S_{11}.

(b) Power transfer efficiency $|S_{21}|^2$.

Figure 7.6 Simulations for the initial and final designs at their respective operating frequencies. The operating frequencies of the initial, pre-tuned designs were simulated to be 41.2 MHz for both Design 1 and Design 2. The operating frequencies of the final, adjusted designs were simulated to be 38 MHz for both Design 1 and Design 2.

Table 7.1 Approximate system parameters

	Design 1	Design 2
Impedance-Matched Distance (cm)	15 cm	20 cm
f	38 MHz	38 MHz
L	364 nH	364 nH
Z_A	3.85 Ω	3.85 Ω
ϵ_{eff}	2.13	2.13
M	18.6 nH	10.1 nH
Z_{IN}	4.44 + j13.74Ω	2.42 + j10.03Ω
βl @ 38 MHz	14.3°	20.1°
l	21.5 cm	30.2 cm
C	57.2 pF	54.4 pF
l_{CAP}	4.53 cm	4.31 cm

Table 7.2 Final system parameters

	Design 1	Design 2
Impedance-Matched Distance (cm)	15 cm	20 cm
l	20.2 cm	32.2 cm
l_{CAP}	5.09 cm	5.12 cm

matched distance is too close, then the electrical length βl should be increased. Similarly, if the simulated operating frequency is too high, then the capacitance C should be increased. This process quickly results in the adjusted lengths given in Table 7.2. The lengths were measured at the middle of the copper traces printed on the loop. From Table 7.2, it is clear that the adjusted lengths are close to those given in Table 7.1.

Table 7.3 Equivalent Circuit parameters

	Design 1	Design 2
βl @ 38 MHz	13.5°	21.3°
R	0.156 Ω	0.183 Ω
L	343 nH	376 nH
C	61.0 pF	52.4 pF
Q @ 38 MHz	525	491
M	19.2 nH	10.9 nH

Figure 7.6(a) shows the input reflection coefficient S_{11} for the initial and final designs at their respective operating frequencies. The operating frequencies of the initial, pre-tuned designs were simulated to be 41.2 MHz for both Design 1 and Design 2. The operating frequencies of the final, adjusted designs were simulated to be 38 MHz for both Design 1 and Design 2. From the figure, the impedance-matched distances for the initial designs were slightly larger than desired. Figure 7.6(b) shows the simulated power transfer efficiency for the initial and final designs. From simulation, power dissipated in the conductors and dielectric accounted for 7.7% and 13.8% of the power loss for Designs 1 and 2, respectively. Radiative losses were very small, accounting for only 0.17% and 0.33% of the power loss, respectively. The remaining losses were due to slight impedance mismatches.

Figure 7.7 shows a simulation of the surface currents on the source loop of Design 1 for an incident power of 1 Watt. The figure verifies the current behavior described in Figure 7.1(a).

Using the procedure described in Chapter 6, the loop parameters were extracted and are given in Table 7.3. The mutual inductance M was extracted by curve fitting. Figure 7.8 plots the input impedance of the coupled loop system for the circuit model and the simulated structure. The figure shows that the circuit model agrees well with the simulated structure.

7.5.3 Full-Wave Simulation: Frequency Limitations

As discussed in Section 7.4, the circumference of the loop constrains the operating frequency to values high enough to allow realizable electrical lengths and capacitive stubs. In this chapter, a frequency of 38 MHz is employed. However, for the same loop geometry at a coupling distance of 15 cm, it can be shown through full-wave simulation that design frequencies as low as 26 MHz result in feedlines and stubs that fit onto the circumference of the 9 cm loop.

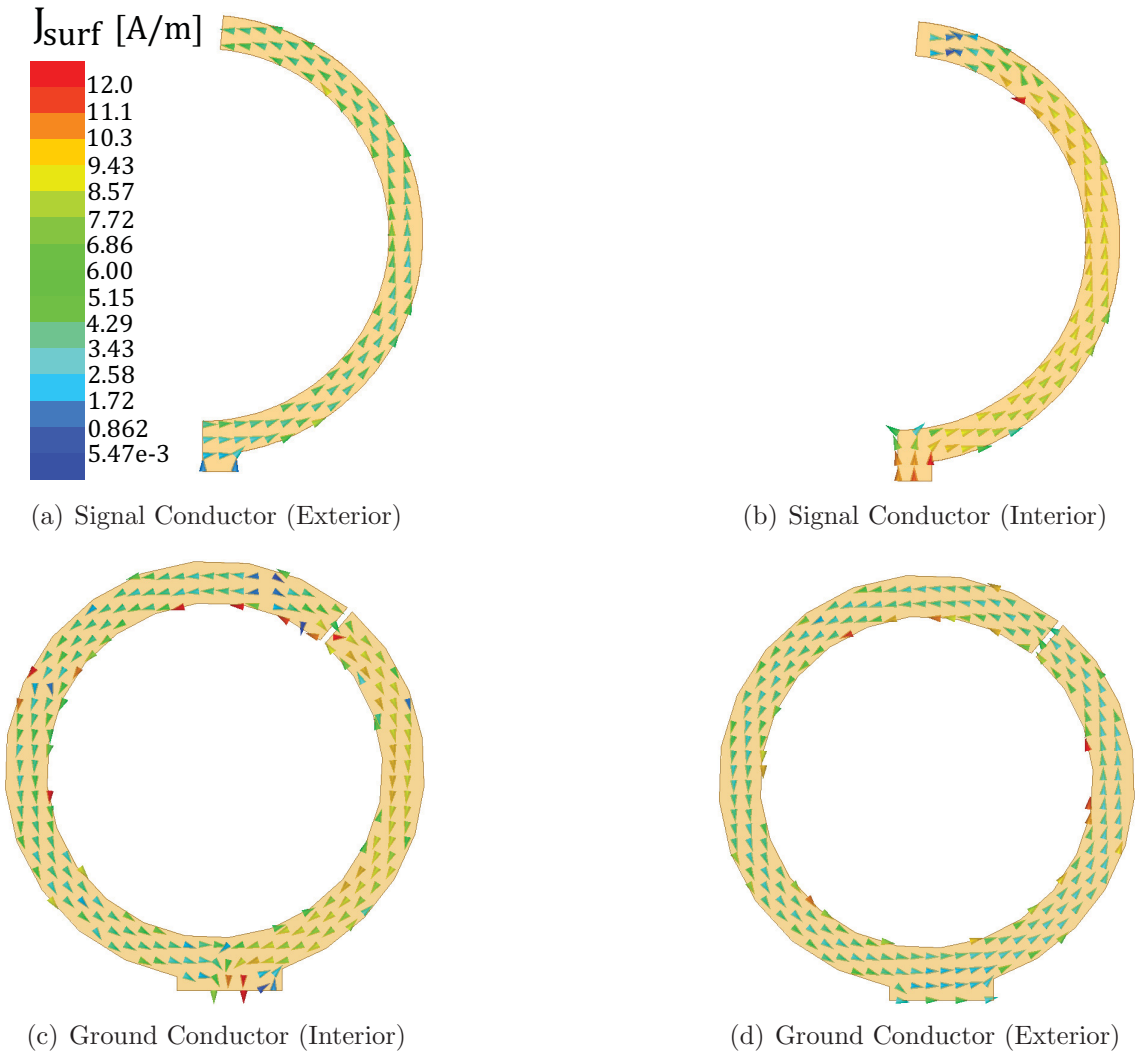

(a) Signal Conductor (Exterior)

(b) Signal Conductor (Interior)

(c) Ground Conductor (Interior)

(d) Ground Conductor (Exterior)

Figure 7.7 Full-wave HFSS simulation of the surface currents residing on the source loop of Design 1 for a coupling distance of 15 cm and an incident power of 1 Watt. The simulation verifies the current behavior depicted in Figure 7.1(a). The net current flows in the counter-clockwise direction, but interior currents on the ground conductor directly beneath the signal conductor flow in the clockwise direction. Exterior currents flow in the counter-clockwise direction for both conductors.

7.5.4 Final Design

The final loop designs were fabricated using an in-house milling machine. The prototypes are shown in Figure 7.9. The width of the slit in the ground conductor is 3 mm. An additional trace of copper is used to mechanically support the thin loop, as shown in the figure. Through HFSS simulations, it can be shown that this trace has negligible effect on the system behavior.

Measurements of the 2-port S-parameters for both designs were taken using a vector network analyzer (VNA). The loop-to-loop efficiency ($|S_{21}|^2$) results are given in Figure

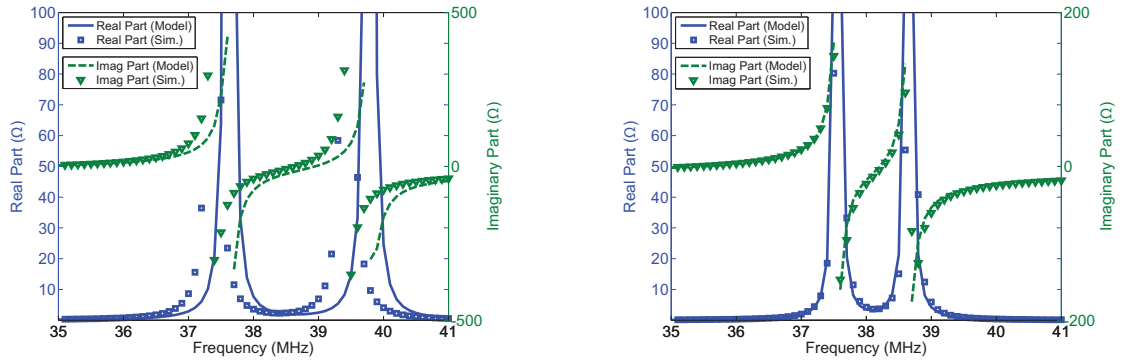

(a) Design 1 (b) Design 2

Figure 7.8 Comparison of the input impedance Z'_{IN} for the simulated structure and its circuit model (see Figure 7.2(b) and Table 7.3).

Table 7.4 Efficiency Comparisons

	This work	[20]	[19]	[97]	[98]	[18]	[99]
Freq. (MHz)	**38**	38	7.95	1.072	13	15.9	3.7
Radius (r) (cm)	**9**	10.7	29.5	9	1.85	15	17
# of turns (N)	**1**	1	6	2	10	5	3
Reported Efficiencies							
	91%@1.67r	83%@1.67r	-	87%@1.67r	77.7%@1r	95%@1.33r	95%@1.76r
	85%@2.22r	71%@2.22r	67%@2.2r	-	-	-	-

7.11. The Figure includes measurements at the even and odd modes for frequency tuning (see Section 7.2.3). Inspection of Figure 7.11(a) shows that the system efficiency can be dramatically improved using the frequency tuning. This is consistent with the analysis presented in [95]. Frequency tuning is used in the strong coupling regime, which is given by [95]:

$$(\omega M)^2 > (R + R_S)^2. \tag{7.20}$$

The measured power transfer efficiency at the matching distances for Designs 1 and 2 are 91% and 85%, respectively. The reflection coefficients at the loop are given in Figure 7.12 and show that the ports are well-matched.

A comparison of loop-to-loop efficiencies with a sample of other WNPT systems is given in Table 7.4. The table shows the self-matched resonators presented in this chapter perform better than most of the reported systems. However, the primary advantages of these self-matched resonators are the compactness, planarity, and the use of distributed elements. The other systems in Table 7.4 use non-planar copper coils that are not self-matched.

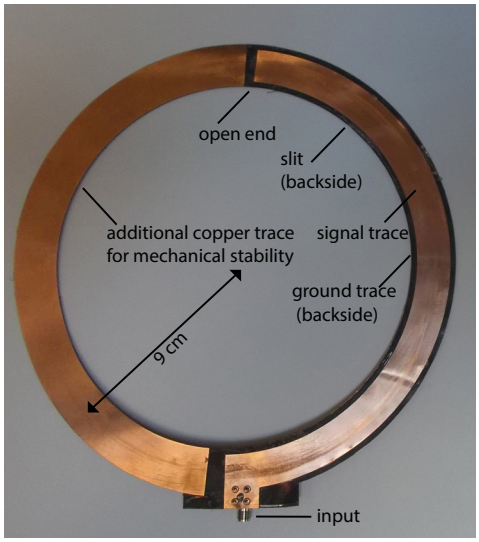

(a) Fabricated self-matched loop resonator using Design 1.

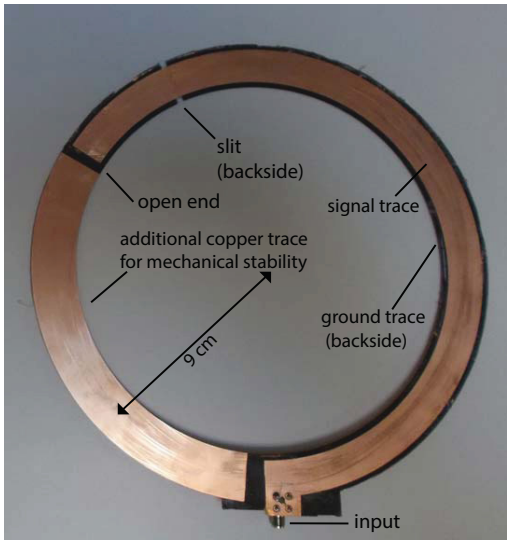

(b) Fabricated self-matched loop resonator using Design 2.

Figure 7.9 Fabricated self-matched microstrip loop resonators. Traces of copper were used to mechanically support the thin loops.

7.6 Chapter Summary

In this chapter, an impedance-matching technique for coupled, planar-loop resonators was proposed and implemented using low-impedance transmission lines and capacitive stubs. These distributed components were integrated into the planar resonators themselves. Two pairs of compact resonators with radius 9 cm were designed and fabricated. For the first design, 91% loop-to-loop power transfer efficiency was measured at its intended impedance-matched distance of 15 cm (1.67 radii). For the second design, 85% loop-to-loop power transfer efficiency was measured at its intended impedance-matched distance of 20 cm (2.22

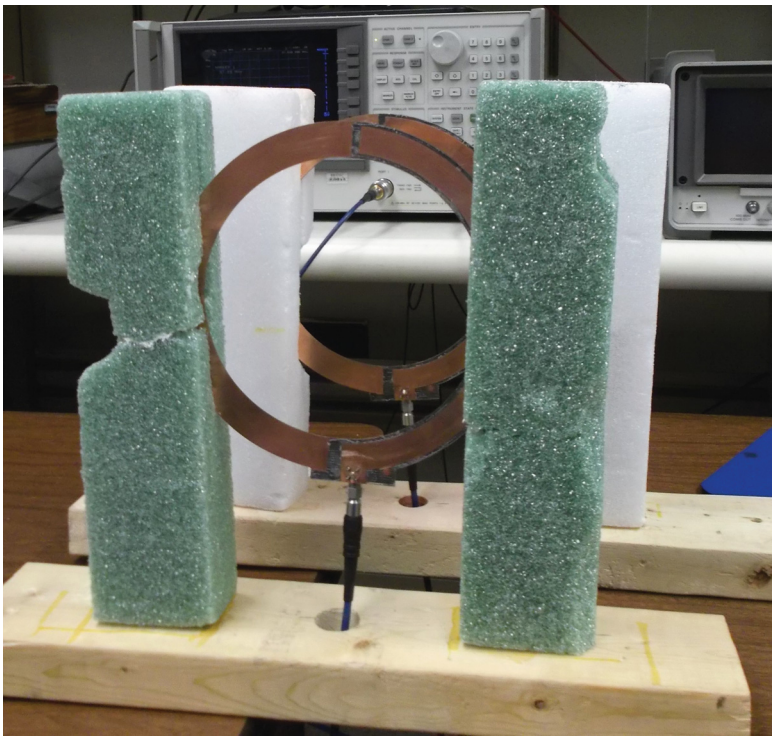

Figure 7.10 Measurement setup for the coupled loop system. Foam is used to hold the loops upright.

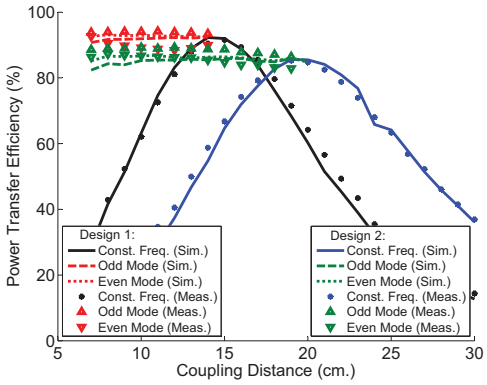

(a) Simulated and measured power transfer efficiency for the two loop designs. Both frequency-tuned and fixed-frequency efficiencies are provided.

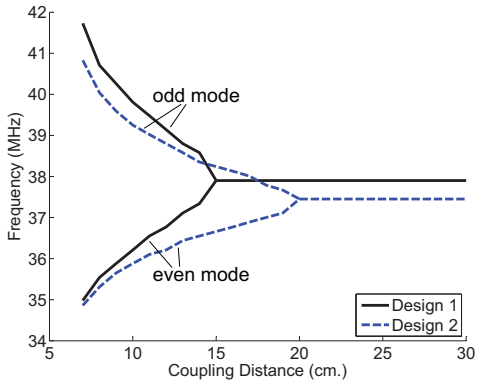

(b) Measured operating frequencies for the two frequency-tuned systems.

Figure 7.11 Simulation and measurement results for the two self-matched resonator designs.

radii). Using frequency tuning, high system efficiency was maintained in the strong coupling regime. This chapter demonstrates high-Q planar loops for wireless non-radiative power transfer (WNPT) systems without external matching networks.

The efficiencies for the WNPT resonators presented in this chapter are higher than

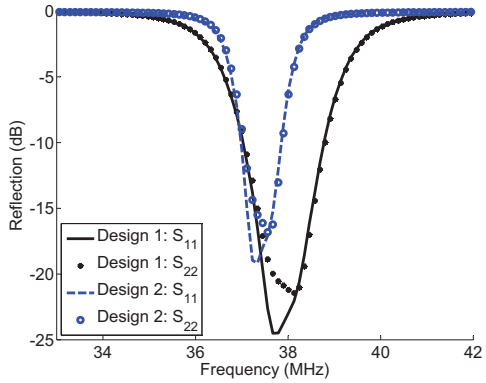

Figure 7.12 Measured input and output reflection coefficients for the pairs of loops at their coupling distances. For Design 1, the coupling distance is 15 cm. For Design 2, the coupling distance is 20 cm. The low reflections show that the resonators are well-matched at the intended coupling distances.

most of the reported loop-to-loop efficiencies presented in the literature. Nevertheless, efficiencies could be improved by replacing the dielectric of the system with air. However, the primary advantages of these resonators are the compactness, planarity, and use of distributed elements. These attributes are particularly advantageous for PCBs and ICs.

Future research directions include efficiency improvements using other types of dielectric, such as air, or by changing the characteristic impedance Z_0 of the system to values more representative of a practical load.

Chapter 8

Conclusion

8.1 Summary of Contributions

In this thesis, advances in emerging electromagnetics topics such as metamaterials and wireless power transfer were presented. There were three distinct topics: (1) pattern shaping using leaky-wave antennas, (2) the design of a compact, broadband, printed beamformer using constrained optimization techniques, and (3) the design of compact, high-Q, planar loop resonators for wireless non-radiative power transfer. A summary of contributions to the field of electromagnetics are provided here.

8.1.1 Pattern Shaping with Leaky-Wave Antennas

In Chapters 2 and 3, two leaky-wave, metamaterial impedance surfaces were explored for synthesizing arbitrary radiation patterns: (1) an impedance surface consisting of an inhomogeneous, anisotropic dielectric topped by an admittance sheet and (2) an impedance surface consisting of cascaded, electric admittance sheets separated by dielectric layers. Eigenmode analysis was presented for each topology using either a transverse resonance technique or a full-field approach.

A modified Orchard-Elliott technique was introduced for calculating the required aperture field. This method overcomes the deficiencies of the geometrical optics approximation, used in earlier works to design such antennas, by using an efficient gradient search method. Moreover, it avoids cumbersome methods requiring iterative FFTs.

Several different antenna designs were presented and simulated using the commercial full-wave solver COMSOL Multiphysics. The results showed excellent agreement with the prescribed goals. In particular, high-fidelity control of the far-field magnitude and polarization were demonstrated.

8.1.2 Design of a Compact, Broadband, Printed Beamformer

Chapters 4 and 5 introduce an alternative to coordinate-transformation techniques for designing exotic metamaterial transformation devices. The technique consists of a custom finite-element method (FEM) solver coupled with a constrained nonlinear minimization algorithm. The proposed procedure has two primary advantages over coordinate-transformation methods: (1) it can place constraints on material parameters to improve practicality and bandwidth and (2) it permits the design of devices for which a transformation map may be difficult/impossible to find, such as those with several prescribed outputs for specified inputs.

Chapter 4 presents the design of two different antenna beamformers: (1) a beamformer designed to transform each of 7 different stipulated inputs to an output beam at a different prescribed radiation angle and (2) a beamformer with 3 input/output pairs that each produce a flattop radiation pattern with 40° beamwidth at different angular ranges. Simulation results using the commercial full-wave solver COMSOL Multiphysics demonstrates excellent results compared to prescribed goals.

Chapter 5 details the implementation of the first beamformer design presented in Chapter 4. Printed tensor transmission-line metamaterials are employed to realize the inhomogeneous, anisotropic design. These unit cells are of low-pass topology, resulting in a broadband performance. Measurement results demonstrate good performance from 10 GHz to 13 GHz. In particular, the prescribed radiation angles are maintained between 10 GHz and 13 GHz while keeping sidelobe levels low.

8.1.3 Planar Resonators for Wireless Non-Radiative Power Transfer

Chapters 6 and 7 introduce the design of a compact, high-Q planar loop resonator topology for efficient inductive power transfer. Analytical models are developed to investigate the trends in efficiency.

Chapter 7 presents a method for tailoring the parameters of the loop resonator presented in Chapter 6 to achieve a 2-port impedance match at a prescribed coupling distance. The designs alleviate external matching requirements. Such a technique not only achieves high efficiency, but also a compact structure. Two different sets of loops are fabricated: one for a 2-port match at 15 cm and another for a 2-port match at 20 cm. Measurement results show coil-to-coil efficiencies of 91% and 85% for the two structures, respectively.

8.2 Future Work

The research presented in this thesis was performed to advance the state-of-the-art in metamaterials and wireless power transfer. However, as in all research, further improvements and advancements can be made. This section lists potential directions for future work on the presented topics.

8.2.1 Pattern Shaping with Leaky-Wave Antennas

Future work on pattern shaping using leaky-wave antennas may include the design and fabrication of a physical antenna realization. To do so, the effect of a finite antenna width on the performance would be investigated.

Future work may also include the extension of the theory to 2D leaky-wave metasurfaces. However, a synthesis technique other than the one-dimensional Orchard-Elliott method would need to be employed.

8.2.2 Design of a Compact, Broadband, Printed Beamformer

There are several opportunities for improvement in the beamformer design. For example, the dielectric substrate (Rogers RT/Duroid 5880) used in the design is relatively flexible. The choice of a more rigid substrate may help the measured performance.

Mitigation of the coupling effects at the input feedline could also be explored. In the printed-circuit design, this coupling degraded the beamformer performance from 8 GHz to 9.5 GHz. A reduction of feedline lengths and a redesign of the matching networks may improve the performance.

Future work may also include improvement of the radiation efficiency. One possibility would be to use a larger cell size, which would allow for larger conductive widths and therefore lower conductive losses. A redesign of the cell database may also yield a wider range of material parameters, which could reduce the amount of power exiting the sides of the transformation region.

The design of a beamformer that scans a wider angular range may also be explored. The redesign of the cell database to include a wider range of material parameters may help with this.

Finally, future investigations may include beamformer fabrication using low-loss, 3D-printed materials.

8.2.3 Planar Resonators for Wireless Non-Radiative Power Transfer

Possible improvements to the planar resonators used for wireless non-radiative power transfer may include the use of an air or styrofoam dielectric to achieve an even higher efficiency than was demonstrated, since the dielectric loss tangent would be lower.

Investigations may also include the use of an array of planar resonators to improve performance. In particular, such an array may be able to improve the coupling to the receiver loop.

8.3 List of Publications

The work reported in this thesis has been published in the following peer-reviewed journals and conference proceedings.

8.3.1 Journal Papers

1. **B. B. Tierney** and A. Grbic, "A Compact, Broadband Beamformer Designed Using Optimization," Manuscript in Preparation for IEEE Transactions on Antennas and Propagation, June 2016.
2. **B. B. Tierney** and A. Grbic, "Designing Anisotropic, Inhomogeneous Materials Through Optimization: An Alternative to Transformation Electromagnetics," Manuscript in Preparation for IEEE Transactions on Antennas and Propagation, June 2016.
3. **B. B. Tierney** and A. Grbic, "Controlling Leaky Waves for Tailored Electromagnetic Radiation Using Metasurfaces," Manuscript in Preparation, June 2016.
4. F. Elek, **B. B. Tierney** and A. Grbic, "Synthesis of tensor impedance surfaces to control phase and power flow of guided waves," IEEE Transactions on Antennas and Propagation, vol. 63, no. 9, pp. 3956-3962, Sept. 2015.
5. **B. B. Tierney** and A. Grbic, "Arbitrary beam shaping using 1-D impedance surfaces supporting leaky waves," IEEE Transactions on Antennas and Propagation, vol. 63, no. 6, pp. 2439-2448, June 2015.
6. **B. B. Tierney** and A. Grbic, "Planar shielded-loop resonators," IEEE Transactions on Antennas and Propagation, vol. 62, no. 6, pp. 3310-3320, June 2014.
7. **B. B. Tierney** and A. Grbic, "Design of self-matched planar loop resonators for wireless nonradiative power transfer," IEEE Transactions on Microwave Theory and

Techniques, vol. 62, no. 4, pp. 909-919, April 2014.

8.3.2 Conference Proceedings

1. **B. B. Tierney** and A. Grbic, "Design of a Printed, Metamaterial-Based Beamformer," Submitted to International Symposium on Antennas and Propagation, pp. 1-2, Okinawa, Japan, October 24-28, 2016.
2. **B. B. Tierney** and A. Grbic, "Antenna aperture synthesis using cascaded sheet admittances," IEEE International Symposium on Antennas and Propagation, pp. 1-2, Fajardo, Puerto Rico, June 26 - July 1, 2016.
3. **B. B. Tierney** and A. Grbic, "Optimization as an Alternative to Transformation Optics," 10th European Conference on Antennas and Propagation, pp. 1-2, Davos, Switzerland, April 10-15, 2016.
4. **B. B. Tierney** and A. Grbic, "Antenna aperture synthesis using cascaded sheet admittances," International Conference on Metamaterials, Photonic Crystals, and Plasmonics, pp. 1-2, New York City, NY, August 4-7, 2015.
5. **B. B. Tierney** and A. Grbic, "Leaky-wave eigenmodes for arbitrary electromagnetic wavefronts," IEEE International Symposium on Antennas and Propagation, pp. 1-2, Vancouver, BC, Canada, July 19-24, 2015.
6. **B. B. Tierney** and A. Grbic, "Radiation pattern synthesis using impedance surfaces supporting leaky waves," URSI General Assembly and Scientific Symposium, pp. 1-4, Beijing, China, Aug. 16-23, 2014.
7. **B. B. Tierney** and A. Grbic, "Tailoring leaky-wave radiation with impedance surfaces," IEEE International Symposium on Antennas and Propagation, pp. 1-2, Memphis, TN, July 6-11, 2014.
8. **B. B. Tierney** and A. Grbic, "Planar shielded-loop resonators for wireless non-radiative power transfer," IEEE International Symposium on Antennas and Propagation, pp. 1-2, Orlando, FL, July 7-13, 2013.

Appendices

Appendix A
FEM Functional

This appendix presents the derivation of the Ritz functional featured in (4.2). Consider a boundary value problem over a domain Ω with boundary $\delta\Omega$ governed by the following differential equation:

$$\mathcal{L}\Phi = f. \tag{A.1}$$

If $\mathcal{L}$ is self-adjoint under Dirichlet boundary conditions, i.e. $\langle \mathcal{L}\Phi, \Psi\rangle = \langle \Phi, \mathcal{L}\Psi\rangle$, then the solution to the boundary value problem can be found by finding a stationary point of the functional $F(\Phi)$ [62]:

$$\begin{aligned} F(\Phi) = \frac{1}{2}\langle \mathcal{L}\Phi, \Phi\rangle - \frac{1}{2}\langle \Phi, f\rangle - \frac{1}{2}\langle f, \Phi\rangle \ldots \\ -\frac{1}{2}\langle \mathcal{L}\Phi, u\rangle + \frac{1}{2}\langle \Phi, \mathcal{L}u\rangle, \end{aligned} \tag{A.2}$$

where u is any function that satisfies the boundary conditions on the boundary $\delta\Omega$.

Consider the 2D inhomogeneous problem with $\vec{E} = E_z\hat{z}$ and a $\hat{z}$-directed current line source at $\mathbf{r}'$:

$$\nabla \times E_z\hat{z} = -j\omega\mu_0\bar{\mu_r}\vec{H}, \tag{A.3a}$$

$$\nabla \times \vec{H} = j\omega\epsilon_0\epsilon_{rz}E_z\hat{z} + \delta(\mathbf{r}-\mathbf{r}')I\hat{z}. \tag{A.3b}$$

Multiplying (A.3a) by $\bar{\nu_r} = {\bar{\mu_r}}^{-1}$ and applying the curl operator results in

$$\nabla \times [\bar{\nu_r}\nabla \times E_z\hat{z}] - k_0^2\epsilon_{rz}E_z\hat{z} = -j\omega\mu_0\delta(\mathbf{r}-\mathbf{r}')I\hat{z}. \tag{A.4}$$

The differential equation is of the form of (A.1) with the operator $\mathcal{L}$ equal to

$$\mathcal{L} = \nabla \times [\bar{\nu_r}\nabla\times] - k_0^2\epsilon_{rz}. \tag{A.5}$$

It can be shown that the operator $\mathcal{L}$ is self-adjoint for Dirichlet boundary conditions [62]. Consider a homogenous section Ω_i of the inhomogenous domain Ω and employ the inner product given by:

$$\langle \vec{a}, \vec{b} \rangle = \int_{\Omega_i} (\vec{a} \cdot \vec{b}) dS. \tag{A.6}$$

From (A.2), the functional over Ω_i is given by:

$$\begin{aligned} F_i(E_z) = \frac{1}{2} \int_{\Omega_i} \left(\nabla \times [\bar{\nu_{ir}} \nabla \times E_z \hat{z}] \cdot E_z \hat{z} - k_0^2 \epsilon_{irz} E_z^2 \right) dS + \ldots \\ \int_{\Omega_i} j\omega\mu_0 I E_z \delta(\mathbf{r} - \mathbf{r}') dS + \ldots \\ -\frac{1}{2} \int_{\Omega_i} (\nabla \times [\bar{\nu_{ir}} \nabla \times E_z \hat{z}] \cdot u \hat{z}) \, dS + \ldots \\ \frac{1}{2} \int_{\Omega_i} (\nabla \times [\bar{\nu_{ir}} \nabla \times u \hat{z}] \cdot E_z \hat{z}) \, dS. \end{aligned} \tag{A.7}$$

This equation can be simplified by applying the identity $(\vec{a} \times \vec{b}) \cdot \vec{c} = -(\vec{c} \times \vec{b}) \cdot \vec{a}$, setting $E_z = u$ on the boundary $\delta\Omega_i$, and employing Green's first vector identity,

$$\begin{aligned} \iiint_{\Omega_i} \left[(\nabla \times \vec{a}) \cdot \bar{\nu} (\nabla \times \vec{b}) - \vec{a} \cdot \nabla \times \left[\bar{\nu} (\nabla \times \vec{b}) \right] \right] dV = \\ \oiint_{\delta\Omega_i} \left[\vec{a} \times [\bar{\nu} (\nabla \times \vec{b})] \right] \cdot \hat{n} dS. \end{aligned} \tag{A.8}$$

The resulting functional is

$$\begin{aligned} F_i(E_z) = \frac{1}{2} \int_{\Omega_i} \left((\nabla \times E_z \hat{z}) \cdot \bar{\nu_{ir}} (\nabla \times E_z \hat{z}) - k_0^2 \epsilon_{irz} E_z^2 \right) dS + \ldots \\ \int_{\Omega_i} j\omega\mu_0 I E_z \delta(\mathbf{r} - \mathbf{r}') dS + \frac{1}{2} \int_{\delta\Omega_i} \hat{n} \times [\bar{\nu_{ir}} (\nabla \times E_z \hat{z})] \cdot E_z \hat{z} dS. \end{aligned} \tag{A.9}$$

We must find a stationary point of $F_i(E_z)$ in each homogeneous subdomain of the inhomogeneous problem. This can be accomplished simply by first summing together all $F_i(E_z)$ and then finding the stationary point of the resulting functional. By enforcing continuity of the tangential magnetic field, the boundary integrals around each cell Ω_i will cancel with the integrals from adjacent cells. Indeed, $\hat{n} \times \vec{H} = \hat{n} \times [\bar{\nu_{ir}} (\nabla \times E_z \hat{z})]$ must be continuous and E_z is assumed continuous. Only the integral along the outer boundary of the entire domain remains. Assuming some absorbing boundary condition on $\delta\Omega$, the resulting functional becomes:

$$F(E_z) = \frac{1}{2}\int_\Omega \left((\nabla \times E_z\hat{z}) \cdot \bar{\nu_r}(\nabla \times E_z\hat{z}) - k_0^2\epsilon_{rz}E_z^2\right) dS + \ldots$$
$$\int_\Omega j\omega\mu_0 I E_z \delta(\mathbf{r} - \mathbf{r}')dS + \frac{1}{2}\int_{\delta\Omega} \hat{n} \times (\nabla \times u\hat{z}) \cdot E_z\hat{z}d\Gamma, \tag{A.10}$$

where u satisfies the absorbing boundary condition on the outer boundary.

Appendix B

Spatial Cost Function Derivation

In this appendix, a detailed development of the spatial cost function provided in (4.11) is presented.

B.0.3 An Abstract Problem

To gain insight into (4.11), an abstract problem is considered first. The problem is the following: to find a vector $\mathbf{g}$ yielding the largest $||a(x,\mathbf{g})||^2$ for which $a(x,\mathbf{g}) = \alpha b(x)$, $\alpha \in \mathbb{C}$. Here, $a(x,\mathbf{g})$ and $b(x)$ are abstract functions with no physical meaning. A proposed solution to the problem is to solve the following optimization problem:

$$\underset{\mathbf{g}}{\text{minimize}} \quad s(\mathbf{g}) = 1 - \frac{|a(x,\mathbf{g}) \cdot b(x)^*|^2}{||b(x)||^4}. \tag{B.1}$$

The cost function is written using an inner product, which is defined in (4.12). The inner product is employed because it is a natural measure of similarity between two vectors. For example, this is the basis of matched filters [100].

The Cauchy-Schwarz inequality [101] can be used to show that, under certain conditions, solving (B.1) is equivalent to achieving the desired goal of finding a vector $\mathbf{g}$ yielding the largest $||a(x,\mathbf{g})||^2$ for which $a(x,\mathbf{g}) = \alpha b(x)$, $\alpha \in \mathbb{C}$. To see this, first recall that by the Cauchy-Schwarz inequality

$$a(x,\mathbf{g}) \cdot b(x)^* \leq ||a(x,\mathbf{g})|| \cdot ||b(x)||, \tag{B.2}$$

and therefore

$$s(\mathbf{g}) \geq 1 - \frac{(||a(x,\mathbf{g})|| \cdot ||b(x)||)^2}{||b(x)||^4} = 1 - \frac{||a(x,\mathbf{g})||^2}{||b(x)||^2}. \tag{B.3}$$

It is well known that Eq. (B.3) becomes an equality if and only if $a(x,\mathbf{g}) = \alpha b(x)$, for some $\alpha \in \mathbb{C}$ [101]. Now, let

$$\chi = \sup\{||a(x,\mathbf{g})||^2\} < \infty. \tag{B.4}$$

If there exists a feasible $\mathbf{g}$ satisfying the condition

$$a(x, \mathbf{g}) = \alpha b(x), \quad |\alpha| = \sqrt{\frac{\chi}{||b(x)||^2}}, \tag{B.5}$$

then $s(\mathbf{g})$ is minimized if and only if (B.5) is satisfied. In this case, solving problem (B.1) is equivalent to the original goal of finding a vector $\mathbf{g}$ yielding the largest $||a(x, \mathbf{g})||^2$ for which $a(x, \mathbf{g}) = \alpha b(x)$, $\alpha \in \mathbb{C}$. Therefore, we can simply employ well-established optimization algorithms to solve the problem.

B.0.4 Adaptation to Metamaterial Device Design

In this appendix, the aforementioned abstract problem is adapted to the design of metamaterial transformation devices. In particular, $a(x, \mathbf{g})$ represents the achieved output field and $b(x)$ represents the desired output field. However, two considerations are required for proper adaptation: 1) $||a(x, \mathbf{g})||^2$ and $||b(x)||^2$ should represent the output power and 2) the feasibility of (B.5) should be ensured. These considerations are discussed next.

B.0.5 Power Vector

The quantities $||a(x, \mathbf{g})||^2$ and $||b(x)||^2$ should represent output power. The output power density along the output aperture is written in terms of $E_z(x)$ as (see Appendix C):

$$P(x) = (1/2\omega\mu_0)\,\mathrm{Im}\{E_z(x)\partial E_z(x)^*/\partial y\}. \tag{B.6}$$

The unit vector $\hat{y}$ is normal to the output interface, as shown in Fig. 4.1. Under a local plane-wave approximation, $\partial E_z(x)^*/\partial y = jk_y(x)E_z(x)$ and

$$P(x) = \frac{k_y(x)}{2\omega\mu_0}|E_z(x)|^2. \tag{B.7}$$

A local radiation angle $\theta_r(x) = \cos^{-1}\frac{k_y(x)}{k}$ can be defined and the power density rewritten as

$$P(x) = \frac{\cos\theta_r(x)}{2\eta_0}|E_z(x)|^2. \tag{B.8}$$

The function $h(x)$ is now defined as:

$$h(x) = \sqrt{P(x)}\angle E_z(x) = \sqrt{\frac{\cos\theta_r(x)}{2\eta_0}}E_z(x). \tag{B.9}$$

Physically, the magnitude of $h(x)$ represents the square root of the output power density at x along the output interface, while its phase is equal to that of the electric field. The

function $h(x, \mathbf{g})$ is, in general, a function of the position along the output interface and the material coefficients, $\mathbf{g}$.

Since $||h(x, \mathbf{g})||^2$ represents output power, it is better suited for the cost function $s(\mathbf{g})$ than simply the output electric field. However, one additional modification is required, as explained next.

B.0.6 Nonlinear Scaling

Recall that condition (B.5) must be feasible to properly employ (B.1) as a solution. In the context of metamaterial device design, condition (B.5) physically means that there exists an achievable output $a(x, \mathbf{g})$ with power χ (the maximum achievable power) for which $a(x, \mathbf{g}) = \alpha b(x)$, $\alpha \in \mathbb{C}$. If this condition were not true, then some output profiles may minimize the cost function in (B.1), despite their incorrect shape, simply because $||a(x, \mathbf{g})||^2$ is large. Fortunately, the cost function can be modified to prevent this.

To reach a compromise between output power and field profile, a nonlinear scaling of $h(x, \mathbf{g})$ is introduced. In particular, consider the function k defined as:

$$k(h(x, \mathbf{g})) = h(x, \mathbf{g}) \cdot \min \left\{ 1, \beta \frac{||h_0(x)||}{||h(x, \mathbf{g})||} \right\}, \tag{B.10}$$

where the subscript 0 refers to the desired vector. For large output power $||h(x, \mathbf{g})||^2$, $||k(h(x, \mathbf{g}))||^2 = \beta^2 ||h_0(x)||^2$. For lower powers, $k(h(x, \mathbf{g})) = h(x, \mathbf{g})$. Therefore, $h(x, \mathbf{g})$ has been scaled by the function k to minimize the impact of its magnitude on the spatial cost function $s(\mathbf{g})$. This is achieved by the appropriate choice of β. The variable β offers a compromise between output power and desired profile. Ideally, β is chosen to be the highest value for which (B.5) is approximately feasible. For the beamformer prototype presented in Section 4.4, $\beta = 0.8$ and $||h_0(x)||^2$ equals the available input power.

Replacing $a(x, \mathbf{g})$ with $k(h(x, \mathbf{g}))$ and $b(x)$ with $k(h_0(x))$ in (B.1) results in the cost function given by (4.11). Note that a summation of the cost functions for each input q is employed in (4.11).

Appendix C

Power Expression

This appendix presents the derivation of expression (B.6). From Poynting's theorem:

$$\mathbf{S} = \mathbf{E} \times \mathbf{H}^*. \tag{C.1}$$

For the TE polarization discussed in Chapter 4, we have

$$\begin{aligned}
\mathbf{S} &= \frac{1}{-j\omega\mu_0} E_z \hat{z} \times (\nabla \times E_z^* \hat{z}), \\
\mathbf{S} &= \frac{1}{-j\omega\mu_0} E_z \hat{z} \times \left(\frac{\partial E_z^*}{\partial y} \hat{x} - \frac{\partial E_z^*}{\partial x} \hat{y} \right), \\
\mathbf{S} &= \frac{j}{\omega\mu_0} E_z \frac{\partial E_z^*}{\partial y} \hat{y} + \frac{j}{\omega\mu_0} E_z \frac{\partial E_z^*}{\partial x} \hat{x}.
\end{aligned} \tag{C.2}$$

The average output power density $P(x)$ is therefore given by

$$\begin{aligned}
P(x) &= \frac{1}{2} \operatorname{Re}\{S_y \hat{y}\}, \\
P(x) &= (1/2\omega\mu_0) \operatorname{Im}\{E_z(x) \partial E_z(x)^* / \partial y\}.
\end{aligned} \tag{C.3}$$

Appendix D

Effect of Feed line on Power Transfer Efficiency

D.0.7 Effective Resistance of the Feed line

Consider an RLC resonator with a length of lossy transmission line attached to the input (see Figure D.1(a)), representative of a shielded-loop resonator. The transmission line can be decomposed into a lossless transmission line and an effective series resistance R_{EFF} (see Figure D.1(b)). The resistance R_{EFF} can be determined by calculating the power P_{feed} dissipated in the feed line and dividing it by $|I_2|^2$ (defined in Figure D.1(b)):

$$R_{EFF} = \frac{2P_{feed}}{|I_2|^2}. \tag{D.1}$$

It can be shown that the effective resistance R_{EFF} will reach a minimum at a frequency near the resonance of the RLC circuit. The effective resistance R_{EFF} will increase as the excitation frequency is moved away from this minimum. This effect becomes more pronounced with longer transmission lines. For two magnetically-coupled RLC circuits (loops), the result is a decrease in maximum power transfer efficiency. This follows directly from the general equation for power transfer efficiency η' of the symmetric, coupled-loop system shown in Figure 6.3:

$$\eta' \triangleq \frac{P_{out}}{P_{source}} = \eta(1-|\Gamma|^2) = \frac{(1-|\Gamma|^2)R_L(\omega M)^2}{R[(R+R_L)^2+(\omega L-\frac{1}{\omega C}+X_L)^2]+(\omega M)^2(R+R_L)}. \tag{D.2}$$

where $|\Gamma|^2$ is the power reflection coefficient, which depends on the impedance mismatch at the source, and $Z_L = R_L + jX_L$. Clearly, if R increases, the efficiency η of the system decreases. For loops that use a feed line, R_{EFF} contributes to the total R.

To derive an expression for R_{EFF} as a function of frequency, let's write an expression

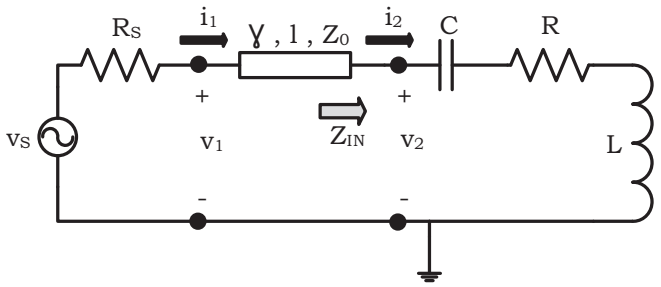

(a) Schematic of an RLC resonator with an input feed line. Here the transmission line is characterized by its complex propagation constant γ, physical length l, and characteristic impedance Z_0.

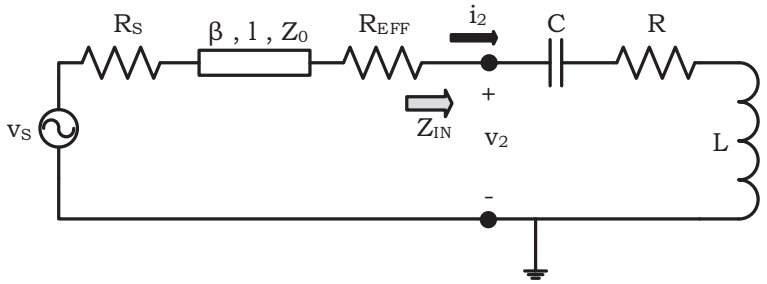

(b) Schematic of an RLC resonator with the power loss of the input feed line represented by an effective resistance R_{EFF}. A lossless transmission line is used to represent the phase delay.

Figure D.1 Effective feed line resistance R_{EFF} for an RLC resonator with an input feed line.

for the power lost in the feed line:

$$P_{feed} = \frac{1}{2}\left(\mathrm{Re}\{V_1 I_1^*\} - \mathrm{Re}\{V_2 I_2^*\}\right). \tag{D.3}$$

From the equation for the impedance looking into a transmission line:

$$\frac{V_1}{I_1} = Z_0 \frac{Z_{IN} + Z_0 \tanh(\gamma l)}{Z_0 + Z_{IN} \tanh(\gamma l)}, \tag{D.4a}$$

$$\frac{V_2}{I_2} = Z_{IN}. \tag{D.4b}$$

Here, $\gamma = \alpha + j\beta$ is the complex propagation constant of the transmission line, where α quantifies the attenuation along the line. Using (D.4a) and (D.4b):

$$\mathrm{Re}\{V_1 I_1^*\} = |I_1|^2 \,\mathrm{Re}\{\frac{V_1}{I_1}\} = |I_1|^2 \frac{g(Z_{IN})}{(Z_0' + pR_{IN} - qX_{IN})^2 + (Z_0'' + qR_{IN} + pX_{IN})^2}, \tag{D.5a}$$

$$\mathrm{Re}\{V_2 I_2^*\} = |I_2|^2 R_{IN}. \tag{D.5b}$$

Here, $g(Z_{IN})$ is defined as:

$$\begin{aligned} g(Z_{IN}) = {} & R_{IN}|Z_0|^2 + |\tanh(\gamma l)|^2 R_{IN}(Z_0'^2 - Z_0''^2) \\ & + Z_0' p(|Z_{IN}|^2 + |Z_0|^2) + 2Z_0' Z_0'' X_{IN} |\tanh(\gamma l)|^2 \\ & - Z_0'' q(|Z_0|^2 - R_{IN}^2 - X_{IN}^2). \end{aligned} \tag{D.6}$$

The impedance Z_{IN}, the characteristic impedance Z_0, and the function $\tanh(\gamma l)$ have been decomposed into their real and imaginary parts so that $Z_{IN} = R_{IN} + jX_{IN}$, $Z_0 = Z_0' + jZ_0''$, and $\tanh(\gamma l) = p + jq$.

The power P_{feed} dissipated in the feed line can be written as:

$$P_{feed} = \frac{|I_2|^2}{2}\left(\frac{|I_1|^2}{|I_2|^2}\,\mathrm{Re}\{\frac{V_1}{I_1}\} - R_{IN}\right). \tag{D.7}$$

Using (D.7), the effective resistance R_{EFF} can be written as:

$$R_{EFF} = \frac{2P_{feed}}{|I_2|^2} = \left[\frac{|I_1|^2}{|I_2|^2}\,\mathrm{Re}\{\frac{V_1}{I_1}\} - R_{IN}\right]. \tag{D.8}$$

The current I_1 can be written in terms of I_2 using the Z-matrix $\bar{\bar{Z}}_{TL}$ of the transmission line:

$$\begin{aligned} \implies \bar{\bar{Z}}_{TL} &= Z_0 \begin{bmatrix} \frac{1+e^{-2\gamma l}}{1-e^{-2\gamma l}} & \frac{2e^{-\gamma l}}{1-e^{-2\gamma l}} \\ \frac{2e^{-\gamma l}}{1-e^{-2\gamma l}} & \frac{1+e^{-2\gamma l}}{1-e^{-2\gamma l}} \end{bmatrix}, \\ \begin{bmatrix} V_1 \\ V_2 \end{bmatrix} &= \begin{bmatrix} V_1 \\ I_2 Z_{IN} \end{bmatrix} = \bar{\bar{Z}}_{TL} \begin{bmatrix} I_1 \\ -I_2 \end{bmatrix}, \\ \implies \frac{I_1}{I_2} &= \left[\frac{R_{IN} + jX_{IN}}{Z_0}\sinh(\gamma l) + \cosh(\gamma l)\right]. \end{aligned} \tag{D.9}$$

Substituting (D.5a), (D.6), and (D.9) into (D.8) provides an equation for R_{EFF} as a function of γ, Z_0, line length l, and Z_{IN}. Under the assumptions $Z_0'' << Z_0'$, $p << q$, and $R_{IN} \approx 0$, the equation simplifies to:

$$R_{EFF} = \frac{g(Z_{IN})|\cosh(\gamma l)|^2}{|Z_0|^2}. \tag{D.10}$$

By taking the derivative $\delta/\delta X_{IN}$ of (D.10), it can be shown that for a given frequency and transmission line, R_{EFF} achieves a minimum when $X_{IN} = X_{IN}^{min}$:

$$X_{IN}^{min} = -\frac{Z_0''|\tanh(\gamma l)|^2}{p + \frac{Z_0''}{|Z_0|}q}. \tag{D.11}$$

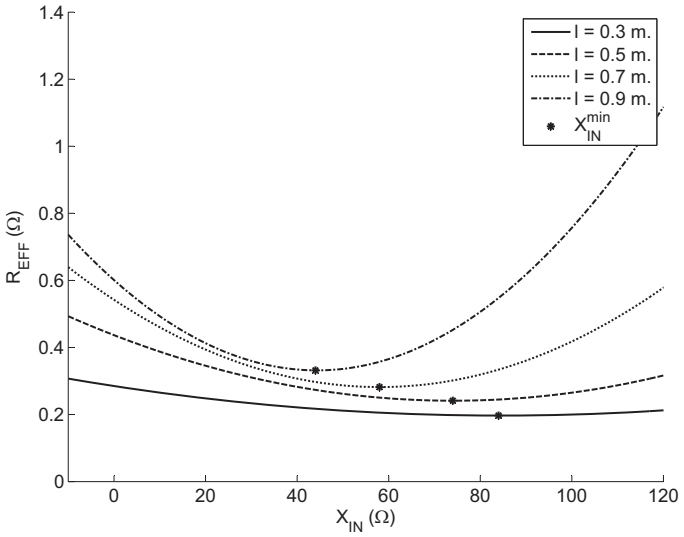

Figure D.2 The effective resistance R_{EFF} for the transmission line.

Figure (D.2) shows the variation of R_{EFF} with X_{IN} using (D.10) for a microstrip line of varying lengths attached to a lossless, reactive load jX_{IN}. The minima given by (D.11) are also plotted. The parameters of the microstrip, referring to Figure 7.1(b), are as follows:

- Height (a) = 813 μm
- Width (W) = 2 mm
- Relative Permittivity (ϵ_R) = 3.0
- Conductivity (σ) = 5.8e7 S/m
- Conductor Thickness (t) = 35 μm
- Loss Tangent ($\tan\delta$) = 0.001

The values of γ and Z_0 are extracted from the commercial circuit solver ADS at 40 MHz:

$$\gamma = 0.0105 + j1.31 \ m^{-1},$$
$$Z_0 = 50.38 - j0.3585 \ \Omega.$$

From Figure D.2, a longer feed line exhibits a higher R_{EFF} and a lower X_{IN}^{min}.

To verify (D.10), the analytical $|S_{11}|$ for the equivalent circuit of Figure D.1(b) is compared with the simulated $|S_{11}|$ for the actual circuit of Figure D.1(a).

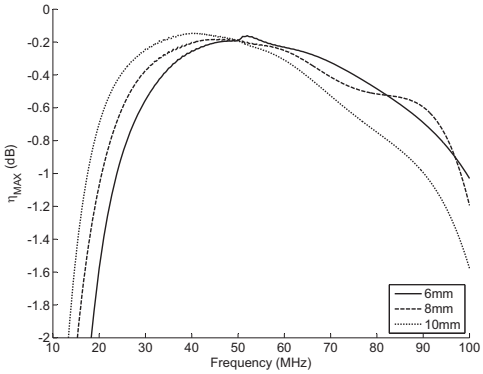

(a) Maximum power transfer for a system of coupled shielded-stripline loop resonators like those characterized in Table 6.1. Here, the coupling distance is 10 cm. The feed line causes the maximum power transfer efficiency to drop off over frequency.

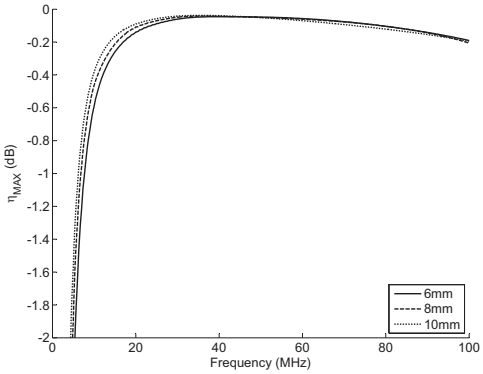

(b) Maximum power transfer for a system of coupled shielded-stripline loop resonators like those shown in Table 6.3. The coupling distance is assumed to be 10 cm. The maximum power transfer efficiency is greatly improved across the range of frequencies by decreasing the feed line length.

Figure D.3 Maximum power transfer efficiencies for different slit locations.

D.0.8 Implications for Coupled Loops

Referring to Figure 6.3, the input impedance Z_{IN} for a symmetric system of magnetically-coupled loops in a WNPT system can be written as [20]:

$$Z_{IN} = j(\omega L - \frac{1}{\omega C}) + R + \frac{(\omega M)^2}{j(\omega L - \frac{1}{\omega C}) + R + Z_L}. \tag{D.12}$$

For maximum power transfer [20]:

$$Z_S = Z_L = j\left(\frac{1}{\omega C} - \omega L\right) + \sqrt{R^2 + (\omega M)^2}. \tag{D.13}$$

Using the same analysis as for a single loop, R_{EFF} will be minimized at a point X_{IN}^{min}. As a result, the maximum achievable power transfer efficiency decreases as $|X_{IN} - X_{IN}^{min}|$ increases in the presence of an input feed line.

To verify these conclusions, pairs of coupled shielded-loop resonators from Tables 6.1 and 6.3 are simulated at a coupling distance of 10 cm. The maximum power transfer efficiency (achievable under a simultaneous conjugate match at both ports) is plotted versus frequency using the simulated S-parameters. Although thus far only the behavior of R_{EFF} with respect to X_{IN} has been discussed, the behavior versus frequency is similar. Figure D.3(a) shows the maximum power transfer efficiency for three different systems of coupled shielded-stripline loop resonators like those presented in Table 6.1. Three different trace widths W are used for the loops. It is clear that the efficiency is reduced for the higher frequencies. Figure D.3(b) shows the same results for the loops characterized in Table 6.3 (shifted ground slit).

The plots demonstrate that reducing the length of the feed line improves the performance of the loops away from the frequency corresponding to the minimum R_{EFF}.

Appendix E

Alternative Viewpoint of Low-Impedance Matching

An alternative perspective of the impedance transformation curves given in Figure 7.3 are presented in Figure E.1. Here, the Smith chart is normalized to Z_0. It can be shown that the impedance Z_S (see Figure 7.2(b)) presented by the feedline as a function of βl forms an off-center circle on the Smith chart. Moreover, for a given Z_A, this circle is fixed. Adjusting Z_A adjusts the size of the Z_S circle. By adjusting βl, the impedance Z_S can be rotated along the circle until it coincides with the constant resistance circle for Z_M, which is given by (7.4). Then, a series capacitor can be used to transform the impedance from Z_S to Z_M. By viewing the impedance transformation using Figure E.1, one can visually examine the constraints on Z_A by understanding its effect on the position of the Z_S circle.

To examine the behavior of the Z_S circle mathematically, the following definitions will be used:

$$\Gamma_A = \frac{Z_A - Z_0}{Z_A + Z_0}, \tag{E.1a}$$

$$\Gamma_X = \frac{Z_X - Z_0}{Z_X + Z_0}, \tag{E.1b}$$

$$\Gamma'_X = \frac{Z_X - Z_A}{Z_X + Z_A}, \tag{E.1c}$$

$$\Gamma_S = \frac{Z_S - Z_0}{Z_S + Z_0}. \tag{E.1d}$$

Consider the reflection coefficient Γ_S at the input of the transmission line in Figure E.2 (referenced to a characteristic impedance Z_0) written in terms of the reflection coefficient Γ'_X (referenced to a characteristic impedance Z_A):

$$\Gamma'_S = \Gamma'_X e^{-j2\beta l} = \left[\frac{Z_X - Z_A}{Z_X + Z_A}\right] e^{-j2\beta l}, \tag{E.2a}$$

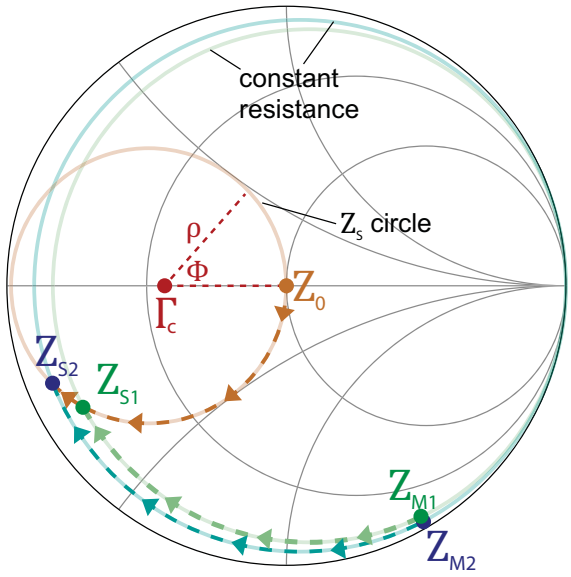

Figure E.1 Smith chart normalized to Z_0. The impedance transformation along the feedline of impedance Z_A follows a circle of radius ρ.

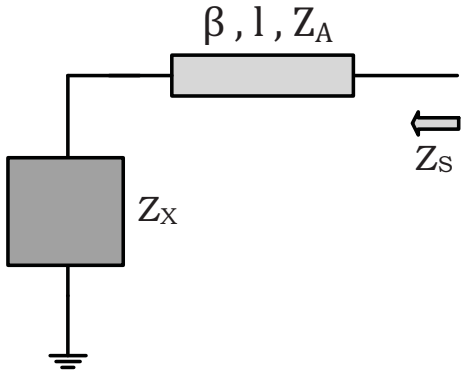

Figure E.2 Low-impedance transmission line connected to an arbitrary load impedance Z_X.

$$Z_S = Z_A \frac{1+\Gamma'_S}{1-\Gamma'_S} = Z_A \frac{1+\left[\frac{Z_X-Z_A}{Z_X+Z_A}\right] e^{-j2\beta l}}{1-\left[\frac{Z_X-Z_A}{Z_X+Z_A}\right] e^{-j2\beta l}}. \tag{E.2b}$$

Substituting (E.2a) into (E.2b), it can be shown that Γ_S reduces to:

$$\Gamma_S = \frac{\Gamma_A + \Gamma'_X e^{-j2\beta l}}{1+\Gamma_A \Gamma'_X e^{-j2\beta l}}. \tag{E.3}$$

Showing that the plot of Γ_S versus βl draws a circle on the Smith chart reduces to proving there exists Γ_C and ρ such that:

$$|\Gamma_S - \Gamma_C| = |y| = \rho. \tag{E.4}$$

Clearly, Γ_C and y should be a function of Z_0, Z_X, and Z_A, but Γ_C and ρ must be independent of βl. It can be shown that (E.4) is satisfied under the following conditions:

$$\Gamma_C = \frac{\Gamma_A(1-|\Gamma'_X|^2)}{1-\Gamma_A^2|\Gamma'_X|^2}, \tag{E.5a}$$

$$y = \frac{\Gamma'_X(1-\Gamma_A^2)}{1-\Gamma_A^2|\Gamma'_X|^2}e^{j2\theta}, \tag{E.5b}$$

$$\theta = \arg(\Gamma_A\Gamma'^*_X + e^{-j2\beta l}). \tag{E.5c}$$

Figure E.1 labels Γ_C, ρ, and $\phi = 2\theta$. for an arbitrary set of parameters Z_0, Z_A, and Z_X.

E.0.9 Special Case: $Z_X = Z_0$

In Chapter 7, $Z_X = Z_0$ (see Figure 7.2(b)). Under this condition, equations (E.3), (E.5a), (E.5b), and (E.5c) simplify as follows:

$$\Gamma_S = \frac{\Gamma'_X(e^{-j2\beta l}-1)}{1-|\Gamma'_X|^2e^{-j2\beta l}}, \tag{E.6a}$$

$$\Gamma_C = \left(\frac{-\Gamma'_X}{\Gamma'^2_X+1}\right), \tag{E.6b}$$

$$y = -\Gamma_C e^{j2\theta}, \tag{E.6c}$$

$$\theta = \arg(e^{-j2\beta l} - \Gamma'^2_L). \tag{E.6d}$$

From (E.6c), it is clear that $|\Gamma_C| = \rho$. If $Z_A < Z_0$ then $\Gamma_C = -\rho$ and the center of the Smith chart is coincident with the point $\Phi = 0$ on the Γ_S circle. Equations (E.6b) and (E.6c) show that ρ increases as Z_A decreases. In fact, as Z_A approaches 0, ρ approaches 1/2. Therefore, by varying Z_A, the Z_S impedance circle can be contracted and expanded. This interpretation of low-impedance matching can be used to visually explain Equation (7.14). Indeed, Z_A must be small enough that the Z_S impedance circle intersects with the constant resistance circle for Z_M.

Bibliography

[1] S. Tretyakov, *Analytical Modeling in Applied Electromagnetics*. Artech House, 2003.

[2] J. B. Pendry, "Negative refraction makes a perfect lens," *Physical Review Letters*, vol. 85, no. 18, p. 3966, 2000.

[3] A. Alù, M. G. Silveirinha, A. Salandrino, and N. Engheta, "Epsilon-near-zero metamaterials and electromagnetic sources: Tailoring the radiation phase pattern," *Physical Review B*, vol. 75, no. 15, p. 155410, 2007.

[4] J. B. Pendry, D. Schurig, and D. R. Smith, "Controlling electromagnetic fields," *Science*, vol. 312, no. 5781, pp. 1780–1782, 2006.

[5] U. Leonhardt, "Optical conformal mapping," *Science*, vol. 312, no. 5781, pp. 1777–1780, 2006.

[6] D. H. Werner and D.-H. Kwon, *Transformation Electromagnetics and Metamaterials*. Springer, 2014.

[7] S. Hrabar, I. Krois, I. Bonic, and A. Kiricenko, "Negative capacitor paves the way to ultra-broadband metamaterials," *Applied Physics Letters*, vol. 99, no. 25, p. 254103, 2011.

[8] N. Yu, P. Genevet, M. A. Kats, F. Aieta, J.-P. Tetienne, F. Capasso, and Z. Gaburro, "Light propagation with phase discontinuities: generalized laws of reflection and refraction," *Science*, vol. 334, no. 6054, pp. 333–337, 2011.

[9] C. Pfeiffer and A. Grbic, "Metamaterial Huygens surfaces: tailoring wave fronts with reflectionless sheets," *Physical Review Letters*, vol. 110, no. 19, p. 197401, 2013.

[10] M. Selvanayagam and G. V. Eleftheriades, "Discontinuous electromagnetic fields using orthogonal electric and magnetic currents for wavefront manipulation," *Optics Express*, vol. 21, no. 12, pp. 14 409–14 429, 2013.

[11] A. Kurs, A. Karalis, R. Moffatt, J. D. Joannopoulos, P. Fisher, and M. Soljačić, "Wireless power transfer via strongly coupled magnetic resonances," *Science*, vol. 317, no. 5834, pp. 83–86, 2007.

[12] L. Olvitz, D. Vinko, and T. Švedek, "Wireless power transfer for mobile phone charging device," in *MIPRO, 2012 Proceedings of the 35th International Convention*, May 2012, pp. 141–145.

[13] D. van Wageningen and T. Staring, "The Qi wireless power standard," in *2010 14th International Power Electronics and Motion Control Conference (EPE/PEMC)*, 2010, pp. 25–32.

[14] H. Jiang, S. Liang, J. Zhang, S. Liou, and H. Shahnasser, "Design and optimization of printed spiral coils in wireless power transfer for biomedical implants," in *2011 4th International Conference on Biomedical Engineering and Informatics (BMEI)*, vol. 2, Oct 2011, pp. 1064–1067.

[15] K. Jung, Y.-H. Kim, E. J. Choi, H. J. Kim, and Y.-J. Kim, "Wireless power transmission for implantable devices using inductive component of closed-magnetic circuit structure," in *2008 IEEE International Conference on Multisensor Fusion and Integration for Intelligent Systems*, August 2008, pp. 272–277.

[16] Y.-X. Guo, D. Zhu, and R. Jegadeesan, "Inductive wireless power transmission for implantable devices," in *2011 International Workshop on Antenna Technology (iWAT)*, March 2011, pp. 445–448.

[17] C. Koch, W. Mokwa, M. Goertz, and P. Walter, "First results of a study on a completely implanted retinal prosthesis in blind humans," in *2008 IEEE Sensors*, October 2008, pp. 1237–1240.

[18] T. Imura, H. Okabe, and Y. Hori, "Basic experimental study on helical antennas of wireless power transfer for electric vehicles by using magnetic resonant couplings," in *2009 IEEE Vehicle Power and Propulsion Conference*, September 2009, pp. 936–940.

[19] A. Sample, D. Meyer, and J. Smith, "Analysis, experimental results, and range adaptation of magnetically coupled resonators for wireless power transfer," *IEEE Transactions on Industrial Electronics*, vol. 58, no. 2, pp. 544–554, February 2011.

[20] E. Thomas, J. D. Heebl, C. Pfeiffer, and A. Grbic, "A power link study of wireless non-radiative power transfer systems using resonant shielded loops," *IEEE Transactions on Circuits and Systems I: Regular Papers*, vol. 59, no. 9, pp. 2125–2136, 2012.

[21] H. J. Orchard, R. S. Elliott, and G. J. Stern, "Optimising the synthesis of shaped beam antenna patterns," *IEE Proceedings H - Microwaves, Antennas and Propagation*, vol. 132, no. 1, pp. 63–68, February 1985.

[22] R. E. Collin and F. J. Zucker, *Antenna Theory*. McGraw-Hill New York, 1969.

[23] A. A. Oliner and D. R. Jackson, "Leaky-wave antennas," *Antenna Engineering Handbook*, vol. 4, 1993.

[24] J. L. Gómez-Tornero, A. D. L. T. Martínez, D. C. Rebenaque, M. Gugliemi, and A. Álvarez-Melcón, "Design of tapered leaky-wave antennas in hybrid waveguide-planar technology for millimeter waveband applications," *IEEE Transactions on Antennas and Propagation*, vol. 53, no. 8, pp. 2563–2577, 2005.

[25] R. Siragusa, E. Perret, P. Lemaitre-Auger, H. Van Nguyen, S. Tedjini, and C. Caloz, "A tapered CRLH interdigital/stub leaky-wave antenna with minimized side-lobe levels," *IEEE Antennas and Wireless Propagation Letters*, vol. 11, pp. 1214–1217, 2012.

[26] A. Martinez-Ros, J. Gómez-Tornero, and G. Goussetis, "Planar leaky-wave antenna with flexible control of the complex propagation constant," *IEEE Transactions on Antennas and Propagation*, vol. 60, no. 3, pp. 1625–1630, March 2012.

[27] C. H. Walter, *Traveling wave antennas*. Dover Publications,[1970, 1970.

[28] P. Burghignoli, F. Frezza, A. Galli, and G. Schettini, "Synthesis of broad-beam patterns through leaky-wave antennas with rectilinear geometry," *IEEE Antennas and Wireless Propagation Letters*, vol. 2, no. 1, pp. 136–139, 2003.

[29] A. Martinez-Ros, J. Gómez-Tornero, and G. Goussetis, "Holographic pattern synthesis with modulated substrate integrated waveguide line-source leaky-wave antennas," *IEEE Transactions on Antennas and Propagation*, vol. 61, no. 7, pp. 3466–3474, July 2013.

[30] J. L. Gomez-Tornero, A. J. Martínez-Ros, and R. Verdu-Monedero, "FFT synthesis of radiation patterns with wide nulls using tapered leaky-wave antennas," *IEEE Antennas and Wireless Propagation Letters*, vol. 9, pp. 518–521, 2010.

[31] W. P. Keizer, "Fast low-sidelobe synthesis for large planar array antennas utilizing successive fast Fourier transforms of the array factor," *IEEE Transactions on Antennas and Propagation*, vol. 55, no. 3, pp. 715–722, 2007.

[32] M. Ettorre and A. Grbic, "Generation of propagating Bessel beams using leaky-wave modes," *IEEE Transactions on Antennas and Propagation*, vol. 60, no. 8, pp. 3605–3613, 2012.

[33] G. V. Eleftheriades and K. G. Balmain, *Negative-Refraction Metamaterials: Fundamental Principles and Applications*. John Wiley & Sons, 2005.

[34] C. Caloz and T. Itoh, *Electromagnetic Metamaterials: Transmission Line Theory and Microwave Applications*. John Wiley & Sons, 2005.

[35] D. Sievenpiper, L. Zhang, R. F. Broas, N. G. Alexopolous, and E. Yablonovitch, "High-impedance electromagnetic surfaces with a forbidden frequency band," *IEEE Transactions on Microwave Theory and Techniques*, vol. 47, no. 11, pp. 2059–2074, 1999.

[36] C. A. Balanis, *Antenna Theory: Analysis and Design*. John Wiley & Sons, 2012.

[37] R. W. Hamming, *Digital Filters*. Courier Dover Publications, 1989.

[38] B. P. Lathi, *Linear Systems and Signals*. Oxford University Press, 2009.

[39] D. M. Pozar, *Microwave Engineering*. John Wiley & Sons, Inc., 2005.

[40] A. Yariv and P. Yeh, *Optical Waves in Crystals*. Wiley New York, 1984, vol. 5.

[41] R. C. Hansen, "Array pattern control and synthesis," *Proceedings of the IEEE*, vol. 80, no. 1, pp. 141–151, 1992.

[42] H. G. Booker and P. Clemmow, "The concept of an angular spectrum of plane waves, and its relation to that of polar diagram and aperture distribution," *Proceedings of the IEE-Part III: Radio and Communication Engineering*, vol. 97, no. 45, pp. 11–17, 1950.

[43] P. Woodward, "A method of calculating the field over a plane aperture required to produce a given polar diagram," *Journal of the Institution of Electrical Engineers-Part IIIA: Radiolocation*, vol. 93, no. 10, pp. 1554–1558, 1946.

[44] P. Woodward and J. Lawson, "The theoretical precision with which an arbitrary radiation-pattern may be obtained from a source of finite size," *Journal of the Institution of Electrical Engineers-Part III: Radio and Communication Engineering*, vol. 95, no. 37, pp. 363–370, 1948.

[45] R. Elliott, "On discretizing continuous aperture distributions," *IEEE Transactions on Antennas and Propagation*, vol. 25, no. 5, pp. 617–621, 1977.

[46] D. Kahaner, C. B. Moler, S. Nash, and G. E. Forsythe, *Numerical Methods and Software*. Prentice-Hall Englewood Cliffs, NJ, 1989.

[47] R. E. Hodges and Y. Rahmat-Samii, "On sampling continuous aperture distributions for discrete planar arrays," *IEEE Transactions on Antennas and Propagation*, vol. 44, no. 11, pp. 1499–1508, 1996.

[48] C. Pfeiffer and A. Grbic, "Bianisotropic metasurfaces for optimal polarization control: Analysis and synthesis," *Physical Review Applied*, vol. 2, no. 4, p. 044011, 2014.

[49] C. A. Balanis, *Advanced Engineering Electromagnetics*, 2012.

[50] J. D. Jackson, *Classical Electrodynamics*. Wiley New York etc., 1962, vol. 3.

[51] A. Patel and A. Grbic, "Effective surface impedance of a printed-circuit tensor impedance surface (PCTIS)," *IEEE Transactions on Microwave Theory and Techniques*, vol. 61, no. 4, pp. 1403–1413, 2013.

[52] D.-H. Kwon and D. H. Werner, "Transformation optical designs for wave collimators, flat lenses and right-angle bends," *New Journal of Physics*, vol. 10, no. 11, p. 115023, 2008.

[53] ——, "Polarization splitter and polarization rotator designs based on transformation optics," *Optics Express*, vol. 16, no. 23, pp. 18 731–18 738, Nov 2008.

[54] D. Schurig, J. Mock, B. Justice, S. A. Cummer, J. B. Pendry, A. Starr, and D. Smith, "Metamaterial electromagnetic cloak at microwave frequencies," *Science*, vol. 314, no. 5801, pp. 977–980, 2006.

[55] H. Chen, Z. Liang, P. Yao, X. Jiang, H. Ma, and C. T. Chan, "Extending the bandwidth of electromagnetic cloaks," *Physical Review B*, vol. 76, p. 241104, Dec 2007.

[56] C. Craeye and A. Bhattacharya, "Rule of thumb for cloaking bandwidth based on a wave-packet argument," *IEEE Transactions on Antennas and Propagation*, vol. 60, no. 7, pp. 3516–3520, July 2012.

[57] J. Li and J. B. Pendry, "Hiding under the carpet: A new strategy for cloaking," *Physical Review Letters*, vol. 101, p. 203901, Nov 2008.

[58] G. Gok and A. Grbic, "Alternative material parameters for transformation electromagnetics designs," *IEEE Transactions on Microwave Theory and Techniques*, vol. 61, no. 4, pp. 1414–1424, 2013.

[59] ——, "Tailoring the phase and power flow of electromagnetic fields," *Physical Review Letters*, vol. 111, no. 23, p. 233904, 2013.

[60] ——, "A printed antenna beam former implemented using tensor transmission-line metamaterials," in *2014 IEEE Antennas and Propagation Society International Symposium*, July 2014, pp. 765–766.

[61] S. Boyd and L. Vandenberghe, *Convex Optimization*. Cambridge university press, 2004.

[62] J. Jin, *The finite Element Method in Electromagnetics*. John Wiley & Sons, 2014.

[63] T. A. Davis, *Direct Methods for Sparse Linear Systems*. Siam, 2006, vol. 2.

[64] J. Nocedal and S. Wright, *Numerical optimization*. Springer Science & Business Media, 2006.

[65] W. Rotman and R. F. Turner, "Wide-angle microwave lens for line source applications," *IEEE Transactions on Antennas and Propagation*, vol. 11, no. 6, pp. 623–632, 1963.

[66] H.-H. Fuchs and D. Nussler, "Design of rotman lens for beamsteering of 94 ghz antenna array," *Electronics Letters*, vol. 35, no. 11, pp. 854–855, 1999.

[67] J. A. Kong, *Theory of Electromagnetic Waves*, 1975.

[68] J. Butler, "Beam-forming matrix simplifies design of electronically scanned antennas," *Electron. Des.*, vol. 9, no. 8, pp. 170–173, 1961.

[69] J. Blass, "Multidirectional antenna-a new approach to stacked beams," in *1958 IRE International Convention Record*, vol. 8. IEEE, 1960, pp. 48–50.

[70] R. K. Luneburg and M. Herzberger, *Mathematical Theory of Optics*. Univ. of California Press, 1964.

[71] G. Gok and A. Grbic, "Homogenization of tensor TL metamaterials," *Metamaterials*, vol. 5, no. 2, pp. 81–89, 2011.

[72] W. Gander, G. H. Golub, and R. Strebel, "Least-squares fitting of circles and ellipses," *BIT Numerical Mathematics*, vol. 34, no. 4, pp. 558–578, 1994.

[73] F. J. Harris, "On the use of windows for harmonic analysis with the discrete Fourier transform," *Proceedings of the IEEE*, vol. 66, no. 1, pp. 51–83, 1978.

[74] W. C. Brown, "The history of power transmission by radio waves," *IEEE Transactions on Microwave Theory and Techniques*, vol. 32, no. 9, pp. 1230–1242, 1984.

[75] N. Tesla, "Apparatus for transmission of electrical energy," US Patent no. 645,576, 1900.

[76] ——, "System of Transmission of Electrical Energy, US Patent 645576," 1897.

[77] M. Hutin, "hutin," Oct. 23 1894, uS Patent 527,857. [Online]. Available: http://www.google.com/patents/US527857

[78] M. Dionigi and M. Mongiardo, "A novel coaxial loop resonator for wireless power transfer," *International Journal of RF and Microwave Computer-Aided Engineering*, vol. 22, no. 3, pp. 345–352, 2012.

[79] J. Sojdehei, P. Wrathall, and D. Dinn, "Magneto-inductive (MI) communications," in *OCEANS 2001 MTS/IEEE Conference and Exhibition*, vol. 1, 2001, pp. 513–519.

[80] S. Kim, T. Knoll, and O. Scholz, "Feasibility of inductive communication between millimetersized robots," in *The First IEEE/RAS-EMBS International Conference on Biomedical Robotics and Biomechatronics, 2006*, February 2006, pp. 1178–1182.

[81] J. Dyson, "Measurement of near fields of antennas and scatterers," *IEEE Transactions on Antennas and Propagation*, vol. 21, no. 4, pp. 446–460, July 1973.

[82] L. Libby, "Special aspects of balanced shielded loops," *Proceedings of the IRE*, vol. 34, no. 9, pp. 641–646, September 1946.

[83] F. Segura-Quijano, J. Garcia-Canton, J. Sacristan, T. Oses, and A. Baldi, "Wireless powering of single-chip systems with integrated coil and external wire-loop resonator," *Applied Physics Letters*, vol. 92, no. 7, Feb 2008.

[84] S. Han and D. Wentzloff, "Wireless power transfer using resonant inductive coupling for 3D integrated ICs," in *2010 IEEE International 3D Systems Integration Conference*, November 2010, pp. 1–5.

[85] K. Onizuka, H. Kawaguchi, M. Takamiya, T. Kuroda, and T. Sakurai, "Chip-to-chip inductive wireless power transmission system for SiP applications," in *2006 IEEE Custom Integrated Circuits Conference*, September 2006, pp. 575–578.

[86] H. Kim and H.-M. Lee, "Design of an integrated wireless power transfer system with high power transfer efficiency and compact structure," in *2012 6th European Conference on Antennas and Propagation*, March 2012, pp. 3627–3630.

[87] S. Bhuyan, S. Panda, K. Sivanand, and R. Kumar, "A compact resonace-based wireless energy transfer system for implanted electronic devices," in *2011 International Conference on Energy, Automation, and Signal*, December 2011, pp. 1–3.

[88] J. W. Kim, H.-C. Son, D.-H. Kim, J.-R. Yang, K.-H. Kim, K.-M. Lee, and Y.-J. Park, "Wireless power transfer for free positioning using compact planar multiple self-resonators," in *2012 IEEE MTT-S International Microwave Workshop Series on Innovative Wireless Power Transmission: Technologies, Systems, and Applications*, May 2012, pp. 127–130.

[89] H. Wheeler, "Transmission-line properties of a strip line between parallel planes," *IEEE Transactions on Microwave Theory and Techniques*, vol. 26, no. 11, pp. 866–876, November 1978.

[90] E. Hammerstad and O. Jensen, "Accurate models for microstrip computer-aided design," in *1980 IEEE MTT-S International Microwave Symposium Digest*, May 1980, pp. 407–409.

[91] D. L. Sengupta and V. V. Liepa, *Applied Electromagnetics and Electromagnetic Compatibility*. Wiley-Interscience, 2005.

[92] S. Tretyakov, *Analytical Modeling in Applied Electromagnetics*. Artech House Publishers, 2003.

[93] F. E. Terman, *Radio Engineers' Handbook*. McGraw-Hill New York, 1943, vol. 19.

[94] S. Orfanidis, *Electromagnetic Waves and Antenna*. Rutgers Univ. Press, 2004.

[95] J. D. Heebl, E. M. Thomas, R. P. Penno, and A. Grbic, "Comprehensive analysis and measurement of frequency-tuned and impedance-tuned wireless non-radiative power-transfer systems," *IEEE Antennas and Propagation Magazine*, vol. 56, no. 5, pp. 131–148, Oct 2014.

[96] A. Christ, M. Douglas, J. Nadakuduti, and N. Kuster, "Assessing human exposure to electromagnetic fields from wireless power transmission systems," *Proceedings of the IEEE*, vol. 101, no. 6, pp. 1482–1493, 2013.

[97] T. Linlin, H. Xueliang, L. Hui, and H. Hui, "Study of wireless power transfer system through strongly coupled resonances," in *2010 International Conference on Electrical and Control Engineering (ICECE)*, June 2010, pp. 4275–4278.

[98] T. Mizuno, S. Yachi, A. Kamiya, and D. Yamamoto, "Improvement in efficiency of wireless power transfer of magnetic resonant coupling using magnetoplated wire," *IEEE Transactions on Magnetics*, vol. 47, no. 10, pp. 4445–4448, 2011.

[99] S.-H. Lee and R. D. Lorenz, "Development and validation of model for 95%-efficiency 220-W wireless power transfer over a 30-cm air gap," *IEEE Transactions on Industry Applications*, vol. 47, no. 6, pp. 2495–2504, 2011.

[100] G. Turin, "An introduction to matched filters," *IRE Transactions on Information Theory*, vol. 3, no. 6, pp. 311–329, 1960.

[101] K. Hoffman and R. Kunze, "Linear algebra. 1971," *Englewood Cliffs, New Jersey*.